
On the Retrieval of Circumsolar Radiation from Satellite Observations and Weather Model Output

Dipl.-Met. Bernhard Ulrich Reinhardt



München 2013

On the Retrieval of Circumsolar Radiation from Satellite Observations and Weather Model Output

Dipl.-Met. Bernhard Ulrich Reinhardt

Dissertation

der Fakultät für Physik
der Ludwig-Maximilians-Universität
München

vorgelegt von

Dipl.-Met. Bernhard Ulrich Reinhardt

Institut für Physik der Atmosphäre
Deutsches Zentrum für Luft- und Raumfahrt
Oberpfaffenhofen

München, August 2013

Erstgutachter: Prof. Dr. Bernhard Mayer

Zweitgutachter: Prof. Dr. Markus Rapp

Tag der mündlichen Prüfung: 20.11.2013

Contents

| | |
|--|------------|
| Zusammenfassung | vii |
| Abstract | ix |
| 1 Introduction | 1 |
| 1.1 Circumsolar Radiation and Concentrating Solar Technologies | 1 |
| 1.2 Aims of this Study | 3 |
| 2 Basic Principles | 7 |
| 2.1 The Radiative Transfer Equation | 7 |
| 2.2 Scattering of Sunlight | 10 |
| 2.3 Remote Sensing of Clouds from MSG | 12 |
| 2.3.1 The SEVIRI Instrument | 12 |
| 2.3.2 Retrieval of Cloud Properties from Reflected Solar Radiation | 15 |
| 2.4 Passive Satellite Remote Sensing of Aerosol | 17 |
| 2.5 The Sunshape | 19 |
| 2.6 The Circumsolar Ratio – CSR | 21 |
| 2.7 Ground Based Measurements of the Circumsolar Radiation | 23 |
| 3 Tools and Methods | 25 |
| 3.1 Optical and Microphysical Properties of Cirrus Clouds | 25 |
| 3.2 Cloud Property Remote Sensing with the APICS Algorithm | 27 |
| 3.2.1 Algorithm Description | 27 |
| 3.2.2 Auxiliary Albedo Dataset | 28 |
| 3.2.3 Cirrus Cloud Mask | 31 |
| 3.3 Aerosol Input and Processing | 33 |
| 3.3.1 Modeled Aerosol Data from the ECMWF IFS | 33 |
| 3.3.2 Aerosol Optical Properties | 34 |
| 3.3.3 Post-Processing of ECMWF Output | 39 |
| 3.4 Atmospheric Radiative Transfer | 40 |
| 3.4.1 The RTE-Solvers DISORT and MYSTIC | 40 |
| 3.4.2 Adaptation of the RTE-Solver MYSTIC | 42 |
| 3.4.3 Pseudo-Spectral and Solar Integrated Radiative Transfer | 50 |

| | | |
|----------|---|------------|
| 3.5 | Parametrization of Circumsolar Radiation | 52 |
| 3.5.1 | Concept of the Apparent Optical Thickness | 53 |
| 3.5.2 | Treatment of Multiple Scattering Layers – The Adding Method | 58 |
| 3.5.3 | Sensitivity of the CSR Parameterization on Sun Zenith Angle | 64 |
| 3.5.4 | Sensitivity of the CSR Parameterization on the Scattering Layer’s Geometry | 65 |
| 3.5.5 | Further Aspects of the Apparent Optical Thickness Approach | 66 |
| 3.6 | Sensitivity of Circumsolar Radiation to Ice Particle Shape | 67 |
| 3.7 | Sensitivity of CSR to Aerosol Particle Shape and Relative Humidity | 68 |
| 4 | Results | 73 |
| 4.1 | Intercomparison of Retrieval Results for Different Ice Particle Shapes | 73 |
| 4.2 | Validation | 76 |
| 4.2.1 | Validation of Aerosol Related Circumsolar Radiation | 79 |
| 4.2.2 | Validation of Cirrus Related Circumsolar Radiation | 82 |
| 4.3 | Characteristics of Cirrus-Related Circumsolar Radiation | 89 |
| 4.3.1 | Spatial Distribution | 89 |
| 4.3.2 | Irradiance Overestimation by Pyrheliometers | 91 |
| 4.3.3 | Relation of Irradiance and CSR | 94 |
| 5 | Discussion | 97 |
| 5.1 | Statistical Post-Processing of IFS Aerosol Output | 97 |
| 5.2 | Uncertainties in the Cirrus Cloud Property Retrieval | 100 |
| 5.2.1 | Undetected Cirrus Clouds | 101 |
| 5.2.2 | Spurious SEVIRI Pixels | 107 |
| 5.3 | Comparison of the Satellite CSR Retrieval to a Regression Model | 107 |
| 6 | Conclusions | 111 |
| 6.1 | Synopsis of Findings | 112 |
| 6.2 | Outlook | 113 |
| | Bibliography | 115 |
| | Glossary | 125 |
| | Acknowledgements | 127 |

Zusammenfassung

Konzentrierende Solarkraft steht im Wettstreit mit anderen sich dynamisch entwickelnden erneuerbaren Energiequellen. Ein zentraler Erfolgsfaktor ist dabei die Verringerung der Energieerzeugungskosten. Bei der Verfolgung dieses Ziels kommt der verbesserten Bestimmung der Einstrahlung eine wichtige Rolle zu. Finanzierungskosten für Neuanlagen können durch eine genauere Vorhersage der solaren Resource verringert werden, weil diese zu einer Reduzierung der finanziellen Risiken führt. Desweiteren erlaubt eine verbesserte Bestimmung der Einstrahlung zukünftige Anlagen in Bezug auf die lokalen Bedingungen zu optimieren. Dies senkt die Kosten und erhöht die Energieeffizienz. Die Zirkumsolarstrahlung ist ein Parameter, dem bei der Ressourcenbestimmung immer mehr Aufmerksamkeit zu Teil wird. Sie wird durch Vorwärtsstreuung des Sonnenlichts an Wolken- und Aerosolpartikeln hervorgerufen. Die Messung von Zirkumsolarstrahlung ist jedoch anspruchsvoll und es existieren nur wenige Messreihen von eingeschränktem Umfang. Um die Lücke zwischen der vermehrten Nachfrage nach Daten zur Zirkumsolarstrahlung und deren eingeschränkter Verfügbarkeit zu füllen, wurde in dieser Arbeit eine Methode zur Bestimmung der Zirkumsolarstrahlung aus verfügbaren Datensätzen von Aerosol- und Wolkeneigenschaften entwickelt. Im Speziellen wurden die optische Dicke und der Effektivradius von Cirrus-Wolken, sowie die Flächenmassenkonzentration verschiedener Aerosolkomponenten ausgewertet. Den Kern der Methode zur Ableitung der Zirkumsolarstrahlung stellt eine schnelle und dennoch genaue Parametrisierung dar. Diese erlaubt es die Zirkumsolarstrahlung mittels einfacher analytischer Ausdrücke aus zuvor tabellierten Koeffizienten zu berechnen, anstatt den Strahlungstransport zeitaufwändig numerisch zu berechnen. Die entsprechenden Tabellen wurden mittels umfangreicher Simulationen mit einer speziell angepassten Version des Monte Carlo Strahlungstransportmodells MYSTIC erstellt. MYSTIC wurde im Rahmen der Studie unter anderem um eine realistische Strahlungsquelle erweitert, indem die bisher verwendete Punktquelle durch eine ausgedehnte Sonnenscheibe mit wellenlängenabhängiger Helligkeitsverteilung ersetzt wurde.

Die ausgewerteten Aerosolflächenmassenkonzentrationen wurden als Modellausgabe des Integrated Forecast System (IFS) vom European Centre for Medium-Range Weather Forecasts (ECMWF) bezogen. Um die Wolkeneigenschaften von Cirren abzuleiten wurde das APICS Retrievalsystem auf Messungen der Meteosat Second Generation (MSG) Satelliten angewandt. Im Zuge der Studie wurde APICS für das Retrieval optisch dünner Cirren optimiert. Dazu wurde ein neuer Datensatz der Bodenalbedo auf Basis von MSG Messungen generiert, der als a priori Annahme in das Retrieval einfließt. Dieser neue Datensatz

ist, im Gegensatz zu dem bisher verwendeten, konsistent zu den anderen innerhalb des Retrievals getroffenen Annahmen. Dies ist eine wichtige Voraussetzung für die Ableitung der Eigenschaften von optisch dünnen Cirren. Desweiteren wurde APICS mit einer neuen Wolkenmaske betrieben, die auf der Ausgabe des COCS-Cirrenretrievals basiert. Sie ersetzt die zuvor genutzte Wolkenmaske des MeCiDa Eiswolkendetektionsalgorithmus. Dadurch können etwa 70 bis 80 Prozent mehr von jenen dünnen Cirren berücksichtigt werden, die noch genug Sonnenlicht zum Betrieb einer typischen solar-thermischen Anlage passieren lassen.

In Bezug auf Cirren stellt die Form der Eispartikel einen Unsicherheitsfaktor dar – sowohl bei der Ableitung der Wolkeneigenschaften, als auch bei der Berechnung der Zirkumsolarstrahlung. Bisher gibt es noch keine Möglichkeit die Partikelform von MSG aus zu bestimmen, sondern es muss eine Annahme a priori gemacht werden. Um eine Bestimmung der daraus folgenden Unsicherheit zu ermöglichen wurde APICS erweitert, so dass mehrere neue Eispartikelformen bei der Ableitung der Wolkeneigenschaften verwendet werden können. Damit konnte eine Unsicherheit in der Größenordnung von bis zu 50% in der mittleren Zirkumsolarstrahlung festgestellt werden, die aus der Unbestimmtheit der Eispartikelform folgt.

Die entwickelte Methode zur Ableitung der Zirkumsolarstrahlung wurde mit Bodmessungen des Zirkumsolarverhältnis (engl. circumsolar ratio, CSR) validiert, die an der Plataforma Solar de Almería (PSA) durchgeführt wurden. Dabei zeigte sich, dass die statistische Verteilung der Zirkumsolarstrahlung mit beiden der verwendeten “Baum” Eispartikelformmischungen gut charakterisiert werden kann. Beim Vergleich instantaner Werte treten jedoch Timing- und Amplitudenfehlern auf. In der Validierung zeigte sich für das CSR eine mittlere absolute Abweichung (engl. mean absolute deviation, MAD) von 0.11 für beide “Baum” Parametrisierungen, ein Bias von 4% bzw. -11% und eine Spearman Rang-Korrelation $r_{\text{rank,CSR}}$ von 0.54 bzw. 0.48. Wenn Messungen mit sub-skaligen Cumulus Wolken innerhalb der entsprechenden Satellitenpixel manuell ausgefiltert wurden, verbesserte sich die Übereinstimmung instantaner Werte. Dies spiegelt sich wider in MAD-Werten von 0.08 bzw. 0.07 und $r_{\text{rank,CSR}}$ -Werten von 0.79 bzw. 0.76. Des Weiteren stellte sich heraus, dass das von Aerosol verursachte CSR deutlich unterschätzt wird, wenn die Daten vom IFS unmodifiziert verwendet werden. Erst nach einer Anpassung der Aerosolflächenmassenkonzentration können sinnvolle Ergebnisse erzielt werden. Vermutlich ist eine zu geringe Konzentration von großen Mineralstaubpartikeln im IFS der Grund für die Unterschätzung der CSR.

Die entwickelte Methode kann in Zukunft ausgeweitet und mit anderen Datenquellen kombiniert werden. Während bodengebundene Referenzmessungen bisher die Beurteilung der Zirkumsolarstrahlung an nur wenigen Messstationen zulassen, können mit der hier neu entwickelten Methode beliebige Kraftwerksstandorte begutachtet werden.

Abstract

Concentrating solar technologies compete with other rapidly developing renewable energy sources. To succeed it is vital to lower the levelized cost of energy. There are several parameters that can be optimized to reach this goal, but a key component is the improvement of the resource assessment. A better prediction of the solar resource for new facilities brings down financing costs as financial risks are reduced. Moreover, improved solar resource assessment allows to optimize new facilities in regard to the local insolation conditions. This increases energy and cost efficiency. One parameter that is becoming more and more important for the resource assessment is the circumsolar radiation. It is caused by forward scattering of sun light by cloud or aerosol particles. However, measuring circumsolar radiation is demanding and only very limited data sets are available. As a step to bridge this gap, a method was developed in this study to determine circumsolar radiation from readily available data on clouds and aerosol. Specifically, the effective radius and optical thickness of cirrus clouds were used, as well as area mass loadings of several aerosol components. The core of the method to determine the circumsolar radiation is a fast yet precise parameterization. It allows to compute the circumsolar radiation by simple analytical expressions from previously tabulated coefficients, instead of solving the radiative transfer by time-consuming numerical simulations. The lookup tables were generated by extensive calculations using a specifically adjusted version of the Monte Carlo radiative transfer model MYSTIC. To this end, MYSTIC was enhanced with a realistic radiation source: The point source used so far was replaced by a extended sun disk which features a wavelength dependent brightness distribution.

The evaluated aerosol area mass loadings were obtained from the European Centre for Medium-Range Weather Forecasts (ECMWF) as model output of the Integrated Forecast System (IFS). To derive the cirrus cloud properties the APICS retrieval framework was applied to Meteosat Second Generation (MSG) measurements. During the course of this study APICS was optimized regarding the retrieval of optically thin cirrus clouds. To this end, a new ground albedo data set was generated on the basis of MSG measurements which serves as a priori assumption in the retrieval. This new data set is, in contrast the so far used one, consistent to the other assumptions made within the retrieval. This is an important pre-requisite for the successful retrieval of optically thin cirrus clouds. Furthermore, APICS was operated with a new cloud mask based on output of the COCS cirrus cloud property retrieval algorithm. It replaces the formerly used cloud mask from the MeCiDa cirrus detection algorithm. Thereby in the order of 70 to 80 percent more optically thin cirrus clouds can be considered, which allow enough light to pass for operation of a

typical solar thermal utility.

Considering cirrus clouds the prevailing ice particle shape is an uncertainty factor in the cloud property retrieval as well as in the computation of circumsolar radiation. So far it cannot be determined from MSG but must be assumed a priori. To allow for an uncertainty analysis concerning this parameter APICS was extended to consider several new ice particle shapes in the retrieval process. It was found, the nescience of the ice particle shape leads to an uncertainty of up to 50% in the mean circumsolar irradiance.

The newly developed method for the retrieval of circumsolar radiation was validated with ground measurements of the circumsolar ratio (CSR) performed at the Plataforma Solar de Almería (PSA). This showed that the statistical distribution of the circumsolar radiation can be well characterized with both of the two employed “Baum” ice particle shape parameterizations. When comparing instantaneous values timing and amplitude errors become evident, tough. For the circumsolar ratio (CSR) the validation yielded a mean absolute deviation (MAD) of 0.11 for both “Baum” parameterizations, a bias of 4% and -11%, respectively, and a Spearman rank correlation $r_{\text{rank,CSR}}$ of 0.54 and 0.48, respectively. If measurements with sub-scale cumulus clouds within the relevant satellite pixels were manually removed, the agreement of instantaneous values improved. This reflects in the MAD values of 0.08 and 0.07, respectively, and $r_{\text{rank,CSR}}$ values to 0.79 and 0.76, respectively. Furthermore, it was found that for aerosol the CSR is strongly underestimated if the IFS output is used head on. Only after adjusting the aerosol mass loadings reasonable values can be obtained. An underrepresentation of large dust particles in the IFS seems most likely to be reason for this.

In the future the method developed in this study can be extended and combined with other data sources. While ground-based reference measurements so far only allowed the assessment of the circumsolar radiation at few specific measurement sites, the newly developed method makes it possible to survey arbitrary sites.

Chapter 1

Introduction

This thesis deals with the retrieval of circumsolar radiation to the benefit of concentrating solar technology (CST). The term *circumsolar* indicates that the radiation is observable in an annular region of the sky of a few degrees extent surrounding the sun. The phenomenon of enhanced brightness in the circumsolar region is also referred to as *aureole* (comp. Fig. 1.1).

1.1 Circumsolar Radiation and Concentrating Solar Technologies

Concentrating solar technology denotes systems that concentrate the sun's radiation to harvest its energy. Concentration of the sun light is required if the natural non-concentrated solar radiative flux density is not sufficient for the considered purpose – the most obvious application is producing high temperatures. Concentration of radiation is inseparable from a limiting of the angular region from which radiation can be utilized. This comes from the fact that the étendue of a infinitesimal pencil of light $dU = n dA d\Omega$ is conserved in geometric optics (Chaves, 2008). n is the refractive index of the medium, dA the infinitesimal area perpendicular to propagation direction through which the light passes and $d\Omega$ the solid angle covered by the pencil. CSTs typically have acceptance half-angles α between 0.7° and 2.3° (Blanc, 2013, in regard to solar thermal systems). These systems therefore require a tracking mechanism to follow the position of the sun. The tracking comes with the advantage of the sun rays falling approximately perpendicular onto the

system. No reduction of the incident irradiance through the so called “cosine effect” occurs, as it is the case with non-tracking solar technologies, like common photovoltaics (e.g. King, 1996). However, concentrating systems cannot utilize most of the diffuse radiation from the upper half space. The primary measure used to quantify the energy input into a concentrating system is the direct normal irradiance (DNI), while for non-concentrating systems the global horizontal irradiance (GHI) is of importance. The CSTs aperture sizes may seem narrow but they still are considerably larger than the sun disk, which exhibits an average angular radius α_{sun} of 0.266° ¹. Therefore it is somewhat ambiguous to use the *direct* normal irradiance as quantity for the energy input. While in radiative transfer modelling direct radiation is considered as radiation which has not been scattered, in experimental meteorology it is defined as the radiation measured by a pyrheliometer, with α usually 2.5° (World Meteorological Organization standard according to CIMO Guide, chap. 7). Certainly both definitions will not match the energy ingress through varying CST apertures exactly. Indeed the deviations may be quite large. Furthermore not all radiation accepted by a CST system is converted equally well. The conversion efficiency usually depends on the angle of incidence. Both issues are connected to circumsolar radiation: Considering pyrheliometer measurements, circumsolar radiation can cause an overestimation of the solar irradiance available as resource for CST. Moreover, for the design and the precise evaluation of high flux solar concentrators the radiance distribution inside and around the sun disk, called sunshape, needs to be known (e.g. Rabl and Bendt (1982), Schubnell (1992), Neumann and Witzke (1999) or Buie and Monger (2004)). To take these effects into account, CST operators, constructors and designers need methods to determine the circumsolar radiation entering different sized CST apertures.

Circumsolar radiation is caused by forward scattering of sun light by cloud or aerosol particles. If these particles are horizontally evenly distributed, the radiance decreases with angular distance from the sun. The steepness and shape of this angular gradient depends on the particles’ type, shape and size as well as on the optical thickness of the scattering layer. Thus, perception of circumsolar radiation by any optics pointed at the sun – be it a pyrheliometer or a CST system – is strongly dependent not only on its opening half-angle α but also on the sky conditions. Furthermore, the discrepancy in perception caused by different opening angles is not constant, but also varies with sky conditions.

¹Depending on the earth-sun distance, α_{sun} varies between 0.261° and 0.271° (e.g. calculated from sun radius and earth-sun distance values given in Liou, 1980).



Figure 1.1: Picture of the sky, shot in the direction of the sun (courtesy of Bernhard Mayer). Clouds are obstructing the sun causing a distinct aureole.

1.2 Aims of this Study

Previous studies have dealt with the simulation of circumsolar radiation for a range of atmospheric conditions (e.g. Grassl, 1971; Thomalla et al., 1983). There also have been efforts to measure circumsolar radiation from the ground (e.g. Grether et al., 1980; Noring et al., 1991; Ritter and Voss, 2000; Neumann et al., 2002; DeVore et al., 2009; Wilbert et al., 2011, 2013). Following the ground measurements there have been attempts to parameterize circumsolar radiation based on regression of meteorological variables (e.g. Watt, 1980; Neumann et al., 1998). However these parameterizations do not consider properly the physical reason of the variability of circumsolar radiation – the properties of the scattering particles. The cause for circumsolar radiation, clouds and aerosols, are temporally and spatially variable. To assess the effect of circumsolar radiation on CST systems at new locations, data sets with good resolution and coverage in time *and* space are needed to fully assess the impact on CSR system design and operations.

There have been studies which focus on the retrieval of cloud and aerosol properties from circumsolar radiation measurements (e.g. Nakajima et al., 1983; Min and Duan, 2005; DeVore et al., 2009) and recently also from stellar aureole measurements (DeVore et al., 2013). The presented study followed the opposite approach: The aim of this study was to develop

a method which allows to derive the circumsolar radiation from globally available data on clouds and aerosols. The methodology was developed, validated and applied on the basis of two specific data sources: Cloud properties retrieved from measurements of the geostationary Meteosat Second Generation (MSG) satellites (Sect. 2.3) and modelled aerosol concentrations from the Integrated Forecast System (IFS) of the ECMWF² (Sect. 3.3.1). However, the methodology can be adapted to other data sources as well. The utilized data sources have big advantages considering global coverage, site intra-comparability and financial costs compared to ground measurements. The data are readily available for many regions of the world covering longer time spans than most available ground measurement time series of circumsolar radiation.

Considering clouds, this study only deals with circumsolar radiation caused by cirrus clouds. These ice clouds often occur with an optical thickness τ ranging from 0.1 to 2.0, that on one hand still allows the operation of CSTs, and on the other hand makes them detectable by satellites. Other cloud types are usually optically thicker, such that the transmitted direct radiation is insufficient for the operation of CSTs.

The core of the method is a fast yet precise parameterization which converts cloud or aerosol parameters into circumsolar radiation measures. The parameterization is assisted by a lookup table which is based on simulations of the circumsolar radiation. To allow for these simulations, the radiative transfer solver “Monte Carlo Code for the Physically Correct Tracing of Photons in Cloudy Atmospheres”, MYSTIC (Mayer, 2009) was extended by the capability to calculate circumsolar radiation.

Concentrating solar technologies can be divided into two categories – solar thermal units and concentrating photovoltaics. The principle of the former is to generate heat, which can be utilized for power generation, as industrial process heat or to drive chemical processes. The latter uses photovoltaic cells to generate power. In solar thermal applications basically the whole spectrum of the sun light can be exploited (up to $\approx 2.5 \mu\text{m}$, e.g. Wesselak and Schabbach, 2009), while photovoltaics have a narrower spectral response. This work primarily focuses on solar thermal applications, i.e. the broad band solar integrated circumsolar radiation, but the developed methods can in principle be applied to concentrating photovoltaics with little modification.

The manuscript is structured as follows. In Chapter 2 an overview of the basic principles is given, on which this work is founded. In Chapter 3 the tools and methods used in this study

²European Centre for Medium-Range Weather Forecasts

are described. This includes a description of the achieved improvements with respect to the exact simulation of the sunshape with the radiative transfer solver MYSTIC, as well as concerning the retrieval of cirrus cloud properties from MSG measurements with the APICS algorithm. Finally the core of the method, the parameterization of circumsolar radiation is developed in this chapter. Results obtained by applying the developed method on selected data are shown in Chapter 4. Furthermore a validation utilizing ground measurements performed at the Plataforma Solar de Almería, Spain, is presented. Error sources and the respective sensitivity of the results are discussed in Chapter 5. Furthermore a comparison of the developed method to a parameterization based on DNI and GHI measurements is presented. A synopsis of the thesis as well as an outlook is given in Chapter 6.

Parts of this thesis concerning cirrus related circumsolar radiation have already been published in Reinhardt et al. (2012, 2013).

Chapter 2

Basic Principles

In this chapter the basic principles and mechanisms underlying this thesis are outlined. Virtually all aspects of this work are connected to the transfer of sunlight through the atmosphere. In Sect. 2.1 it is sketched how this process can be mathematically expressed in the radiative transfer equation (RTE). Closely connected is Sect. 2.2 which deals with the scattering of sunlight in the atmosphere. The satellite based remote sensing of properties of cloud and aerosol particles – which are the reason for circumsolar radiation – is sketched in Secs. 2.3 & 2.4. Sections 2.5, 2.6 & 2.7 outline how circumsolar radiation can be quantified and how it is measured from the ground.

2.1 The Radiative Transfer Equation

The pivotal physical mechanism dealt with in this work under many different aspects is the transfer of sunlight through the atmosphere. Let us therefore briefly recapitulate the equations governing the radiative transfer. The following considerations are adapted from Zdunkowski et al. (2007).

Two important radiation quantities which appear repeatedly throughout this work are the irradiance I , also called flux, and the radiance L . The irradiance quantifies the radiant power incident on a surface per unit area. Consequently it is given in units of (W/m^2). The radiance holds the information on how much radiant power is coming from which

directions. It is given in units of (W/m²/sr). Integration of the radiance over a solid angle Ω will yield irradiance:

$$I = \int_{\Omega} L \cos \theta d\Omega \quad , \quad (2.1)$$

where θ is the angle between the considered surface normal in regard to which I is calculated and the solid angle element $d\Omega$. Both quantities – irradiance and radiance – can also be specified spectrally. Then the matching units are (W/m²/nm) and (W/m²/sr/nm), respectively.

The problem of calculating the propagation of sunlight through the atmosphere can be split into two parts, one for the direct radiation, i.e. the part of the radiation having not interacted with the atmosphere, and one for the diffuse radiation. This is reasonable since the diffuse radiation does not couple back to the direct radiation. However, the direct radiation serves as source for the diffuse radiation.

The direct solar irradiance I_{dir} can be calculated from the extraterrestrial flux I_s according to the *Beer-Bouguer-Lambert*¹ law as

$$I_{\text{dir}} = I_s \exp \left(- \int_0^s k_{\text{ext}}(s') ds' \right) \quad (2.2)$$

with k_{ext} the (volume-)extinction coefficient (in units of (m⁻¹)) and s the direct path along which the light has traveled through the atmosphere along the direction of incidence $\hat{\Omega}_0$ (comp. Zdunkowski et al., 2007, Eq. 2.32).

In this context we can also introduce the optical thickness τ which is usually defined as the vertical integral of the extinction coefficient k_{ext} over height z . However, decisive for the circumsolar radiation is the integral of the extinction coefficient along the line of sight between the observer and the sun (as in Beer's law). It is called slant path optical thickness

$$\tau_s = \int_{z_1}^{z_2} \frac{k_{\text{ext}}(z)}{\mu} dz \quad (2.3)$$

where μ is the cosine of the sun zenith angle θ_{sun} .

The diffuse solar radiation is described by an integro-differential equation (comp. Zdun-

¹For the sake of brevity commonly called Beer's law

kowski et al., 2007, Eq. 2.36) which is referred to as the radiative transfer equation (RTE):

$$\hat{\Omega} \cdot \nabla L_d = -k_{\text{ext}} L_d + \frac{\omega_0 k_{\text{ext}}}{4\pi} \int_{4\pi} P(\hat{\Omega} \cdot \hat{\Omega}') L_d(\hat{\Omega}') d\hat{\Omega}' + \frac{\omega_0 k_{\text{ext}}}{4\pi} P(\hat{\Omega}_0 \cdot \hat{\Omega}) I_{\text{dir}} \quad . \quad (2.4)$$

It describes the change of the diffuse radiance L_d along a direction of propagation $\hat{\Omega}$. $\hat{\Omega}$ and $\hat{\Omega}'$ are directional unit vectors. The single scattering albedo ω_0 relates the extinction coefficient to the scattering coefficient k_{sca} and to the absorption coefficient k_{abs} as

$$\omega_0 = \frac{k_{\text{sca}}}{k_{\text{ext}}} = 1 - \frac{k_{\text{abs}}}{k_{\text{ext}}} \quad (2.5)$$

and gives the relative amount of scattering on the extinction (Zdunkowski et al., 2007, Eq. (1.49)). The scattering phase function P describes how much of the light coming from the direction $\hat{\Omega}'$ is redirected to the direction $\hat{\Omega}$ in a scattering process. Since only randomly oriented particles are considered in this study, the bulk phase functions depend only on the cosine of the scattering angle $\cos(\theta_{\text{sca}}) = \hat{\Omega} \cdot \hat{\Omega}'$ (e.g. Hansen and Travis, 1974). The first term on the right side of the RTE (Eq. 2.4) gives the reduction of radiance through extinction, i.e. either absorption or scattering, out of the direction $\hat{\Omega}$. The second term is a source term describing the in-scattering of diffuse radiance from other directions $\hat{\Omega}'$ into direction $\hat{\Omega}$. The third term expresses the conversion of direct radiation into diffuse radiation through scattering.

Note that the presented equations are for monochromatic light. All optical parameters are wavelength dependent and the equations need to be solved for every wavelength individually (see also Sect. 3.4.3). Furthermore all variables depend on the location \vec{x} . The presented form of the RTE is stripped to include only processes relevant for the applications in this work. Emission of radiation which occurs in the atmosphere at considerable amounts only in the infra-red spectrum is neglected. The transfer of radiant energy from one wavelength to another (inelastic scattering) is also omitted, as well as it is ignored that light can occur in different polarisation states. For a derivation of the RTE and a more complete overview of atmospheric radiative transfer one may refer to Zdunkowski et al. (2007).

Although the presented version of the RTE resembles already a simplified model for the radiative transfer it still is difficult to solve. Analytically this can only be achieved if further drastic simplifications are applied. If a more realistic version of the RTE should be solved this must be done numerically. For this study the radiative transfer was simulated

utilizing the libRadtran software package (Mayer and Kylling, 2005). In Sect. 3.4.1 the two different RTE solvers from libRadtran which found application in this work are presented. Unless stated otherwise the plane parallel approximation and the closely connected independent column approximation are applied in all radiative transfer simulations in this study. The former indicates that the atmosphere is considered to consist of parallel slabs in which the atmospheric properties do not change. That is variations are only considered in the vertical, such that the radiative transfer collapses to a one dimensional problem. Furthermore the curvature of the earth is ignored. The independent column approximation assumes that the radiative transfer within an atmospheric column, as probed for example by a satellite, is independent of the atmospheric properties of the neighbouring columns. In other words, the atmosphere is treated locally as one dimensional and the radiative transfer is calculated using the plane parallel approximation with periodic boundaries. In general, both approximations cause errors which increase with solar zenith angle: For low solar altitude, 3D-effects, like shadowing by clouds, are pronounced and the sphericity of the atmosphere has to be considered (see also discussion at the end of Sect. 3.2.3).

2.2 Scattering of Sunlight

Scattering describes the change of the propagation direction of light due to interaction with the medium. A recommendable review on scattering in planetary atmospheres was given by Hansen and Travis (1974), but let us briefly recapitulate the most relevant aspects concerning this study.

Forward scattering, that means a change of the propagation direction of at most a few degrees, is the phenomenon that causes the formation of an aureole in turbid atmospheres. Pronounced scattering in forward direction occurs on particles which are larger than the wavelength λ of the light. For particles much larger than λ , the extinction efficiency $Q_{\text{ext}} = \sigma_{\text{ext}}/A$ may become larger than one. σ_{ext} is the extinction cross-section and A is the geometrical cross-section of the particle. Accordingly Q_{ext} is the ratio of the actually extinct radiant flux to the radiant flux hitting the geometrical cross section of a particle (comp. Zdunkowski et al., 2007, Chap. 9.6). Q_{ext} can be as large as four but approaches two for very large particles. This so called “extinction paradox” exists because not only the light hitting the particle’s geometrical cross section is influenced but also the light bypassing the particle. This is due to the wave-nature of the light and can be described

by the diffraction theory. Therefore in the limit of large particles, the distribution of approximately 50% of the scattered radiant energy is described by diffraction theory. For the other half of the radiant energy, different methods, like for example geometric optics (e.g. Petty, 2006), need to be employed.

The diffraction pattern depends on the shape of the projected area of the scattering particle. Airy (1835) published a solution of the diffraction problem for circular apertures which is also valid for spherical particles. In general the diffraction pattern is proportional to the 2-dimensional Fourier transform \mathcal{F} of the projected area (Born and Wolf, 1999, chap. 8.3), so that the diffraction phase function P_{dif} can be written as (DeVore et al., 2013, Eq. 3):

$$P_{\text{dif}}(\theta_{\text{sca}}/\lambda, \phi) = \frac{2\pi}{A\lambda^2} |\mathcal{F}\{f_{\text{proj}}(x, y)\}|^2 \quad , \quad (2.6)$$

with θ_{sca} and ϕ being the scattering zenith and azimuth angle, respectively. f_{proj} is the pupil function and describes the particle's projection on a surface normal to the incident light. It is 1 inside the projection and 0 elsewhere.

In any case, diffraction predicts a primary peak of scattering into the forward direction. This peak becomes more and more focused the larger the particles are. As can be followed in Fig. 2.1, for a sphere the half-width-half-maximum of the forward peak is inversely proportional to the arcus sine of the sphere's radius r which can be approximated as $1/r$ for small angles.

While the diffraction theory can be used to predict the forward scattering peak of large particles, there is no uniform method to derive the complete scattering phase function ($\theta_{\text{sca}} = 0^\circ..180^\circ$) of ice crystals of arbitrary sizes and shapes (Yang et al., 2005). The optical property datasets for cirrus clouds used in this thesis are outlined in Sect. 3.1. They were created using an up-to-date combination of several methods.

For spherical particles, Mie theory (Mie, 1908) can be used to derive an exact solution of the scattering properties – including diffraction effects. The optical properties for aerosol used in this study are mainly based on Mie calculations (see Sect. 3.3).

In the limit of particles much smaller than λ (e.g. air molecules), Rayleigh theory (Lord Rayleigh (J. W. Strutt), 1871) can be applied which predicts only a weak directional

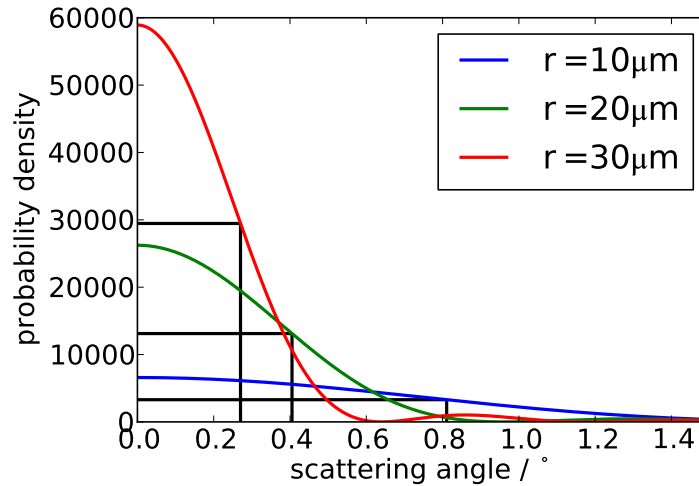


Figure 2.1: Detail of the diffraction phase functions at 550 nm for spheres with radii r of 10 μm , 20 μm and 30 μm . Black lines mark the half-width-half-maximum values at 0.81° , 0.41° and 0.27° , respectively.

dependence of the scattering. The phase function for Rayleigh scattering P_{ray} is (e.g. Hansen and Travis, 1974, Eq. 2.15):

$$P_{\text{ray}} = \frac{3}{4} (1 + \cos^2 \theta_{\text{sca}}) \quad . \quad (2.7)$$

As Fig. 2.2 shows the phase function varies only by a factor of 2 between sideways and forward or backward scattering. Therefore the radiation ending up in the circumsolar region is only a small part of the scattered radiation and the contribution of Rayleigh scattering to the circumsolar radiation can be neglected for the purposes of this study (see also Sect. 3.5).

2.3 Remote Sensing of Clouds from MSG

2.3.1 The SEVIRI Instrument

This study relies on data of the Spinning Enhanced Visible and Infra-Red Imager (SEVIRI) aboard the geostationary Meteosat Second Generation (MSG) satellites (Schmetz et al.,

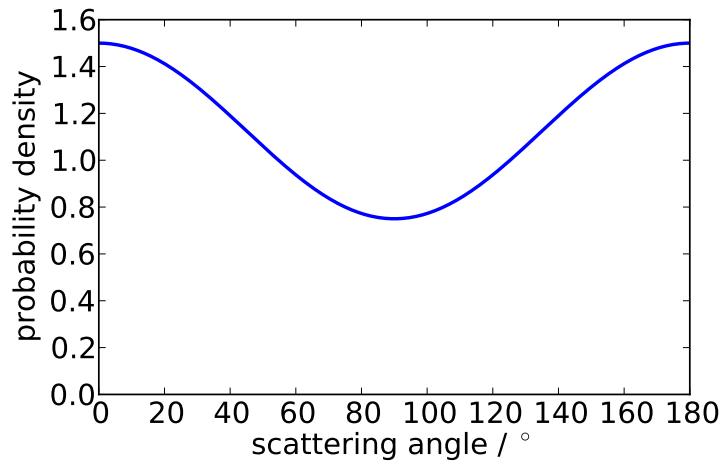


Figure 2.2: Phase function for Rayleigh scattering.

2002) for the remote sensing of clouds. It features eleven spectral channels in the visible and infrared spectrum with a sub-satellite-point sampling distance of 3 km and one broad band high-resolution channel in the visible spectrum (1 km sampling distance). From the geostationary orbit SEVIRI samples a large part of the earth which appears as disk on the images (comp. Fig. 2.3).

The MSG-satellites are spin stabilized – that is they rotate with 100 revolutions min^{-1} . The main instrument SEVIRI thereby scans the earth in lines from east to west – three lines at a time. A step motor driven mirror advances the focus of the imager by three lines from south to north with every revolution. A full scan takes about 12 minutes. Thereafter a calibration of the thermal channels and the repositioning of the mirror takes place so that the instrument can sample the full disk every 15 minutes. The images in the 11 standard channels feature 3712x3712 pixels. The time delay Δt between the start of the scan of the disk in the south and the probing of a certain pixel can therefore be approximated via the pixel’s line number N_l :

$$\Delta t \approx \frac{N_l}{3712} \cdot 12 \text{ min} \quad . \quad (2.8)$$

This becomes important when co-locating measurements of other instruments.

The main advantages of the instrument are the high sampling frequency combined with a good spatial resolution which allows to follow the temporal evolution of cloud properties anywhere within the MSG disk. The first MSG satellite (Meteosat 8) delivered operational

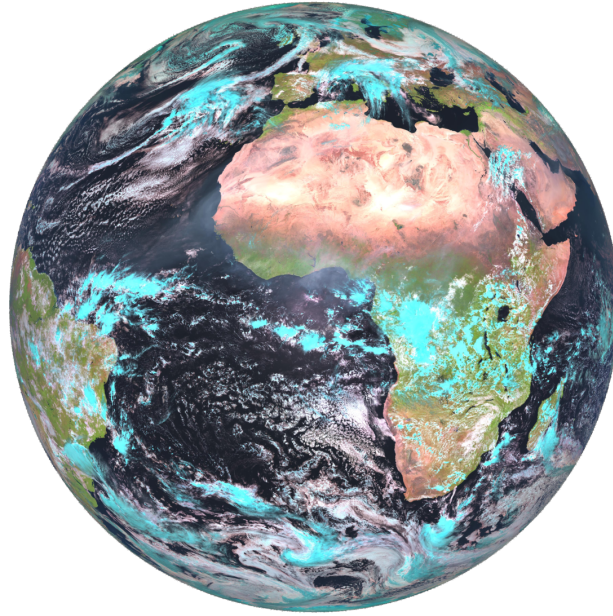


Figure 2.3: False-color composite image of one full SEVIRI scan – the sampled part of the earth is also called “MSG-disk”.

data from 2004 on. Currently Meteosat 10 is the main operational MSG satellite and with one further successor to be launched the MSG satellite family is expected to deliver consistent measurements until 2018.

Especially important in the context of this work are the SEVIRI channels 1 & 3 or “VIS006” & “NIR1.6”. They are centered at $0.635\ \mu\text{m}$ and $1.64\ \mu\text{m}$ and the lower and upper wavelength boundaries are $0.56\ \mu\text{m}$ and $0.71\ \mu\text{m}$, and $1.50\ \mu\text{m}$ and $1.78\ \mu\text{m}$ respectively. Typically the measurements in these channels are expressed as reflectivity or reflectance value R which is basically a normalized radiance:

$$R = \frac{\pi L d^2}{I_\lambda \cos(\theta_{\text{sun}})} \quad , \quad (2.9)$$

with L being the measured spectral band radiance, d the earth-sun distance in AU, I_λ the spectral band solar irradiance for the channel at 1 AU and θ_{sun} the sun zenith angle at the considered location (EUM MET TEN 12 0332).

It should be noted that SEVIRI is operated with an over-sampling strategy: While the sampling distance is 3 km at nadir, the resolution is only about 4.8 km. As sampling is

performed with constant angular stepping, this resolution decreases for off-nadir measurements. Furthermore the registration of satellite pixels to latitude/longitude values may deviate by up to 3 km at nadir with a image-to-image root-mean-square-value of 1.2 km (Schmetz et al., 2002). These limitations must be kept in mind for example when comparing SEVIRI data to ground based measurements as in Sect. 4.2.2.

A test sector of 189x252 satellite pixels within the whole MSG disk was defined (see Fig. 2.4). The evaluation of SEVIRI measurements was limited to this sector for the sake of reduced computing time and storage space. The sector includes the southern part of the Iberian Peninsula where recently the construction of concentrating solar power plants flourished. Currently approximately 40 solar power plants are in operation in this area. Also the CST research center Plataforma Solar de Almería (PSA) is inside the sector, as well as parts of northern Africa, where an increasing amount of CST projects are planned. The chosen area includes Mediterranean as well as desert climate zones and should therefore offer suitable test conditions. Ocean pixels and pixels containing continental water surfaces were excluded from evaluation using a land/water mask from the EUMETSAT Land Surface Analysis Satellite Applications Facility (LANDSAF).

2.3.2 Retrieval of Cloud Properties from Reflected Solar Radiation

The Algorithm for the Physical Investigation of Clouds with SEVIRI (APICS) is used in this study to derive cloud properties from the SEVIRI measurements. APICS is an implementation of the method developed by Nakajima and King (1990) for SEVIRI. The method uses measurements of reflected solar radiation to retrieve the optical thickness and the effective radius r_{eff} of clouds.

The effective radius is a parameter that is commonly used to characterize the scattering and absorption properties of disperse particle size distributions by means of a single scalar (Hansen and Travis, 1974; McFarquhar and Heymsfield, 1998). For spherical particles like water droplets it is defined as the ratio of the third to the second moment of the size distribution. There is however an ambiguity in the definition of r_{eff} for non-spherical particles. In this study it is defined as

$$r_{\text{eff}} = \frac{3 \int V(\hat{L})n(\hat{L})d\hat{L}}{4 \int A(\hat{L})n(\hat{L})d\hat{L}} \quad (2.10)$$

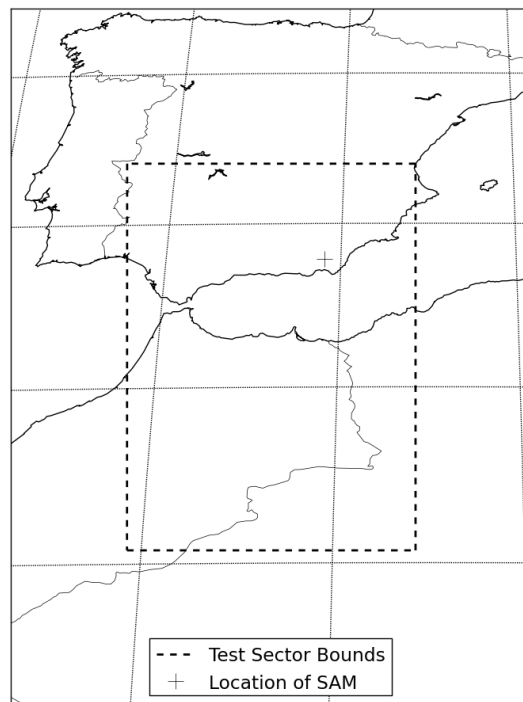


Figure 2.4: Map covering the test sector. SEVIRI pixels are evaluated inside the sector over land only. The cross marks the location of the the research center Plataforma Solar de Almería.

where n is the number concentration, \hat{L} the maximum dimension, V the volume and A the projected area of the particles. This definition was also used in the generation of the utilized cirrus bulk optical properties (e.g. Baum et al., 2005a) which are described in Sect. 3.1.

The method by Nakajima and King (1990) exploits the spectral course of the absorption coefficient of water and ice. While cloud particles in the visible part of the spectrum basically solely scatter sun light, they also absorb light in the infrared. The mean path length traveled by light through a cloud particle during a scattering event depends on the particle size. Alike, the absorption depends on the particle size. This is reflected in the single scattering albedo ω_0 which is basically 1 in the visible part of the spectrum independent of particle size but < 1 with a dependence on r_{eff} in the infrared (comp. Fig. 2.5). Thus, a measurement of reflected sun light in the visible is only sensitive to the amount of scattering by the cloud particles and therefore the optical thickness. A measurement in the infrared is sensitive to both, scattering and absorption. It therefore contains information about the optical thickness and the particle size. By performing a measurement in both parts of the spectrum, one can unravel both informations. For now we leave it at reading from Fig. 2.5 that the SEVIRI channels² 1 & 3 can be used to perform such a retrieval. The technical details of the APICS retrieval are outlined further down in Sect. 3.2.

2.4 Passive Satellite Remote Sensing of Aerosol

Aerosols scatter and absorb sunlight. The share that is backscattered into space can be used to remotely sense aerosol properties. However aerosol can be comprised of a large variety of particles in terms of sizes, material and shape. This diversity alone makes remote sensing challenging.

The signal reaching the satellite is affected not only by the aerosol but also by the atmosphere and often to large amounts by the surface. A rigorous cloud screening must be applied to the satellite measurements, else the aerosol amount will be overestimated. This is problematic since even sub-scale clouds or very thin clouds which are hard to detect will affect the retrieved aerosol properties. The surface reflectivity must be known precisely since it accounts for a large share of the reflected sun light. But even with a well charac-

²Filter functions in Fig. 2.5 from EUMETSAT document EUM/MSG/TEN/06/0010

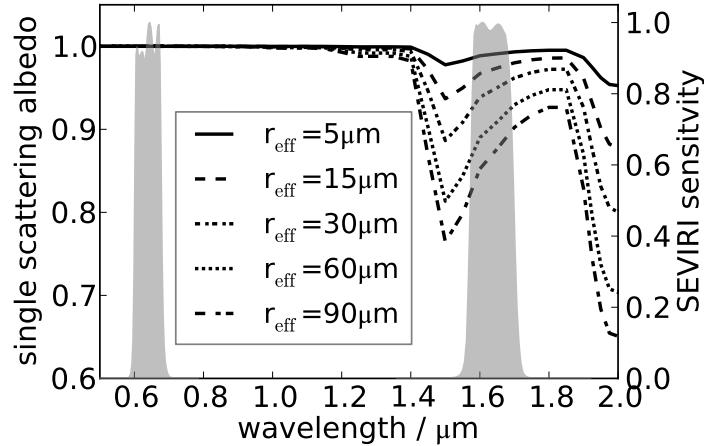


Figure 2.5: Spectral course of the single scattering albedo ω_0 for solid-column particle mixtures for different effective radii r_{eff} . Shown in grey are the filter functions for the channels 1 & 3 of the SEVIRI instrument aboard Meteosat-8.

terized surface reflectivity it can be hard to retrieve aerosol properties. This is the case if the aerosol has similar scattering and absorption characteristics as the surface: While over a dark surface like the ocean aerosol will increase the satellite-measured reflectivity, it may – depending on the aerosol absorption – decrease the reflectivity over bright surfaces like snow or ice. In between, the sensitivity of the satellite-measured reflectivity on the atmospheric aerosol load becomes zero. This is often the case for desert regions: Uplifted dust over a desert can be hardly quantified.

Today's retrievals which go beyond the determination of the optical thickness alone use a synergy of measurements, that is multi-angle, multi-spectral and polarized measurements. This way some information about the aerosol type and size distribution can be obtained. However even these sophisticated retrievals do not provide full global coverage. For example the SYNAER retrieval, which is a multi-spectral retrieval for the aerosol optical thickness and aerosol type, does not work over deserts and the aerosol type is only given if the aerosol optical thickness is larger than 0.1 (Holzer-Popp et al., 2008). Furthermore multi-angle or polarized measurements are performed only from low earth orbit satellites such that the temporal resolution of today's sophisticated aerosol retrievals is typically in the order of days.

To obtain a data set without gaps, that also contains data for arid regions which are of

special interest for CST, I decided to use modeled aerosol data from the Integrated Forecast System (IFS) of the European Centre for Medium-Range Weather Forecasts (ECMWF). The details concerning the model are outlined in Sect. 3.3.1.

2.5 The Sunshape

While a complete characterization of the instantaneous circumsolar radiation can only be given by a 2D radiance distribution, it is commonly reduced to a one-dimensional radial radiance profile assuming radial symmetry. Such a radial radiance profile from the center of the sun outward is called sunshape. It is an adequate simplification if scattering is caused within atmospheric layers that are horizontally homogeneous within the field of view. At large sun zenith angles θ_{sun} , a 1D profile might not be appropriate, even for homogeneous conditions, as significant differences in the path length through the scattering layer occur, even within a small field of view.

The projection of a circular field of view onto a horizontal (scattering) layer is an ellipse. It has two length scales L_1 and L_2 corresponding to its major and minor axis. Both depend on the elevation of the scattering layer H and on the sun zenith angle θ_{sun} :

$$L_1 = H / \tan(90^\circ - \theta_{\text{sun}} - \alpha_{\text{cir}}) - H / \tan(90^\circ - \theta_{\text{sun}} + \alpha_{\text{cir}}) \quad (2.11)$$

$$L_2 = 2 \sin(\alpha_{\text{cir}}) H / \cos(\theta_{\text{sun}}) . \quad (2.12)$$

Figure 2.6 shows that, even if only a field of view with $\alpha_{\text{cir}} = 2.5^\circ$ is considered, the length scales can be in the order of several kilometers for cirrus clouds at an elevation of $H = 12$ km. Cirrus clouds normally show variability on smaller scales so that a sunshape is in general not a good representation of the instantaneous 2D radiance distribution around the sun. It is therefore advisable to temporally average sunshapes measured from the ground since advection of the clouds through the field of view will normally smooth the average radiance distribution.

For aerosols the sunshape is a better representation of the instantaneous 2D radiance distribution for two reasons. First, aerosols normally show considerably less horizontal variability than cirrus clouds. And second, most of the aerosol is constricted to the boundary layer which has only a few kilometers vertical extent at most, so that often the length

scale of the field of view is a magnitude smaller than for cirrus clouds.

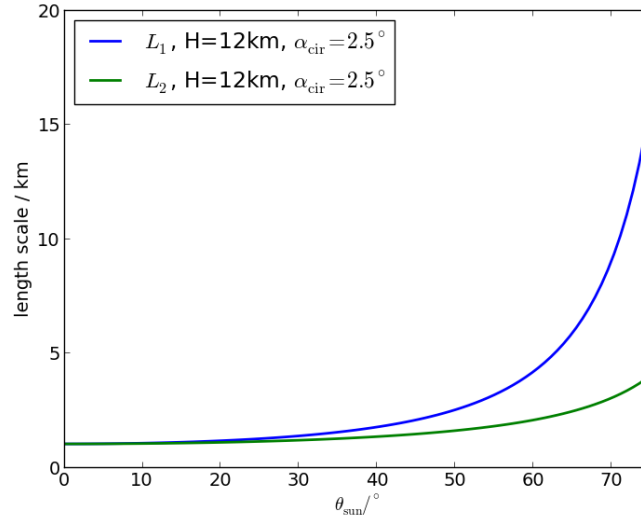


Figure 2.6: Length of the major and minor axis of the ellipse that forms as a circular field of view with $\alpha_{\text{cir}} = 2.5^\circ$ intersects a horizontal layer at 12 km elevation under different sun zenith angles.

Figure 2.7 shows exemplary three sunshapes simulated with the radiative transfer solver MYSTIC (see Sect. 3.4.2). In case of a clear atmosphere the radiance inside the sun disk features the highest values compared to the other simulations, while it exhibits the lowest values in the circumsolar region. After adding an aerosol layer to the simulation the radiance inside the sun disk decreases by $\approx 40\%$, while in the circumsolar region it increases by approximately two magnitudes. If the aerosol is replaced by a cirrus layer of the same optical thickness, the sunshape looks quite different in the circumsolar region: Close to the sun the radiance is once more increased by about two magnitudes but falls off much more steeply with increasing angular distance to the sun. This difference in the sunshapes reflects the different particle sizes: The ice particles are larger than the aerosol particles, therefore the forward peak in their scattering phase function is more focused. To give the reader an impression of corresponding irradiance values, the sunshapes were integrated over three angular intervals; once over the sun disk ($0.0^\circ - 0.266^\circ$), once over the circumsolar region up to 1.0° from the sun center and once over the annular region from 1.0° to 2.5° from the sun center. While 1.0° is meant to represent the field of view of a CST receiver, 2.5° is the opening half-angle standard of pyrhemometers by the World

Meteorological Organisation (WMO) (CIMO Guide). Table 2.1 lists the results of the integration in W/m^2 . The cirrus with the pronounced forward scattering peak produces higher irradiance values than the aerosol layer, especially within the sun disk and the circumsolar region closely around the sun. Compared to aerosol or clouds, air molecules only cause negligible irradiance in the circumsolar region.

Considering once more the sunshapes in Fig. 2.7 one can realize that the brightness in the sun disk itself ($\alpha < 0.266^\circ$) is not distributed evenly. The center is brighter than the rim. This effect is called limb darkening. It is not only caused by the terrestrial but rather by the solar atmosphere: Most of the sun light reaching the earth is emitted in the photosphere of the sun, which besides emission also shows strong absorption of light. As the sun is a sphere, light reaching the earth from the “rim” travels along a slanted path through the photosphere, while light from the disk center exits the photosphere perpendicular. The mean depth in the photosphere, from which light reaching the earth originates, decreases therefore from the disk center to the rim. The temperature and therefore also the emission of light in the photosphere increases with depth. Therefore the sun disk appears brighter in the center than at the rim (Scheffler and Elsässer, 1990). The implementation of the limb darkening effect in the radiative transfer solver MYSTIC is outlined in Sect. 3.4.2.

Table 2.1: Shortwave integrated irradiance values for the three sunshape simulations shown in Fig. 2.7. Values are given for the sun disk ($0.0^\circ - 0.266^\circ$), the circumsolar region extending to 1.0° angular distance from the sun center and an annular region extending from 1.0° to 2.5° angular distance from the sun center.

| | $0.0^\circ - 0.266^\circ$ | $0.266^\circ - 1.0^\circ$ | $1.0^\circ - 2.5^\circ$ |
|---------------|---------------------------|----------------------------|----------------------------|
| Rayleigh atm. | 998 W/m^2 | 0.01 W/m^2 | 0.06 W/m^2 |
| Dust aerosol | 621 W/m^2 | 3.2 W/m^2 | 11 W/m^2 |
| Cirrus | 684 W/m^2 | 90 W/m^2 | 20 W/m^2 |

2.6 The Circumsolar Ratio – CSR

The characterization of the circumsolar radiation can be simplified further by introducing a scalar quantity – the circumsolar ratio (CSR). It is defined as the normal irradiance coming from an annular region around the sun divided by the normal irradiance from this circumsolar region and the sun disk. For the remainder of the document the term irradiance always refers to normal irradiance, i.e. irradiance on a surface perpendicular

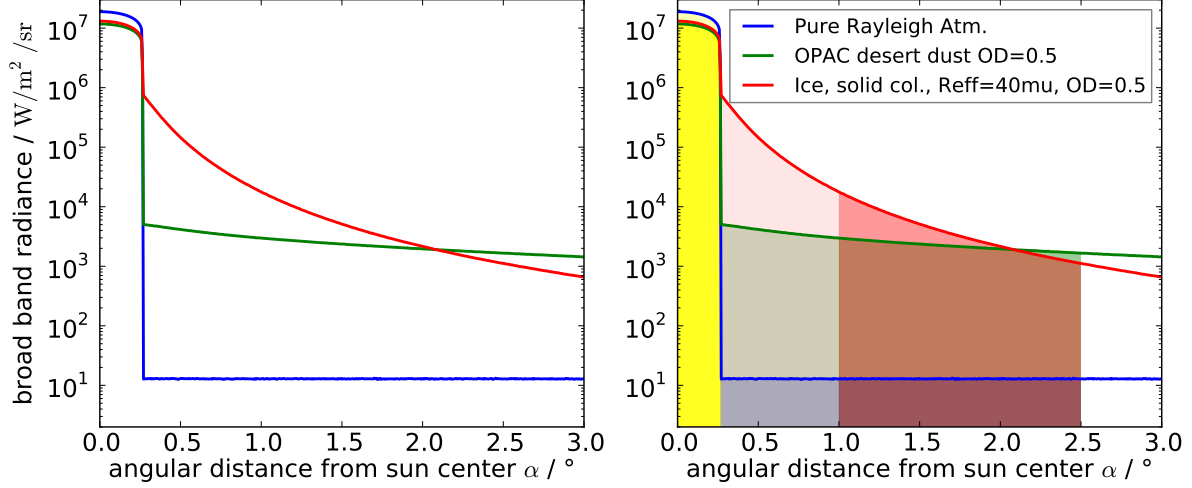


Figure 2.7: Left panel: MYSTIC simulation of sunshapes for three atmospheric situations (MYSTIC, see Sect. 3.4.2). A pure Rayleigh atmosphere (only molecules, blue), with a layer of OPAC desert dust aerosol (see Sect. 3.3.2) with an optical thickness at 550 nm of 0.5 (green) or with a cirrus composed of solid-columns (see Sect. 3.1) with $r_{\text{eff}} = 40 \mu\text{m}$ (red). Right panel: Same as left but the circular/annular regions marked for which irradiance values are given in Tab. 2.1.

to the direction pointing at the sun. The disk angle α_{sun} gives the extent of the sun disk measured from its center to the edge. The circumsolar region reaches from the sun's edge to the angle α_{cir} ($> \alpha_{\text{sun}}$) which is subject to arbitrary definition and measured from the sun's center as well. With this we can write

$$\text{CSR}(\alpha_{\text{cir}}) = \frac{\int_0^{2\pi} \int_{\alpha_{\text{sun}}}^{\alpha_{\text{cir}}} L(\alpha) \cos(\alpha) \sin(\alpha) d\alpha d\phi}{\int_0^{2\pi} \int_0^{\alpha_{\text{cir}}} L(\alpha) \cos(\alpha) \sin(\alpha) d\alpha d\phi} \quad (2.13)$$

where L is the sunshape – i.e. the radiance depending on the angular distance α from the sun center. The cosine term is safely neglected in the following since even for the maximum α_{cir} of 5° considered in this study the errors due to this are smaller than 0.2%. This estimate was derived by evaluating the error for a worst case sunshape which does

not decrease with increasing distance to the sun but stays constant ($L = \text{const}$). The error is in this case

$$\frac{\int_{0^\circ}^{5^\circ} (1 - \cos \alpha) \sin \alpha \, d\alpha}{\int_{0^\circ}^{5^\circ} \cos \alpha \sin \alpha \, d\alpha} = 0.2\% \quad . \quad (2.14)$$

Buie et al. (2003) approximated the sunshape in the circumsolar region as a power-law function which can be considered a line in a log-log diagram. They developed a fit for the two parameters intercept and gradient of this function in terms of the CSR, based on broad band solar integrated field measurements of the sunshape. Within the sun disk ($\alpha \leq 4.65 \text{ mrad} = 0.266^\circ$) they used a fixed shape. In total they parameterized the normalized sunshape Φ as

$$\Phi(\alpha) = \frac{L(\alpha)}{L(\alpha = 0)} = \begin{cases} \exp(\kappa)\alpha^\gamma, & \text{for } \alpha > 4.65 \text{ mrad} \\ \frac{\cos(0.326\alpha)}{\cos(0.308\alpha)}, & \text{for } \alpha \leq 4.65 \text{ mrad} \end{cases} \quad (2.15)$$

with

$$\gamma = 2.2 \ln(0.52 \cdot \text{CSR}) \cdot \text{CSR}^{0.43} - 0.1 \quad , \quad (2.16)$$

and

$$\kappa = 0.9 \ln(13.5 \cdot \text{CSR}) \cdot \text{CSR}^{-0.3} \quad . \quad (2.17)$$

The angular distance to the sun center α is expressed in mrad. Employing this fit, the CSR can be used to characterize the sunshape, which is however not utilized in this study.

2.7 Ground Based Measurements of the Circumsolar Radiation

Circumsolar radiation in terms of the sunshape is intricate to measure because a high dynamic range, a good angular resolution and a precise sun tracking are required at the same time. A cornerstone of ground based circumsolar radiation measurement is the so called ‘‘LBL reduced data base’’ which contains about 180 000 sunshapes from 11 U.S. sites measured with four identical devices in the late 1970s and early 1980s (Noring et al., 1991). However LBL’s measurement system was a scanning telescope resulting in a rather low angular resolution of about 0.025° . More recently CCD camera based systems have

been developed allowing to capture the 2D radiance distribution at once in high angular resolution (e.g. Neumann et al., 1998; Neumann and Witzke, 1999; Ritter and Voss, 2000). Data from a system using a CCD camera is also used in this study to validate the results. This system is based on the sun and aureole measurement system (SAM) which was originally developed for the retrieval of cloud properties (DeVore et al., 2009) and is available commercially from Visidyne Inc.³. Apart from a SAM the system constitutes of a Cimel CE-318N EBS9 sun photometer and a dedicated post-processing software. The sun photometer is also part of the “Aerosol Robotic Network – AERONET” (Holben et al., 1998) and products from the AERONET processing scheme are also used later in the validation section (Sect. 4.2.1). SAM measures the sunshape at a wavelength selected with a filter. The post-processing software uses the additional information gathered by the sun photometer to convert this spectral sunshape to other wavelengths or to broad band solar integrated values. Furthermore, this software also calculates CSR values from the obtained radiance profiles. Sunshapes simulated with the adapted MYSTIC version (Sect. 3.4.2) have been used to validate the post-processing. The system and its validation is described in detail in Wilbert et al. (2013). For the sake of brevity it will be called SAMS (for SAM based System) in the following. While in principle three SAMSs exist (one at the Plataforma Solar de Almería, Tabernas, Spain, one in Odeillio, France, and one in Masdar, Abu Dhabi), only the data of the system in Tabernas were used (location marked in Fig. 2.4). The quality assurance of the SAMS data is an elaborate process and only the intensive contact with Stefan Wilbert – the principal investigator of the Tabernas SAMS – allowed to detect and remove some erroneous values in the original dataset. SAMS data from the years 2011 and 2012 have been used in this study. Before 04 Jul. 2011 SAMS was operated with a 670 nm filter which was then replaced by a 870 nm filter. The SAMS dataset provided by Stefan Wilbert also includes DNI and GHI from the collocated meteorological station at the PSA.

Pursuing the goal of making circumsolar radiation measurements cheaper and less maintenance dependent, some studies have been presented recently which show the potential of new circumsolar radiation instruments: Wilbert et al. (2012) investigated a pyrhelimeter-like instrument which allows to measure with different sized apertures. Kalapatapu et al. (2012) presented a sunshape profiling irradiator which is based on the principle of the rotating shadowband radiometer.

³<http://www.visidyne.com>

Chapter 3

Tools and Methods

This chapter deals with the utilized and developed tools and methods. First, the optical property datasets for cirrus clouds which found application are described in Sect. 3.1. In the following Sect. 3.2 the APICS cloud property retrieval framework is introduced and achieved improvements are outlined. Next, the aerosol input from ECMWF's IFS and its processing is specified in Sect. 3.3. Section 3.4 motivates the use of the radiative transfer solver MYSTIC in this study and outlines how it was adapted. Section 3.5 is of special importance, as the method to parameterize circumsolar radiation is developed therein. Finally, Secs. 3.6 & 3.7 provide sensitivity studies concerning the shape of the scattering particles and the hygroscopic growth of aerosol, respectively.

3.1 Optical and Microphysical Properties of Cirrus Clouds

The ice crystals within cirrus clouds feature a variety of shapes. The particle shape influences the optical properties of the ice crystals like the scattering phase function and the single scattering albedo. This in turn influences the modelling of the circumsolar radiation as well as the cloud property retrieval which in the end is based on radiative transfer modelling as well. Passive satellite instruments with only one viewing direction do not provide information about the ice particle shape composition within a cloud. Therefore it has to be assumed a priori.

To be able to assess the uncertainty that is caused by this assumption, a range of different

cloud bulk optical properties were used in this study for the modelling of the circumsolar radiation as well as for the cloud property retrieval. Optical properties for clouds featuring a realistic particle shape mixture were considered as well as for clouds composed of particles of only one single shape. While the latter are not necessarily a realistic assumption they are meant to represent the extremes in the natural variability of the cloud’s composition.

The particle mixtures and associated optical properties are described in Baum et al. (2005a), Baum et al. (2005b) and Baum et al. (2011). In the following the older version is referred to as “Baum v2” and the newer version as “Baum v3.5”. The latter mixture incorporates more particle shapes and the particle surface is “severely roughened” while “Baum v2” is composed of particles with smooth surfaces. The five different single particle shapes that are considered in this study comprise solid- and hollow-columns, aggregates composed of eight hexagonal columns, planar bullet rosettes, and droxtals. They all have smooth surfaces like in “Baum v2”. Hong Gang created single scattering properties using the improved geometric optics method (Yang et al., 2000) for these particles – valid for narrow size bins. From these Claudia Emde computed bulk optical properties by integrating the binned single scattering properties over gamma size distributions

$$n(D) = ND^{\frac{1}{b}-3} \exp\left(-\frac{D}{ab}\right) \quad , \quad (3.1)$$

with the parameters a and b . N is a normalisation constant and the measure of particle size D is defined as

$$D(\hat{L}) = \frac{3V(\hat{L})}{2A(\hat{L})} \quad , \quad (3.2)$$

where \hat{L} is the maximum dimension, V the volume and A the projected area of the particles. The parameter b was fixed to 0.25 while a was iteratively determined such that the size distribution yields the desired effective radius (Eq. 2.10) (pers. comm. Claudia Emde, 2012, Bugliaro et al., 2013). Correspondent to the contributors Hong, Emde, Yang the optical properties for the individual particle shapes are referred to under the acronym HEY. All optical property datasets cover an effective radius range of $5 \mu\text{m} - 90 \mu\text{m}$, except for “Baum v3.5” which only extends from $5 \mu\text{m} - 60 \mu\text{m}$.

3.2 Cloud Property Remote Sensing with the APICS Algorithm

The following section gives an overview of the APICS cloud property retrieval and outlines how it was modified during this study to improve the retrieval in regard to optically thin cirrus. The section is partly adapted from Reinhardt et al. (2013).

3.2.1 Algorithm Description

This study relies on the “Algorithm for the Physical Investigation of Clouds with SEVIRI“ (APICS) framework to derive effective radius and optical thickness of cirrus clouds. APICS (Bugliaro et al., 2011, 2012, 2013) implements a cloud property retrieval based on Nakajima and King (1990) (basic principle see Sect. 2.3.2) for the SEVIRI channels 1 and 3 in the solar spectrum (centered at 0.6 μm and 1.6 μm).

The cloud property retrieval uses lookup tables (LUTs) in which pre-simulated reflectivity values for the two SEVIRI channels (R006 & R016) are stored as a function of the most relevant parameters, namely as a function of the sun and satellite zenith angles, the relative azimuth between sun and satellite, the albedo in both channels, the particle size in terms of the effective radius and the optical thickness. For each ice particle shape (mixture) an individual LUT is used. Simplifications and assumptions about the state of the atmosphere are required, because the two independent pieces of information (the two satellite channels) allow the retrieval of only two quantities, in our case optical thickness and effective radius.

In principle the retrieval returns the (τ, r_{eff}) -combination which minimizes the residual between the pre-calculated and measured reflectivity values, which is calculated as (Bugliaro et al., 2013)

$$\chi^2 := \left(\frac{R006_{\text{meas}}}{R006_{\text{lut}}} - 1 \right)^2 + \left(\frac{R016_{\text{meas}}}{R016_{\text{lut}}} - 1 \right)^2 . \quad (3.3)$$

The user can choose between different algorithms to minimize χ^2 . For this study APICS was operated with an “Powell’s Dog-Leg”-algorithm which was adapted from Madsen et al. (2004) (pers. comm. Luca Bugliaro, 2013). It is a fast iterative algorithm to find a local minimum. The LUTs are interpolated between the supporting points; for this study the retrieval was setup to use a spline interpolation.

For the operation of APICS in this study it was assumed that the channels 1 and 3 of the

SEVIRI instrument aboard the operative “Meteosat 9”-MSG satellite exhibit an underestimation of about 6% (Ham and Sohn, 2010) and an overestimation of 2% respectively (Pers. comm. Philip Watts, EUMETSAT, 2009). Therefore, a pre-processing step was applied to take care of the corresponding recalibration of reflectance values. Recently, Meirink et al. (2013) published similar calibration coefficients. In a satellite inter-calibration study they found an underestimation of 8% and an overestimation of 3.5% for the SEVIRI channels 1 and 3, respectively.

3.2.2 Auxiliary Albedo Dataset

While APICS was originally developed as a multi-purpose cloud property retrieval, it is especially important in the context of this study that optically thin cirrus clouds are retrieved at the best. To account for that, APICS was modified in a common effort of Luca Bugliaro and myself as described in the following.

The most important sources of uncertainty, considering thin ice clouds, are the a priori assumptions about the ground reflectivity, the aerosol properties and the ice particle shape. Figure 3.1 illustrates that a wrong assumption about the ground reflectivity can lead to large errors in the retrieved cloud properties, especially for clouds with $\tau < 5$. Both panels in the figure show excerpts of the lookup tables for albedo value combinations which were actually observed within the considered test sector (Fig. 2.4). The albedo combination in the left panel, for example, was observed for a densely forested region in Spain, just north of Gibraltar (Alcornocales national park), while the albedo combination in the right panel is typically observed for the desert regions in the south-east of the test sector. We adapted APICS such that initially existing problems concerning wrong assumption of the ground reflectivity are reduced.

APICS relies on the albedo to describe the ground reflectivity – that is, isotropic ground reflection is assumed. The albedo must be determined a priori for both SEVIRI channels at every pixel. The original version of APICS used albedo products based on measurements of the Moderate Resolution Imaging Spectroradiometer (MODIS) aboard polar orbiting satellites – either the “blacksky” or “whitesky” albedo from the Ambrals processing scheme (Strahler et al., 1999). Now we modified APICS so that it generates its own self-consistent albedo product. This product is based on the SEVIRI “Clear Sky Reflectance Map”, which is the average of the reflectance for a given time of day over the seven preceding days under clear sky conditions (EUM OPS DOC 09 5165). The clear sky reflectance contains

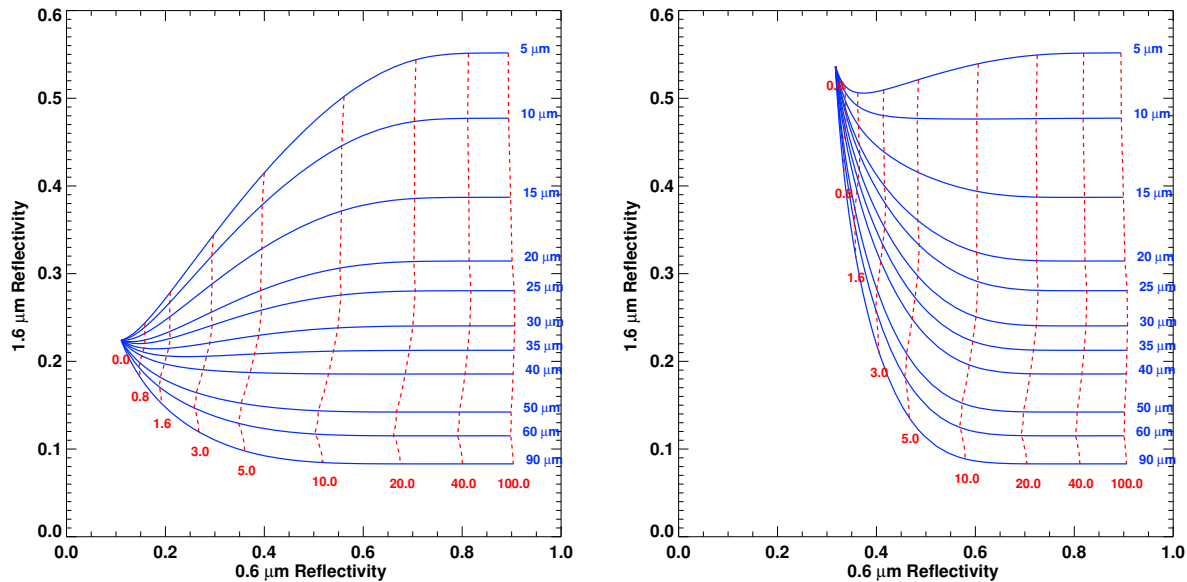


Figure 3.1: Details of the APICS lookup table for “Baum v2” for a sun zenith angle of 30° , a relative azimuth between sun and satellite of 20° and a satellite zenith angle of 41.4° . Blue: Lines of equal effective radius. Dashed red: Lines of equal cloud optical thickness τ . Left panel: Albedo combination for the $0.6 \mu\text{m}$ and $1.6 \mu\text{m}$ -channels of $(0.10, 0.25)$. Right panel: Albedo combination of $(0.35, 0.60)$. Plotting script courtesy of Luca Bugliaro.

contributions from the ground as well as from the atmosphere. From this combined signal the ground albedo needs to be extracted. The albedo values in both SEVIRI channels are therefore retrieved using the APICS lookup tables. To this end it is evaluated for which albedo the pre-simulated reflectivity values match the clear sky reflectance best, where $\tau = 0$. This procedure has the advantage of being consistent with the cloud property retrieval concerning atmospheric gas composition, radiative transfer modelling and instrument calibration. Furthermore we assume that the thus retrieved albedo also corrects for some of the long term variability in the aerosol properties which may deviate from the constant aerosol properties used in the simulations for the APICS lookup tables. Long term variability here denotes changes on the scale of a few days to one week and which are therefore slow enough to influence the clear sky reflectance averaged over seven days. The “Clear Sky Reflectance Map” is routinely only available for 12 UTC. Therefore the albedo is only retrieved at this time and used for the whole day. Nevertheless the success rates (defined in the following) reached by APICS with this method are superior compared to using the MODIS albedo datasets. In principle one could develop a product alike the

“Clear Sky Reflectance Map” with a day-of-time dependence, but this was assessed to be beyond the scope of this study.

Because of the uncertainties in the a priori assumptions described above and because of other insufficient projections of the reality (e.g. 1D radiative transfer calculations) the cloud property retrieval results can be erroneous. Often the measured reflectivity pair cannot even be reproduced by any parameter combination in the lookup tables. In these cases the retrieval will return a (τ, r_{eff}) combination from the “edge” of the LUT and χ^2 – although minimized – will differ from zero. Let us call these occurrences “outliers”. Please note that the definition of outliers is very strict. In principle one could add all those data points to the “hits”, which lie within the uncertainty range of the retrieval due to errors in the measurements and in the assumptions. These errors are, however, difficult to quantify. Since the number of outliers is used in the following only as a relative quality criterion, the exact definition is not relevant. The success rate of the cloud property retrieval S is defined as one minus the ratio of the number of outliers to the total number of considered pixels in a scene.

$$S = 1 - \frac{\text{outliers}}{\text{considered pixels}} \quad (3.4)$$

The success rate was calculated for four months of SEVIRI measurements within the test sector (see Fig. 2.4), which should be characteristic for the four different seasons (Jun/2011, Sep/2011, Dec/2011 and Mar/2012). The average success rates are 62%, 62% and 81% for the MODIS “blacksky”, MODIS “whitesky” and the APICS-generated albedo respectively when using the “Baum v2” optical properties. Considering the better values with the APICS-generated albedo, APICS was operated with this new albedo product for the retrieval of circumsolar radiation. Note that success means the retrieval obtained values, which need not be correct, though. It was decided to include the “outliers” in the circumsolar radiation calculations with the (τ, r_{eff}) combination that APICS returns because they are the best possible result for a given set of measurements.

As one can see from the not perfect success rate this approach attenuates the problems with wrong a priori assumptions but does not solve them completely. The APICS-generated albedo product can adapt to changes of the real surface albedo only on the scale of a few days while the real changes – e.g. due to precipitation – can be on the scale of hours. Further reading on the influence of inhomogeneous surface albedo on Nakajima & King-like cloud property retrievals can be found in Fricke et al. (2012).

3.2.3 Cirrus Cloud Mask

The APICS retrieval is only performed for pixels classified as cirrus. This is mandatory since else a measurement of increased reflectivity compared to the pre-computed clear sky value at $0.6\ \mu\text{m}$ will be misinterpreted by the algorithm as a cirrus cloud, even if the considered pixel is completely cirrus free. Such increased reflectivity values can, for example, be caused by high aerosol loadings or water clouds.

APICS originally relied on a cirrus cloud mask generated by the “Meteosat Second Generation Cirrus Detection Algorithm” v2 (MeCiDa) (Krebs et al., 2007; Ewald et al., 2013). However, it was foreseen that the retrieval of circumsolar radiation would benefit if the cirrus cloud mask used in conjunction with APICS was improved considering the detection efficiency of optically thin clouds. During the course of this study another cirrus cloud property retrieval algorithm was developed at DLR, which is called “Cloud Optical properties derived from CALIOP and SEVIRI” (COCS) (Kox et al., 2011; Kox, 2012). It is very sensitive to optically thin cirrus clouds and was finally used to replace the original cirrus cloud mask algorithm.

COCS uses a neural network approach to convert the measurements in the infrared channels of SEVIRI into the two parameters ice optical thickness and cloud top pressure. The neural network was trained with a collocated dataset of SEVIRI observations and retrieval results for the “Cloud-Aerosol Lidar with Orthogonal Polarization” (CALIOP) aboard the polar orbiting satellite CALIPSO¹. CALIOP is very sensitive to cirrus clouds and therefore the neural network delivers especially good results for thin clouds with $\tau < 1$. However the effective radius, which has strong influence on the circumsolar radiation (see Sect. 3.6), is not retrieved. Furthermore, in an intercomparison of retrieved optical thickness between COCS and APICS, COCS showed a distinct bias to lower optical thickness for cirrus clouds for which APICS retrieved $\tau > 1$. Because COCS is known to saturate at $\tau \approx 2.5$ (Kox, 2012), I assume that the optical thickness from APICS is more reliable for clouds with $\tau > 1$. For these reasons, the output from COCS was only used to generate a cloud mask for APICS.

Ostler (2011) and Bugliaro et al. (2012, 2013) computed the detection efficiency η_{det} of MeCiDa utilizing airborne LIDAR observations. MeCiDa detects virtually all of the cirrus clouds with $\tau > 0.5$ but only about 50% at $\tau \approx 0.2$. For most CST applications only clouds

¹Cloud-Aerosol Lidar and Infrared Pathfinder Satellite Observations

with a slant path optical thickness $\tau_s = \tau / \cos(\theta_{\text{sun}})$ smaller than 3.0 are relevant (with θ_{sun} being the sun zenith angle), otherwise too much light is extinguished in order to allow for energy production. Therefore, clouds with $\tau < 0.5$ account for a good share of the relevant clouds. The same studies show that COCS has advantages in detecting these clouds and reaches a detection efficiency of 80% even at $\tau = 0.15$ while the detection efficiency of MeCiDa falls below 80% already between $\tau = 0.3$ and $\tau < 0.4$. It was therefore decided to derive a cloud mask from COCS results. All pixels that are assigned an optical thickness larger than 0.1 by COCS are assumed to be cloudy. This cut-off criterion of $\tau > 0.1$ is necessary to keep the false alarm rate (FAR) at an acceptable level. Kox (2012) assessed the false alarm rate to be 5% for this cut-off using CALIOP observations as reference. The impact of the change from MeCiDa to COCS on derived circumsolar radiation is discussed in Sect. 5.2.1.

It should be kept in mind that there is no universally valid method to generate a cirrus cloud mask. Different methods differ in detection efficiency and false alarm rate. Often a higher detection efficiency goes along with increased false alarm rate. Furthermore these quality measures are subject to almost arbitrary definition: Consider only the treatment of satellite pixels that contain water and ice clouds at the same time. Should they be classified as cirrus cloud or not? This definition alone will strongly influence η_{det} and the FAR of any algorithm. The approach in this study was to detect as many cirrus clouds as possible and at the same time to minimize the impact of false detections – which is possible only to a certain extent: The re-calibration of the SEVIRI measurements and the new albedo product help to minimize misinterpretation in clear sky conditions. However, they do not address the problems with water clouds (see also Sect. 4.2.2).

Because COCS uses SEVIRI’s infrared channels, it is independent of the sun’s position. The APICS cloud property retrieval however relies on reflected sun light, which causes deteriorations at sunrise and sunset as the plane parallel and the independent column approximation break down. Loeb et al. (1997) showed that for broken clouds with high vertical extent or for stratiform clouds with bumpy cloud tops the plane parallel approximation causes considerable errors even for sun zenith angles as small as 65° . However, in a previous study Loeb and Davies (1997) concluded that the errors are in general less pronounced for optically thin clouds. In this study APICS results are used for sun zenith angles up to 80° . This can be justified as the considered cirrus clouds are optically thinner and, as I assume, normally more homogeneous than the strato-cumulus like synthetic clouds investigated by Loeb et al. (1997).

3.3 Aerosol Input and Processing

3.3.1 Modeled Aerosol Data from the ECMWF IFS

The aerosol data from which circumsolar radiation was derived in this study stem from the Integrated Forecast System (IFS) of the European Centre for Medium-Range Weather Forecasts (ECMWF). It is a global weather model which incorporates prognostic aerosol variables. These variables are also considered in the data assimilation process used to initialize the model: Besides satellite-measured reflectivity values at aerosol-relevant wavelengths, the MODIS aerosol optical depth product at 550 nm (Collection 5) is assimilated.

The IFS was chosen for several reasons: It provides global coverage; it has large support of the scientific community and several major scale projects rely on it (GEMS, MACC, MACC II); furthermore it serves as driver for several local air quality models who use the IFS output as boundary condition. Therefore there has been quite some effort to validate the model (Mangold et al., 2011; Bouarar et al., 2012; Benedictow et al., 2012). The most important point is the assimilation of remote sensed aerosol data: Thanks to it, the MODIS aerosol optical thickness (AOT) should be well represented in the model results. Where however no information from satellite is available, the model parameterizations and physics step in to fill the gap. Mangold et al. (2011) conclude that the assimilation of the MODIS AOT significantly improves the model performance especially concerning AOT-peaks and in general even over areas without MODIS data (bright desert surfaces). This is especially important since many regions of interest for CST applications have arid/desert climate. The IFS does not predict the aerosol particle size explicitly, which is a crucial parameter for the circumsolar radiation. However, the concentrations of several aerosol types with (fixed) size distributions are calculated – where appropriate even subdivided into several size bins (Sect. 3.3.2). The linear combination of these aerosol types thus implicitly holds the information about the aerosol particle size.

Aerosol is represented as different types in the IFS (dust, sea salt, organic matter, black carbon and sulphate). The generation of dust and sea salt aerosol is parameterized from model variables which are basically the 10 m-wind speed plus surface characterizing variables for dust, for example the soil moisture. The other aerosol sources are independent of the meteorology and stem from emission inventories. For the removal, dry and wet deposition is considered consistent to the meteorological variables. The aerosol types containing

large particles, namely dust and sea salt, are represented via three size bins so that a coarse differentiation in settling speed can be achieved. Furthermore the hygroscopic shares of the aerosols are allowed to grow with increasing relative humidity. This short description of the aerosol modelling within the IFS sums up only the most relevant facts of the detailed description from Morcrette et al. (2009).

The data used in this study for the validation of the method (Sect. 4.2.1) stem from a so called “near real time” (NRT) forecast performed with the IFS. It has the drawback that the complete set of model variables is not available as output. The information on relative humidity is not included. However, the re-analysis dataset, which would be preferable and which was intended to be used in deriving global characteristics of circumsolar radiation, was not available for the time spans for which ground based measurements were obtainable. Because the validation showed dissatisfactory results when processing the model output head on, the re-analysis dataset found no application in the end (see Sects. 4.2.1 & 5.1). Details concerning the model setup can be found in (Stein et al., 2011). The NRT data were obtained² in consolidated yearly files which contain successively the first 24 hours of each forecast run, starting at 0 UTC. The correspondent model experiment IDs under which the data can be obtained are *f93i* for the NRT and *fbov*, respectively, for the re-analysis.

3.3.2 Aerosol Optical Properties

This section describes the two different sets of aerosol optical properties which were employed in this study. The OPAC dataset (Optical Properties of Aerosols and Clouds) by Hess et al. (1998) which is included in the radiative transfer software package libRadtran was used for feasibility and sensitivity studies. Furthermore an optical property dataset was generated on the basis of the physical properties of the aerosol types as simulated in the ECMWF IFS (see Sect. 3.3.1). This dataset allows to derive circumsolar radiation from IFS output in the most consistent way. Where necessary, OPAC served to complement the information required for the generation of the optical property dataset, not provided by ECMWF.

²Data obtained from <http://macc.iek.fz-juelich.de/data/f93i/3hourly/ModelLevel/>. Data services provided by Forschungszentrum Jülich

The OPAC Dataset

OPAC defines so-called aerosol types (e.g. continental-polluted) which represent the external mixture of several aerosol components (e.g. soot or water soluble substances). The aerosol components discern themselves by their refractive index, density and particle size distribution. The latter is always parameterized as a logarithmic normal size distribution (e.g. Gasteiger, 2011, Eq. 2.28)

$$n(r) = \frac{dN}{dr} = \frac{N_0}{\sqrt{2\pi} \ln \sigma r} \exp \left[- \left(\frac{\ln r - \ln r_0}{\sqrt{2} \ln \sigma} \right)^2 \right] \quad (3.5)$$

where $n(r)$ is the particle number density per radius interval. The parameters of this distribution are the particle number density N_0 , the mode radius r_0 and the distribution width σ .

The OPAC optical properties were originally calculated for spheres using the Mie theory (Mie, 1908). libRadtran contains a modified version in which prolate spheroids represent mineral dust, instead of spheres. The aspect ratio distribution for the spheroids stems from microscopic observations made 2006 during the Saharan Mineral Dust Experiment (Kandler et al., 2011) and the optical properties were modeled as described in Wiegner et al. (2011), (Pers. comm. Joseph Gasteiger).

Optical Properties for ECMWF IFS Aerosol Components

Optical properties for the aerosol components, which are simulated in the ECMWF IFS, were created during this study for the use with libRadtran. Thereby it was tried to match their physical properties as closely as possible. The necessary parameters were taken from (Morcrette et al., 2009, and pers. comm. Jean-Jacques Morcrette, 2012). However, information concerning the refractive index could not be confirmed with certainty since the product is work in progress and not fully documented. The refractive indices used for the optical properties within the IFS model itself stem from the ADIENT³ project (pers. comm. Jean-Jacques Morcrette, 2012). However the corresponding project report (Highwood, 2009) does not always give unambiguous recommendations. In these cases reasonable assumptions were made.

³<http://www.reading.ac.uk/adient/ADIANT.html>

For the generation of the optical properties Josef Gasteiger (pers. comm. 2012) provided an extensive database of Mie calculations. An associated program allows to generate bulk optical properties according to given size distributions and spectral refractive indices.

Like in OPAC, the aerosol size distributions in the IFS are all based on the log-normal distribution (Eq. 3.5). The IFS aerosol types are either composed of a one-modal or a two-modal log-normal distribution. The latter is a superposition of two log-normal distributions. Furthermore for some aerosol types the distributions are subdivided into several size bins. The size distribution parameters for the different aerosol types are listed in Tab. 3.1. With these it is possible to calculate the volume distribution and the total aerosol volume. With the density ρ , the mass concentration ρ_V ($[\text{g}/\text{m}^3]$) can be derived. The mass concentration is the quantity which is accepted by libRadtran to scale the aerosol properties accordingly. The density values as well as the source of the used refractive indices for each aerosol type are listed in Tab. 3.2. In the following details concerning the individual types are given.

Dust

The size distribution is one-modal with $r_0 = 0.29 \mu\text{m}$, $\sigma = 2$ and $N_0 = 1 \text{ cm}^{-3}$. Since information on the refractive index could not be determined conclusively, the spectrally resolved refractive index from OPAC was used. Highwood (2009) discusses different possible data sources for refractive indices for dust, noting that OPAC shows relatively high absorption.

Sea Salt

Sea salt is hygroscopic, i.e. it takes up water dependent on the ambient relative humidity (RH). Correspondingly the aerosol grows. The size distribution is two-modal with [mode] radii (at 80% RH) of $0.1992 \mu\text{m}$ and $1.992 \mu\text{m}$, $\sigma = 1.9/2.0$ and $N_0 = 70 \text{ cm}^{-3}/3 \text{ cm}^{-3}$ (pers. comm. J.-J. Morcrette). The growth factor f_g is defined as

$$f_g = \frac{r_0(\text{RH})}{r_0(\text{RH} = 0\%)} \quad . \quad (3.6)$$

Growth factors used in OPAC and the IFS were compared. Figure 3.2 shows that they are similar. In the end the growth factors as well as the refractive index values from OPAC

were used. Highwood (2009) also recommends to use the values from Shettle and Fenn (1979), which are the basis for the OPAC implementation. With the utilized growth factors from OPAC the mode radii at $RH = 0\%$ evaluate to $0.1002\ \mu\text{m}$ and $1.002\ \mu\text{m}$, respectively. The density of the dry particles was taken from (Morcrette et al., 2009) as $2.16 \times 10^6\ \text{g}/\text{m}^3$ and was reduced according to the mass mixing ratios of salt and water for growing particles with the density of water being $1.0 \times 10^6\ \text{g}/\text{m}^3$.

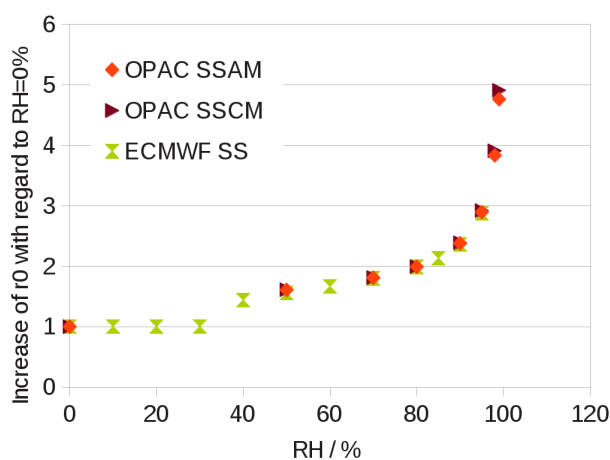


Figure 3.2: Hygroscopic growth factors for the sea salt (SS) accumulation mode (AM) and the coarse mode (CM) of OPAC, as well as for the Sea salt as implemented in the ECMWF IFS (pers. comm. J.-J. Morcrette).

Sulfate, Organic Carbon and Black Carbon

The three aerosol types organic carbon, black carbon and sulfate exhibit the same mode radius of $0.0355\ \mu\text{m}$ and have the same underlying size distribution with $\sigma = 2$ and $N_0 = 1\ \text{cm}^{-3}$ (pers. comm. J.-J. Morcrette). They only differ in the refractive index.

In the data description tables from the ECMWF homepage⁴ the organic component is named “organic matter”. From this name one could assume that this species includes gas-to-particle components as well brown carbon and pollen et cetera. A variety of optical properties is therefore thinkable. However, in personal communication J.-J. Morcrette referred to OC or organic carbon and mentioned that the source for the refractive indices

⁴<http://www.ecmwf.int/publications/manuals/d/gribapi/param/search=organic/> (last accessed 03/Jul/2013)

is the ADIENT database. Consequently, I used the refractive indices from ADIENT for organic carbon. Highwood (2009) describes organic carbon as “humic-like substances” that “generally derive from fossil fuel burning”. Since this includes many substances, the refractive indices may vary strongly. ADIENT uses the refractive index for Swanee River Fulvic Acid (SRFA), which is commonly used as proxy for organic carbon, as anchor point at 532 nm. From this reference value it employs a wavelength dependency which is collected from different studies, depending on wavelength interval. The ADIENT report states that the wavelength dependent refractive indices are given at the OPAC wavelengths. However, the wavelengths used by J. Gasteiger’s tools are slightly different to the ones in the files obtainable from the ADIENT homepage. Therefore, the refractive indices were interpolated linearly to the required wavelengths.

In the IFS the black carbon and the organic carbon component are both divided into a hydrophilic and hydrophobic part. For the hydrophilic part I used in principle the same refractive indices as for the hydrophobic part, but mixed with water. I.e. for the hydrophilic part the mode radius grows with RH and the refractive indices are mixed with the ones for water from the OPAC database⁵ according to the volume mixing ratio. Hygroscopic growth factors from the OPAC component *water-soluble (waso)* were used for technical reasons for organic carbon, black carbon and sulfate, which is always hygroscopic. Figure 3.3 compares them to the growth factors as used originally for the optical properties in the IFS. Alike the growth factors for sea salt they are similar.

The densities of dry organic and black carbon were both set to $1.769 \times 10^6 \text{ g/m}^3$ (pers. comm. J.-J. Morcrette). For sulphate the density of the OPAC component *waso* was used ($1.80 \times 10^6 \text{ g/m}^3$) due to lack of other information.

For sulfate as well as for black and organic carbon the size distribution was given by J.-J. Morcrette (pers. comm. 2012), however he did not state over what range the optical properties are integrated in the IFS. Hence, the integration was performed from $0.001 \mu\text{m}$ to $5 \mu\text{m}$ to include all possible particle sizes.

Discerning the different size bins and hygroscopic and hydrophilic parts, optical properties for 11 different aerosol components have been generated in total.

⁵Originally the refractive indices for water stem from Hale and Querry (1973).

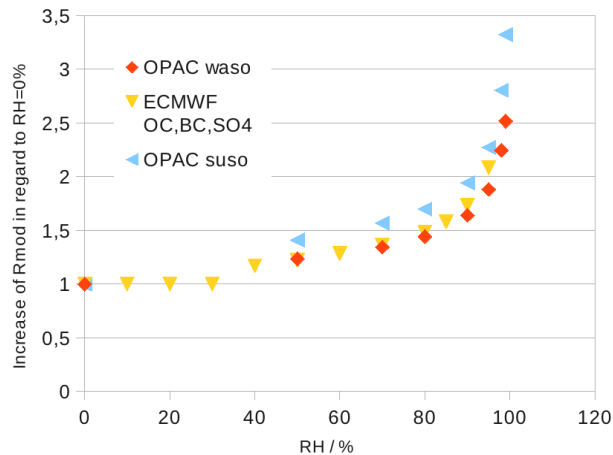


Figure 3.3: Hygroscopic growth factors for the OPAC components “water soluble” (waso) and “sulfate droplets” (suso), as well as for the for IFS aerosol types organic carbon (OC), black carbon (BC) and sulfate (SO4).

Table 3.1: Parameters of the size distributions underlying the aerosol optical properties generated for the use with IFS aerosol data. For multi-modal size distributions the values for r_0 , σ and N_0 are separated by a slash. All values are valid for $\text{RH} = 0\%$.

| Type | r_0 [μm] | σ | $N_0[\text{cm}^{-3}]$ | Size bin limits [μm] |
|--------------|-------------------------|-----------|-----------------------|-----------------------------------|
| Dust | 0.29 | 2 | 1 | 0.03 / 0.55 / 0.9 / 20 |
| Sea Salt | 0.1002 / 1.002 | 1.9 / 2.0 | 70 / 3 | 0.03 / 0.50 / 5 / 20 |
| Org. Carbon | 0.0355 | 2 | 1 | 0.001 / 5 |
| Black Carbon | 0.0355 | 2 | 1 | 0.001 / 5 |
| Sulfate | 0.0355 | 2 | 1 | 0.001 / 5 |

3.3.3 Post-Processing of ECMWF Output

The IFS provides the aerosol mass mixing ratio ζ ($[\text{kg kg}^{-1}]$) for each aerosol component for the individual model boxes. For the radiative transfer simulations in this study with libRadtran aerosol was always placed in a layer between 0 km and 1 km with a constant mass concentration ρ_V ($[\text{g m}^{-3}]$). Since for circumsolar radiation the integrated aerosol loading of the atmospheric column is of relevance, the area mass loading ρ_A ($[\text{g/m}^2]$) must be calculated as the common quantity. In case of the libRadtran calculations this is straightforward as $\rho_A = 1000 \text{ m} \cdot \rho_V$. For the IFS data the area mass loading is calculated as $\rho_A = \sum_{i=0}^N \zeta_i \cdot \rho_{A,\text{air},i}$ where N is the number of model layers and $\rho_{A,\text{air},i}$ the mass of air

Table 3.2: Density values ρ , as well as the sources of the refractive indices used in the generation of optical properties for the IFS aerosol types.

| Type | $\rho(\text{RH} = 0\%)$ | Refrac. Index Source |
|--------------|----------------------------------|-----------------------|
| Dust | $2.61 \times 10^6 \text{ g/m}^3$ | OPAC |
| Sea Salt | $2.16 \times 10^6 \text{ g/m}^3$ | OPAC |
| Org. Carbon | $1.77 \times 10^6 \text{ g/m}^3$ | interpol. from ADIENT |
| Black Carbon | $1.77 \times 10^6 \text{ g/m}^3$ | OPAC (soot) |
| Sulfate | $1.80 \times 10^6 \text{ g/m}^3$ | OPAC (waso) |

per m^2 in the layer $(i + 1)$. $\rho_{A,\text{air},i}$ is calculated from the pressure on the model levels i and $i + 1$ as $\rho_{A,\text{air},i} = (p_{i+1} - p_i)/g_0$ with the gravitational acceleration g_0 (assuming hydrostatic equilibrium). The pressure on the model levels can be reconstructed from the coefficients a_i and b_i , which are tabulated for every model level, and the surface pressure p_{surf} , which is given for every model column as $p_i = a_i \cdot 1 \times 10^5 \text{ Pa} + b_i \cdot p_{\text{surf}}$. \vec{a} , \vec{b} and p_{surf} are distributed along with the IFS model output.

The IFS output was available 3-hourly. While this seems appropriate to capture the aerosol concentration changes, the circumsolar radiation is also influenced by the sun zenith angle because it depends on the slant path optical thickness (Eq. 2.3). Therefore a 3-hourly resolution is not enough to capture its distinct daily course. Circumsolar radiation values were therefore calculated every 15 minutes with the aerosol properties being interpolated linearly from the 3-hourly values.

3.4 Atmospheric Radiative Transfer

3.4.1 The RTE-Solvers DISORT and MYSTIC

When it comes to simulating (unpolarized) radiances considering a horizontally homogeneous atmosphere, the application of the discrete ordinate method (e.g. in the implementation DISORT by Stamnes et al., 1988) is a common choice. It is thoroughly validated and freely available. However it has two drawbacks that complicate or sometimes even prohibit the correct simulation of circumsolar radiation. First, DISORT can only deal with a point source for the incoming radiation at top of atmosphere. For the correct calculation of radiances in the circumsolar region, the sun's extent has to be considered (see Sect. 2.5). This could also be achieved with DISORT by performing several simulations,

placing the point source at different spots within the sun disc, and weighting the results with the extraterrestrial radiance distribution, as suggested by Stamnes et al. (2000). This procedure, however, would strongly increase the computational time. One could also use just one simulation and fold the resulting sunshape with the extraterrestrial radiance distribution. This would take as given that the one radiative transfer simulation performed for a point source is representative of the whole sun disk – which would probably hold true for most (one dimensional) simulations required for this study. While the limitation of DISORT to a point source can therefore be considered merely as inconvenience, it is a real problem that it cannot reproduce the extreme forward peaks of some scattering phase functions: In the discrete ordinate method the radiative transfer equation is split into an even number n_{str} of independent integro-differential equations, called streams. The scattering phase function is expanded in a series of Legendre polynomials of equal length. Only a limited amount of Legendre polynomials/streams can be used, else the series expansion gets numerically unstable and the DISORT algorithm computationally inefficient (scales approximately with n_{str}^3 , Stamnes et al., 2000). With the limited amount of polynomials, the forward peaked phase functions of cirrus clouds cannot always be represented well. Buras et al. (2011) showed, as example, the Legendre series representation of the phase function of the “Baum v2” optical properties at $r_{\text{eff}} = 60 \mu\text{m}$ and $\lambda = 500 \text{ nm}$. Even with 20 000 Legendre polynomials – which for this case is about the maximum number before the series expansion gets instable – the deviations from the original phase function still reach a few percent. To alleviate these downsides, one normally uses a truncated Legendre series – corresponding to a less forward peaked phase function – but applies a so called “intensity correction” on the DISORT results (Buras et al., 2011). The intensity correction however, also shows instabilities for extremely forward peaked phase functions for certain setups (pers. com. Robert Buras, 2013). Furthermore DISORT does not cope well with some geometries. For example, with the sun in the zenith, the result must be extrapolated from the next zenithal supporting point, which depends on n_{str} . In situations with forward peaked phase functions this can lead to erroneous results, as shown further down in this section. Because of these deficiencies, DISORT was not used in this study to simulate radiances in the vicinity of the sun. However, the lookup tables for APICS, for which the forward peak of the scattering phase functions as well as the extent of the sun play no important role, have been computed with the C language version of DISORT from libRadtran, called CDISORT (Buras et al., 2011), using 16 streams.

MYSTIC (Emde and Mayer, 2007; Mayer, 2009; Emde et al., 2011; Buras and Mayer,

2011) – which stands for “Monte Carlo code for the physically correct tracing of photons in cloudy atmospheres” – is the Monte Carlo solver from the libRadtran radiative transfer package (Mayer and Kylling, 2005). Its principle to solve the radiative transfer is to trace individual photons through the atmosphere. All events in which the photon interacts with the atmosphere like scattering and absorption are treated statistically according to their physical probability density functions. Forward peaked scattering phase functions may also pose a problem for plain Monte Carlo simulations, as they may cause rare but result-dominating events – so called “spikes“. Leveling the spikes will increase computing time excessively. A solution for this problem was given by Buras and Mayer (2011). The variance reduction methods described by them are implemented in MYSTIC. It therefore brings along an important prerequisite to simulate the radiance distribution in the aureole region.

Figure 3.4 compares sunshapes simulated with DISORT and MYSTIC for a point source. It shows that both RTE solvers produce the same sunshapes for a setup with OPAC dust aerosols. Although the dust aerosol contains relatively large aerosol particles, the results agree, even for a low number of streams ($n_{\text{str}} = 16$). The relative difference compared to MYSTIC stays below 1% for any of the shown CDISORT simulations, and is therefore in the range of the Monte Carlo noise of the MYSTIC simulations. In the example with a cirrus cloud, it seems that CDISORT reproduces the MYSTIC sunshape well for θ approximately larger than 0.25° but differences occur closer to the source. However, from Fig 3.5, which shows the relative deviation of the CDISORT results from the MYSTIC results, it becomes obvious that errors in the magnitude of 20% and even more must be expected in the circumsolar region. This emphasizes the just discussed drawbacks of DISORT concerning strongly forward peaked phase functions.

3.4.2 Adaptation of the RTE-Solver MYSTIC

“Backward” Simulation of Aureole Irradiance

The most obvious way to simulate radiance with a Monte Carlo model is to inject photons at top of the atmosphere and trace them until they are absorbed, back-scattered into space or eventually reach a detector surface through a finite cone where they are counted. The probability for photons to enter the detector cone however is vanishingly small. Therefore most simulated photons will be absorbed or leave the system before reaching the detector

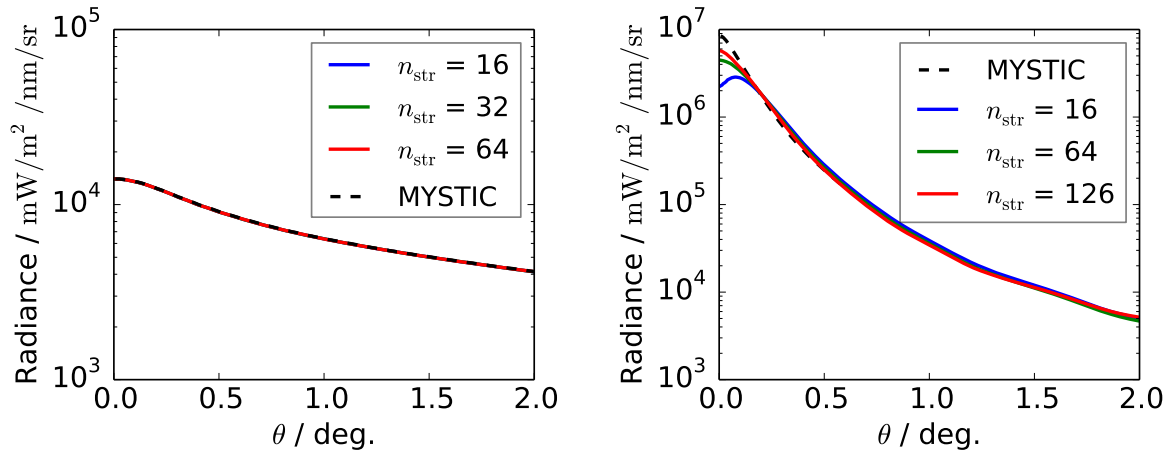


Figure 3.4: Simulations of sunshapes with libRadtran’s solver CDISORT using different numbers of streams compared to a simulation with the MYSTIC solver for desert dust aerosol from OPAC (left panel) and a cirrus cloud composed of HEY solid columns (right panel). $\theta_{\text{sun}} = 0^\circ$. See Fig. 3.5 for relative deviations between CDISORT and MYSTIC.

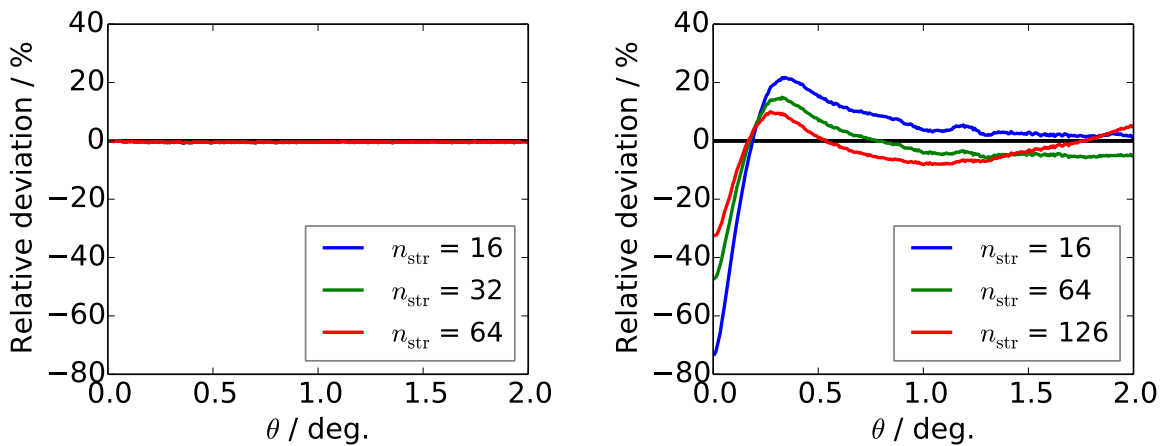


Figure 3.5: Relative deviation of the sunshapes simulated with CDISORT to the simulation with the MYSTIC solver as in Fig. 3.4.

and thus will not contribute to the result. Simulations therefore converge extremely slow with this method. If the considered radiative transfer problem is one dimensional, that is, if no horizontal variation of the atmosphere is allowed, the results are horizontally invariant. The lateral position of the detector is therefore irrelevant and only its directional orientation matters. Or in other words, one can shorten the simulation time by introducing new detectors at suitable positions. By performing so called “local estimates” (LEs) the convergence of the results can be sped up even more. In this case a LE is executed at every scattering event. That is, the probability is calculated that the photon would be scattered directly into a detector of the considered directional orientation and reach this detector without any further scattering or being absorbed. Therefore every scattering photon contributes to the result. Figure 3.6 illustrates this approach which enhances the convergence of the simulation considerably.

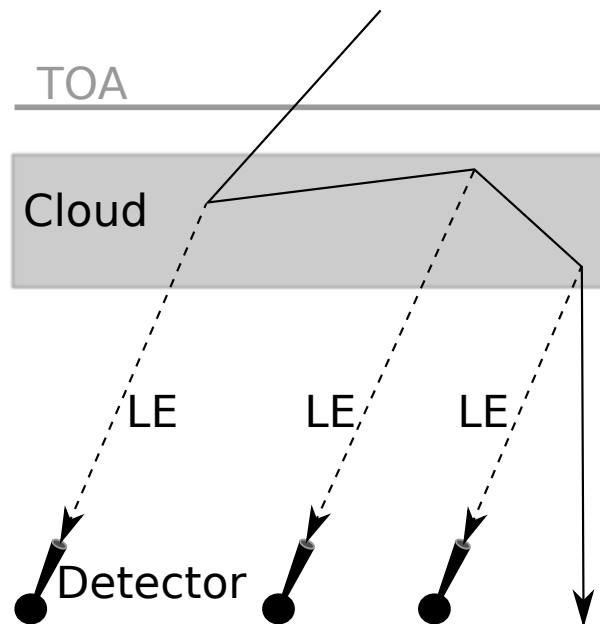


Figure 3.6: Scheme of a forward Monte Carlo calculation of radiance for a one-dimensional radiative transfer problem utilizing local estimates (LEs, dashed lines). Photons are injected at top of atmosphere (TOA). A local estimate is executed at every scattering event along the photon path (solid line).

If a three dimensional radiative transfer problem has to be solved, the orientation *and* position of the detector must be considered. Tracing photons forward is therefore not efficient because performing local estimates is not possible anymore. In this case radiances are usually calculated backward. Thereby the reciprocity principle is used. Photons are

started from the detector in the direction for which the radiance shall be calculated. The photons are then traced backward through the atmosphere. Again a local estimate is executed at every scattering event. However, instead of the probability for the photons being scattered into the direction of the detector, the probability for a scattering into the direction of the sun is calculated (see also illustration in Fig. 3.8 further down). This is called the “backward” Monte Carlo method. For this study only 1D-radiative transfer capabilities are necessary, for which the forward method could have been used. In the end however, MYSTIC’s backward code was adapted for the accurate simulation of circumsolar radiation. Such, circumsolar radiation can also be simulated for 3D-scenes, in case future applications require so.

Considering the calculation of the CSR the integrated value of the radiance over a solid angle section around the sun is desired. Therefore, I modified the backward method such that the photons are not only emitted into one single direction but evenly distributed over the solid angle covered by the detector. The goal is to compute a mean radiance that only needs to be multiplied by the solid angle to obtain the corresponding irradiance. Note that by doing so, the cosine term in the integral $\iint L(\alpha, \phi) \cos(\alpha) \sin(\alpha) \, d\alpha d\phi$ is safely neglected (comp. Sect. 2.6).

Despite the variance reduction methods by Buras and Mayer (2011), the backward simulation of mean radiance for a detector with an extended field of view which may suffer from an unbalanced contribution of the individual photons. This happens if the field of view is centered at the sun and a strongly forward-peaked scattering phase function is present. In this case the photons emitted close to the edge of the detector’s field of view will contribute considerably less to the result than the ones emitted near the center. This is because during the first local estimate the outer photons will have a much smaller probability of being scattered into the direction of the sun than the inner photons: The inner photons need to be scattered by a smaller angle than the outer ones. Due to the strong gradient in the forward peak of the scattering phase function even small differences in scattering angle will lead to large differences in scattering probability. Therefore, on average, the local estimates for the inner photons will be quite high compared to the ones for the outer photons, and so will be the contribution to the result. This will slow down the convergence of the result. To overcome this, I modified the initial distribution of photon directions in MYSTIC, so that more photons are launched near the center of the field of view than geometrically justified. This change of sampling strategy must be corrected for by weighting the photon contributions to the result accordingly. In the end more photons are launched closely to

the sun with lower photon weights and less photons are launched in the outer areas of the aureole but with increased photon weights which leads to a more balanced contribution of the individual photons to the result and thus to a faster convergence.

In principle the Monte Carlo method allows an arbitrary sampling strategy as long as it is accounted for by appropriate photon weights. To initially distribute the photon directions, I adhered to the function P_{ddis} , which is dynamically generated within MYSTIC from the scattering phase functions utilized in the simulation. It has already proved useful in the other variance reduction methods implemented in MYSTIC. P_{ddis} is defined as (Buras and Mayer, 2011, Eq. 10),

$$P_{\text{ddis}}(\theta) = c_{\text{ddis}} \max_i [P_i(\theta)] \text{ for all } \theta \in [0^\circ, 180^\circ] \quad . \quad (3.7)$$

It is the maximum of all scattering phase functions P_i in the current simulation (e.g. for different cloud or aerosol types present in the scene). That is, for every scattering angle θ the maximum value of all scattering phase functions is taken. The resulting function is then normalized with the coefficient c_{ddis} . The initial photon directions are distributed according to this function which is evaluated in the angular interval covered by the field of view of the considered detector. Technically this is realized by first directing every photon towards the sun center and then “scattering” the photon – still at the original position – according to the virtual scattering phase function P_{ddis} . Thereby only scattering angles are allowed which are in line with the desired detector geometry. This is achieved by cutting of P_{ddis} at the angular radius of the detector’s field of view and re-normalizing it afterwards, so that the total scattering probability remains unity. Figure 3.7 illustrates how this approach balances the contributions of the individual photons: In the left panel the initial directions are evenly distributed over the field of view, but most photons contribute only negligibly to the result. In the right panel the photons are distributed according to P_{ddis} and weighted accordingly. In this case the photon contribution is much better balanced. Note that both simulations converge to the same result, but the simulation relying on P_{ddis} for the photon distribution reaches a better uncertainty level. Expressed as standard deviation it is a factor seven lower than for the simulation relying on the original photon distribution.

Extraterrestrial Radiance Distribution

To simplify the radiative transfer the sun is commonly assumed to be a point source at infinity. All sun rays are therefore parallel and enter the atmosphere under the same angle.

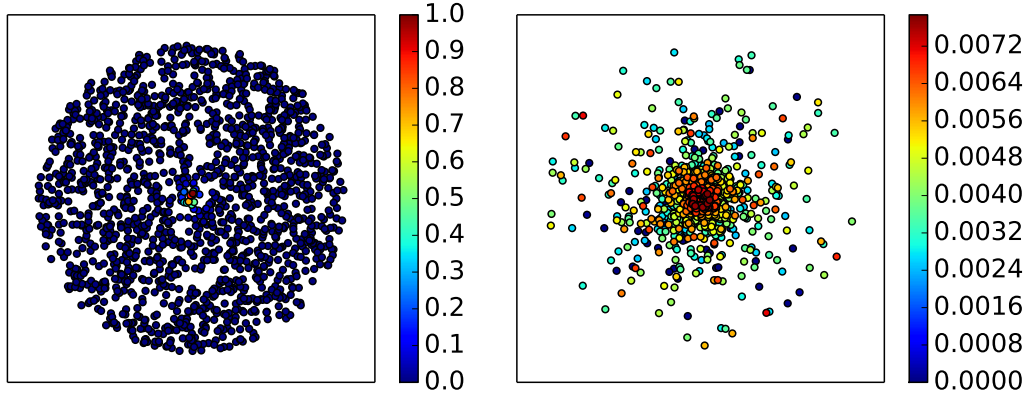


Figure 3.7: Initial distribution of photon directions for MYSTIC simulations of a detector with 2.5° aperture and a scene with a cirrus composed of HEY aggregates ($r_{\text{eff}} = 30 \mu\text{m}$, $\tau = 1.0$). The contribution to the result (in arbitrary units) from the first local estimate is color-coded. In the left panel the photons are distributed evenly with solid angle. In the right panel the photons are distributed according to P_{dis} (Eq. 3.7) and their contribution is weighted accordingly to this modified distribution. Note the different color scales.

However this approximation is not appropriate when simulating radiance in the vicinity of the sun disk. The sun has a finite angular extent and the center of the sun disk is brighter than the limb. This so called limb darkening is caused by absorption in the sun's atmosphere and is therefore wavelength dependent. To take account of these effects I implemented a disk source in MYSTIC which uses a wavelength dependent limb darkening model. The radiance distribution L_λ relative to the radiance from the center of the sun $L_{0,\lambda}$ is given in (Scheffler and Elsässer, 1990) and (Köpke et al., 2001) as

$$\frac{L_\lambda}{L_{0,\lambda}} = \frac{1 + \beta_\lambda \cos \theta}{1 + \beta_\lambda} = \frac{1 + \beta_\lambda \sqrt{1 - r^2}}{1 + \beta_\lambda} . \quad (3.8)$$

Here θ denotes the exit angle of the radiance normal to the surface of the sun. For our purpose the second formulation is more practical where $r = 0$ represents the center of the sun disk and $r = 1$ the limb; simple geometric considerations on the unit circle confirm that $\sqrt{1 - r^2} = \cos \theta$. The limb darkening coefficient β_λ depends on the wavelength; I adopted the corresponding formula from Köpke et al. (2001) (originally from Waldmeier, 1941):

$$\beta_\lambda = \frac{3hc\sqrt{2}}{8k\lambda T_s} \quad (3.9)$$

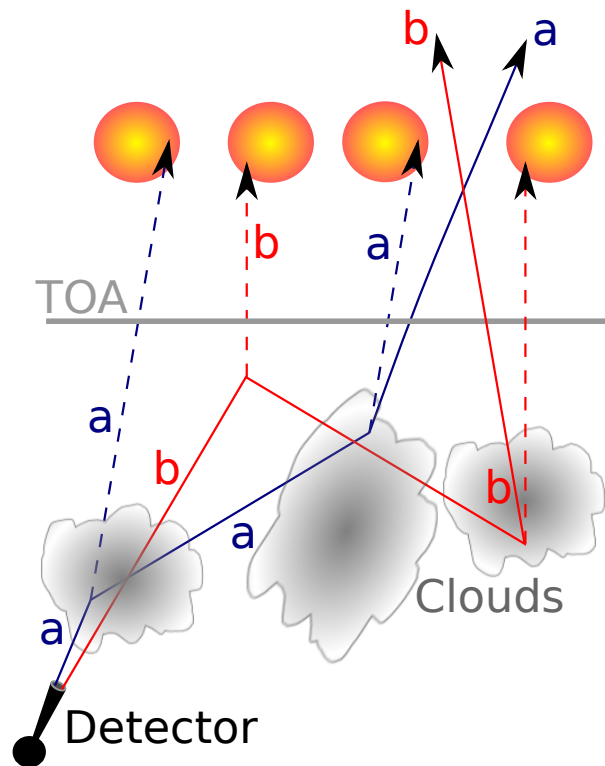


Figure 3.8: Illustration of the “backward” Monte Carlo method for the simulation of radiance. Photons are started from the detector and traced until they are absorbed or leave the atmosphere. Two photon paths (solid lines) are depicted (a & b). The initial photon directions are distributed within the detector cone. At each scattering event a local estimate (dashed lines) is performed which contributes to the result. A local estimate direction on the sun disk is randomly assigned to each photon with a probability according to the limb darkening (Eq. 3.10). This LE-direction is fixed throughout the photon journey.

where λ is the wavelength in m, h the *Planck* constant (6.6261×10^{-34} J s), c the speed of light (2.9979×10^8 m s $^{-1}$), k the *Boltzmann* constant (1.3806×10^{-23} J K $^{-1}$) and T_s the temperature of the sun's surface (5740 K).

A disk source is used in the simulation of the diffuse as well as of the direct radiation. Since photons are traced backward, the disk source has to be considered in the local estimate direction. Each photon gets randomly assigned one direction, into which all LEs are performed. The LE directions are sampled on the sun disk according to the limb darkening function. That is the probability density p for a photon having assigned a LE direction pointing to a spot on the sun disk with angular distance α from center is given as

$$p = \begin{cases} \frac{L_\lambda(\frac{\alpha}{\alpha_{\text{sun}}}) \sin \alpha}{\int_{0^\circ}^{\alpha_{\text{sun}}} L_\lambda(\frac{\alpha}{\alpha_{\text{sun}}}) \sin \alpha \, d\alpha} & \text{for } \alpha \leq \alpha_{\text{sun}} \\ 0 & \text{else} \end{cases} \quad (3.10)$$

The sine term accounts for the changing solid angles covered by annular sections of constant $d\alpha$ as α changes. Figure 3.8 illustrates the backward tracing of photons with a sun disk as source.

In case direct radiation is to be included in the simulation, it is checked directly after the generation of each photon whether the randomly assigned local estimate direction is covered by the sensor's field of view. If so, the probability of the photon reaching the sun without scattering or absorption is calculated in analogy to a LE to obtain the contribution of the direct radiation to the result. This is performed even before the photon starts to move. Only then the photon is launched on its journey through the atmosphere.

The angular sun radius α_{sun} can be set manually or be determined automatically if a time and date is given. The simulations performed for this study, however, neglect the course of the year of α_{sun} and refer to a mean angular sun radius of 0.266° . From reference simulations with varying α_{sun} it is estimated that the absolute error in CSR that arises from this is less than ± 0.004 as long as $\alpha_{\text{cir}} > 0.375^\circ$. However, as Neumann et al. (2002) have demonstrated, the actual sun radius should be taken into account when calculating CSR from ground based sunshape measurements.

The just discussed model improvements can be followed in Fig. 3.9. The differences between a simulation of the diffuse radiance with a point source (blue) and a disk source (green) are pronounced for angles smaller than $\approx 1^\circ$ from the sun center which is in line with findings by Grassl (1971). The red curve shows the total sunshape consisting of direct and diffuse

radiation.

Figures 3.10 and 3.11 demonstrate the capabilities of MYSTIC to simulate the radiative transfer for a 3D scene. They are intended to give the reader an idea of how the circumsolar radiation caused by cirrus clouds and aerosols appear to the human eye. The simulations were performed with the option “output RGB”. This prompts MYSTIC to calculate radiances at several wavelengths between 380 nm and 780 nm and to weight these results into values for red, green and blue color similar to the perception of the human eye. For the simulations concerning aerosol (Fig. 3.11) some cumulus clouds were introduced to the scene to provide more contrast. The corresponding 3D cloud field was produced by Katrin Wapler performing a large eddy simulation (LES). For detail on the LES refer to Wapler (2007).

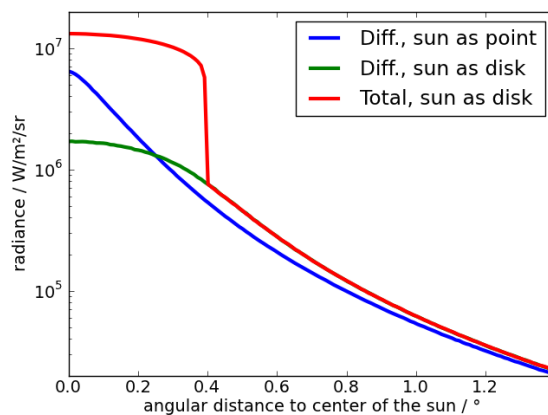


Figure 3.9: Simulated broad band sunshape for a cirrus cloud with optical thickness 0.5 and with the sun in the zenith. Blue: Diffuse radiance for a point source. Green: Diffuse radiance for a disk source. Red: Direct and diffuse radiance for a disk source.

3.4.3 Pseudo-Spectral and Solar Integrated Radiative Transfer

As mentioned, the RTE (Eq. 2.4) must be solved for each wavelength individually. If RT simulation results are given at a certain wavelength in this study, they were obtained by a pseudo-spectral calculation treating the molecular absorption with the band parameterization from LOWTRAN as implemented in libRadtran (adapted from Ricchiazzi et al., 1998). Where the results are “broad band” (bb) or solar/shortwave integrated, they have been obtained using the kato2 correlated-k distribution as provided by libRadtran. kato2

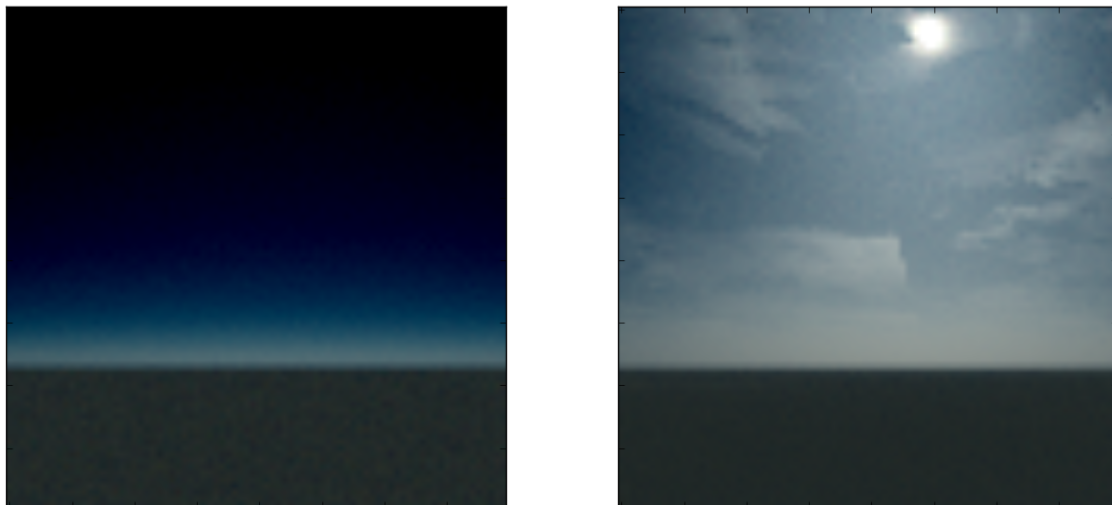


Figure 3.10: MYSTIC RGB simulations of the diffuse radiation, Albedo = 0.2, $\theta_{\text{sun}} = 49^\circ$, Viewing elevation: -17.5° till $+44.4^\circ$. Azimuthal field of view: 80° , Left: Pure Rayleigh atmosphere. Right: Inhomogeneous cirrus layer with a maximum optical thickness of ≈ 0.35 .

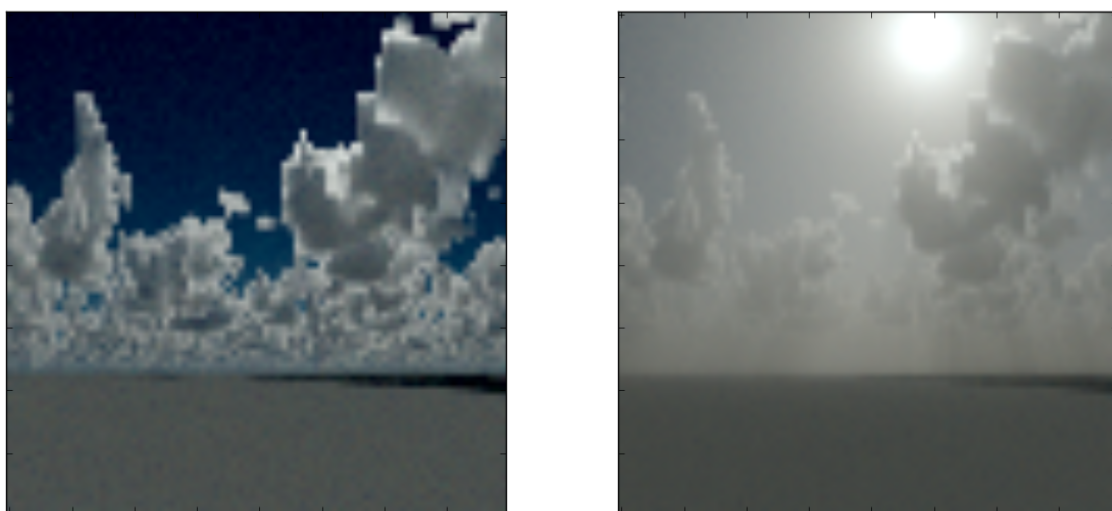


Figure 3.11: MYSTIC RGB simulations of the diffuse radiation, Albedo = 0.2, $\theta_{\text{sun}} = 49^\circ$, Viewing elevation: -17.5° till $+44.4^\circ$. Azimuthal field of view: 80° , Left: Rayleigh atmosphere with fair weather cumuli. Right: Additionally with a layer of aerosol (OPAC desert dust, aerosol optical depth 0.5). Cumulus clouds by K. Wapler.

is an update of the version described by Kato et al. (1999). It uses optimized tables provided by Seiji Kato which allow to reach similar precision with a reduced number of 148 sub-bands instead of 575, which corresponds to a reduced number of RTE-solver calls.⁶

3.5 Parametrization of Circumsolar Radiation

The Monte Carlo radiative transfer solver MYSTIC was adapted during this study such that it can simulate the radiance distribution in the circumsolar region with high accuracy (Sect. 3.4.2). However, these simulations are computationally too expensive to perform them by the number of millions needed to evaluate the satellite or weather model data used in this study. Therefore in this section a way of efficiently parameterizing the circumsolar radiation – and especially the CSR – is developed. A table of coefficients obtained from MYSTIC simulations together with the concept of an apparent optical thickness by Shiobara and Asano (1994) acts as a basis for this. Parts of this section are adapted from Reinhardt et al. (2013).

As mentioned, the circumsolar radiation relevant for CST applications is mainly caused by forward scattering within aerosol or thin cirrus layers. When parameterizing circumsolar radiation it is sufficient to focus on the properties of the atmospheric layers containing scattering particulates. Therefore, varying Rayleigh scattering due to changing sun zenith angle θ_{sun} or different elevations as well as surface albedo changes are neglected in the following. The effects of these simplifications were analysed by several simulations for the largest and therefore most sensitive field of view considered in this study, $\alpha_{\text{cir}} = 5^\circ$. The control simulations show that Rayleigh scattering in a pure atmosphere causes a shortwave integrated circumsolar irradiance of less than 1 W/m^2 and a CSR of less than 0.0015 even for the extreme assumption of the surface albedo being 1. This was tested for varying sun zenith angles θ_{sun} between 0° and 88° . To assess the effect of a changing surface albedo, it was varied between 0 and 1 considering different ice clouds ($0 < \tau < 3$). Resulting changes in diffuse shortwave integrated irradiance were always below 2 W/m^2 or 0.0025 in CSR respectively. Therefore, unless stated otherwise, the simulations used for the development of the circumsolar radiation parameterization were performed with $\theta_{\text{sun}} = 0^\circ$, albedo 0 and elevation 0 m.⁷

⁶See also the libRadtran user manual.

⁷For aerosol a θ_{sun} dependence for high sun zenith angles was diagnosed and accounted for (Sect. 3.5.3).

The calculation of circumsolar radiation in this study is limited to sun zenith angles smaller than 80° . For larger sun zenith angles the plane parallel assumption introduces considerable errors. Furthermore also the cloud property retrieval is not reliable for $\theta_{\text{sun}} > 80^\circ$ (Sect. 3.2). However this limitation is of little importance as many CST facilities are inoperative at such low solar altitude due to the rapid decrease of direct irradiance for larger sun zenith angles and due to the increased self shadowing.

3.5.1 Concept of the Apparent Optical Thickness

Shiobara and Asano (1994) and Kinne et al. (1997) corrected sun photometer measurements in case of cirrus clouds with the concept of an apparent optical thickness. Recently Segal-Rosenheimer et al. (2013) developed this approach further into a cloud property retrieval for sun photometer data. In the following the concept of an apparent optical thickness serves to parameterize circumsolar radiation. We shall see that this approach enables to calculate circumsolar radiation elegantly and in a flexible way from a comparatively low number of pre-calculated coefficients. The concept allows to eliminate the optical thickness of the scattering layer as degree of freedom. Furthermore, circumsolar radiation in the presence of several different scattering layers can easily be calculated because the apparent optical thickness can be assumed to be additive without making a large error. In the following the concept is outlined.

The direct transmission T through the atmosphere can be decomposed into a particulate and molecular transmission

$$T = T_p T_m \quad (3.11)$$

The particulate transmission T_p is expressed as

$$T_p = \exp(-\tau_s) \quad (3.12)$$

where τ_s is the particulate slant path optical thickness along the line of sight from the observer to the sun. The molecular transmission T_m is determined by Rayleigh scattering and absorption by air molecules.

Diffuse radiation – that is radiation having been scattered in the atmosphere – will enter any optics with a finite field of view pointed towards the sun in addition to the direct

radiation. The direct radiation has not been scattered and therefore stems only from the sun while diffuse radiation can come from both – the sun disk region and the circumsolar region.

Considering the total radiation entering the field of view one may consider an apparent transmission T' which describes both, the diffuse and the direct contribution. T' can as well be decomposed into a particulate and molecular part.

$$T' = T'_p T'_m \quad (3.13)$$

Since Rayleigh scattering on molecules contributes only a negligible part to the radiation in the circumsolar region, one can approximate $T'_m = T_m$. The molecular transmission T_m will not be further discussed here since it will cancel out later in the relevant formulas.

The apparent particulate transmission T'_p can be parameterized as

$$T'_p = \exp(-k\tau_s) \quad , \quad (3.14)$$

with k taking values between 0 and 1. This means that the difference between the direct particulate transmission – following Beer's law – and the apparent particulate transmission can be accounted for with the factor k . Defining the apparent optical thickness τ_{app} one obtains

$$\tau_{\text{app}} = k\tau_s \quad , \quad (3.15)$$

$$T'_p = \exp(-\tau_{\text{app}}). \quad (3.16)$$

It is notable that the corrective factor k depends mainly on the field of view, r_{eff} and the ice particle shape or the aerosol type but is almost independent of τ_s itself. This holds true as long as the optical thickness does not get too large. Extensive Monte Carlo simulations performed during this study with different ice particle types as well as with different aerosol species showed that as long as $0 < \tau_s < 3$, k varies by less than 3% if all other parameters except the optical thickness are kept constant.

A lookup table approach allows the fast computation of CSR using a parameterization instead of solving the radiative transfer equation. Thereby k is interpolated linearly between pre-tabulated values obtained from MYSTIC simulations. The corresponding ansatz is outlined in the following.

If we denote the circumsolar irradiance entering an aperture with an opening angle α as I_{cir} , the total irradiance entering the same aperture as $I_{\text{tot},\alpha}$ and the total irradiance coming solely from the sun disk as $I_{\text{tot},\text{sun}}$, then we can write the circumsolar ratio as

$$\begin{aligned} \text{CSR} &= \frac{I_{\text{cir}}}{I_{\text{tot},\text{sun}} + I_{\text{cir}}} = \frac{I_{\text{tot},\text{sun}} + I_{\text{cir}} - I_{\text{tot},\text{sun}}}{I_{\text{tot},\text{sun}} + I_{\text{cir}}} \\ &= 1 - \frac{I_{\text{tot},\text{sun}}}{I_{\text{cir}} + I_{\text{tot},\text{sun}}} = 1 - \frac{I_{\text{tot},\text{sun}}}{I_{\text{tot},\alpha}}. \end{aligned} \quad (3.17)$$

In general we can express the total irradiance $I_{\text{tot},\text{sun}}$ and $I_{\text{tot},\alpha}$ for a given atmosphere by

$$I_{\text{tot},\text{sun}} = I_0 T'_{\text{p},\text{sun}} = I_0 \exp(-k_{\text{sun}}\tau_s) \quad (3.18)$$

$$I_{\text{tot},\alpha} = I_0 T'_{\text{p},\alpha} = I_0 \exp(-k_{\alpha}\tau_s) \quad (3.19)$$

with k_{sun} being the corrective factor for a field of view correspondent to the sun's angular radius and k_{α} for a field of view correspondent to the limiting angle for which the CSR shall be calculated. I_0 denotes the solar constant I_s corrected for molecular transmission:

$$I_0 = I_s T_m. \quad (3.20)$$

Applying Eqs. (3.18) & (3.19) to Eq. (3.17) yields

$$\text{CSR} = 1 - \frac{\exp(-k_{\text{sun}}\tau_s)}{\exp(-k_{\alpha}\tau_s)} = 1 - \exp[-(k_{\text{sun}} - k_{\alpha})\tau_s]. \quad (3.21)$$

One should note that k_{sun} and k_{α} are subtracted which can lead to an adding of the individual errors. Therefore, the error in CSR due to tabulating them independently of the optical thickness can reach up to 20%, but most times it is well below 10%. If higher precision is required, k can be tabulated at several supporting points in τ .

Since the angular radius of the sun is assumed constant, we can re-write Eq. (3.21) as

$$\text{CSR} = 1 - \exp(-\Delta k_{\alpha}\tau_s) \quad (3.22)$$

with $\Delta k_{\alpha} = k_{\text{sun}} - k_{\alpha}$. One can even simplify further:

$$\text{CSR} \approx \Delta k_{\alpha}\tau_s \quad (3.23)$$

as long as $\Delta k_\alpha \tau_s$ is much smaller than 1. This is often the case for aerosol for which, in contrast to cirrus clouds, both Δk_α as well as τ_s are often small. Figure 3.12 compares the exponential ansatz and the linear approximation exemplary for one type of cirrus cloud and one type of aerosol. For the considered aerosol type the linear approximation can be used even for high values of τ_s without making a large error. For cirrus clouds, however, considerable errors arise for $\tau_s \gtrsim 0.5$.

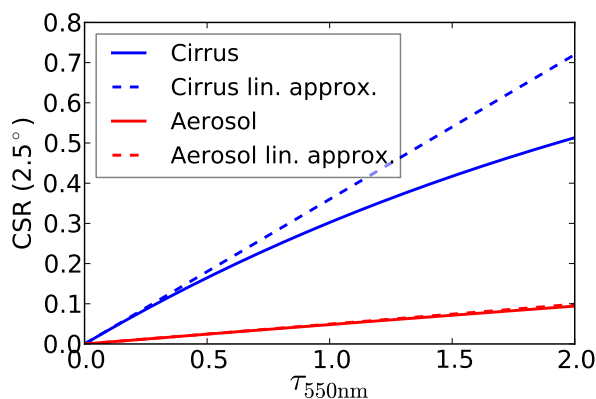


Figure 3.12: CSR for a cirrus cloud (Baum v2.0, $r_{\text{eff}} = 25 \mu\text{m}$) and for aerosol (OPAC mineral dust accumulation mode) calculated once with the precise exponential ansatz (Eq. 3.22, solid lines) and once with the linear approximation (Eq. 3.23, dashed lines).

For cirrus clouds I tabulated broad band values of the corrective factor k as a function of three parameters: The field of view which is characterized by the aperture's opening half angle⁸ α , the particle shape and the particle size⁹ r_{eff} , Please note that APICS returns the cirrus optical thickness at 550 nm, however for this study the integrated solar broad band (bb) circumsolar radiation is in the focus. Therefore, the conversion from optical thickness at 550 nm to the integrated solar value is also incorporated into k . Hence the tabulated values of k discussed in the following will translate a slant path optical thickness at 550 nm into a broad band *apparent* optical thickness. The broad band optical thickness of cirrus clouds does in general not differ much from the optical thickness at 550 nm. However, because this small conversion factor is included, k can at times be slightly larger than 1.

⁸supporting points 0.266° , 0.375° , 0.5° , 0.75° , 1.0° , 1.5° , 2.0° , 2.5° , 3.0° , 4.0° and 5.0°

⁹supporting points $5 \mu\text{m}$, $10 \mu\text{m}$, $15 \mu\text{m}$, $20 \mu\text{m}$, $25 \mu\text{m}$, $30 \mu\text{m}$, $40 \mu\text{m}$, $50 \mu\text{m}$, $60 \mu\text{m}$, $70 \mu\text{m}$, $80 \mu\text{m}$ and $90 \mu\text{m}$, as far as covered by the optical properties.

Table 3.3: Exemplary values of k (Eq. 3.14) for varying ice optical properties.

| Optical Properties | $k(0.266^\circ)$ | $k(2.5^\circ)$ | $k(5.0^\circ)$ |
|--|------------------|----------------|----------------|
| Baum v2.0, $r_{\text{eff}} = 10 \mu\text{m}$ | 0.97 | 0.65 | 0.55 |
| Baum v2.0, $r_{\text{eff}} = 25 \mu\text{m}$ | 0.82 | 0.46 | 0.43 |
| Baum v2.0, $r_{\text{eff}} = 60 \mu\text{m}$ | 0.52 | 0.33 | 0.32 |
| Baum v3.5, $r_{\text{eff}} = 10 \mu\text{m}$ | 0.96 | 0.60 | 0.53 |
| Baum v3.5, $r_{\text{eff}} = 25 \mu\text{m}$ | 0.80 | 0.52 | 0.49 |
| Baum v3.5, $r_{\text{eff}} = 60 \mu\text{m}$ | 0.65 | 0.50 | 0.47 |

To obtain k , the irradiance I_{tot} within the considered field of view was simulated with MYSTIC for clouds with an optical thickness at 550 nm of 1.5. k is then calculated as

$$k = \frac{\log\left(\frac{I_0}{I_{\text{tot}}}\right)}{1.5} . \quad (3.24)$$

I_0 is obtained by a MYSTIC simulation of the irradiance within a 0.266° field of view for a cloud- and aerosol-free atmosphere. An exemplary excerpt of the lookup table for cirrus clouds is given in Tab. 3.3.

For aerosols the parameters aerosol type/component, field of view and relative humidity¹⁰ were considered as variables in the tabulation of k . The ECMWF IFS primarily delivers (dry) aerosol mass mixing ratios which are converted into area mass loadings. Therefore k was tabulated in a different way for aerosol than for clouds; for aerosol k converts from area mass loading directly to apparent optical thickness:

$$\tau_{\text{app}} = k_{\text{aerosol}} \frac{\rho_A}{\mu} . \quad (3.25)$$

It should be noted that the outlined concept can serve in the derivation of other circumsolar radiation parameters besides CSR as well. The diffuse irradiance in the circumsolar region $I_{\text{cir}} = I_{\text{tot},\alpha} - I_{\text{tot},\text{sun}}$ for example is the relevant parameter when considering solar resource overestimation by pyrhelimeters. Since $I_{\text{tot},\alpha}$ is basically the integral of the sunshape L (comp. denominator in Eq. (2.13)) over the solid angle, one can also obtain the mean value

¹⁰supporting points 0 %, 50 %, 70 %, 80 %, 90 %, 95 %, 98 % and 99 %

of the sunshape \bar{L} between the limiting angles α_1 and α_2 by numerical differentiation of $I_{\text{tot},\alpha}$ with respect to the solid angle Ω enclosed by the corresponding field of view as

$$\bar{L}(\alpha_1 < \alpha < \alpha_2) = \frac{I_{\text{tot},\alpha_2} - I_{\text{tot},\alpha_1}}{\Omega(\alpha_2) - \Omega(\alpha_1)}. \quad (3.26)$$

This way the sunshape can be coarsely reproduced from the k -LUT, although this may be not the most straightforward way of use. An example for this is shown in Fig. 3.13. The leaps in the reconstructed sunshape occur at angular supporting points of the k lookup table, in between them k is interpolated linearly.

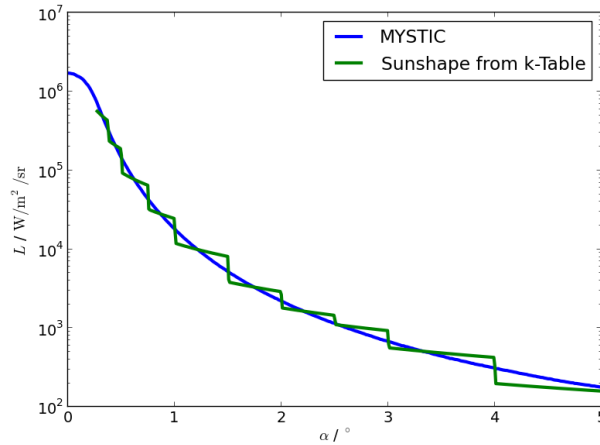


Figure 3.13: Broad band (300 nm – 2600 nm) sunshapes for a cirrus with $\tau_s = 0.5$, $r_{\text{eff}} = 40 \mu\text{m}$ (HEY solid-columns). Blue: From a MYSTIC simulation. Green: Calculated according to Eq. (3.26) from the lookup table for k .

For all applications of the k -LUT for which I_0 does not cancel out (e.g. calculation of I_{cir}) and is required as function of the sun zenith angle, I_0 was interpolated linearly from simulations of 1° resolution in θ_{sun} .

Figure 3.14 summarizes the basic concept of the outlined parameterization in a flowchart.

3.5.2 Treatment of Multiple Scattering Layers – The Adding Method

So far the developed parameterization allows to calculate circumsolar radiation caused by a single layer of scattering particles only. However at times more than one layer has to be

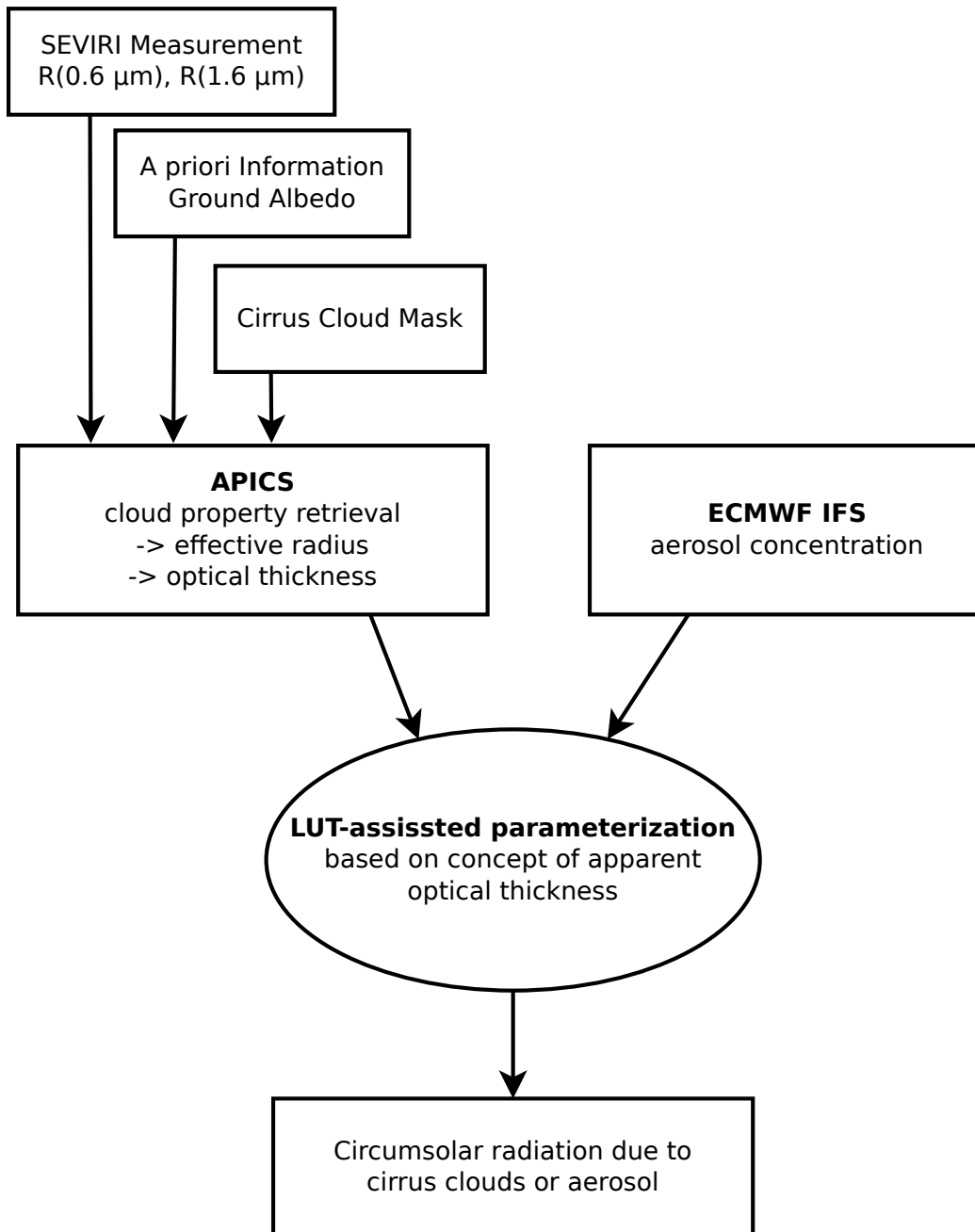


Figure 3.14: Flowchart of the developed method to derive circumsolar radiation.

dealt with; be it in the case of a cirrus above an aerosol layer or when an external mixture¹¹ of aerosols is to be considered, which can be regarded as multiple individual layers as well. The latter is the case if IFS data is to be evaluated, because the model output is an external mixture of aerosol components. The optical thickness of several scattering layers is additive, and since the parameterization is based on the *apparent* optical thickness, it was obvious to test whether it is additive as well.

For this two different test scenarios were considered. The first one places cirrus clouds over aerosol layers, the second one deals with external aerosol mixtures. In both cases reference simulations were performed with MYSTIC, treating the multiple layers explicitly. The sum of the parameterized values of apparent optical thickness for the individual layers computed according to Eq. 3.15 were then compared to these simulations. The summation of τ_{app} values of individual layers or components is called “adding method” in the following. The tests shown in the following were performed for a field of view of 3.0° . The standard deviation in $\tau_{\text{app,bb}}$ derived from the MYSTIC reference simulations due to Monte Carlo noise is always smaller than 0.8%.

The cirrus clouds in the first test scenario were always composed of HEY solid-columns. The ice optical thickness at 550 nm was varied between the three values of 0.1, 0.5 and 1.2 and the effective radius was set to 5 μm , 10 μm , 20 μm , 30 μm , 40 μm , 50 μm , 70 μm or 90 μm . For the aerosol layer optical properties for the three different size bins of the IFS dust aerosol were variantly used at aerosol optical thickness values at 550 nm of 0.1, 0.3 and 1.2. In total $3 \cdot 8 \cdot 3 \cdot 3 = 216$ scenes were created. Figure 3.15 compares the resulting broad band apparent optical thickness values as well as the resulting CSR values. The error in the apparent optical thickness due to simply adding values of two layers instead of explicitly simulating it stays below 4%. All cases with errors $> 1.1\%$ employ aerosol with the highest AOT considered of 1.2. The error in the CSR is in general higher than in the apparent optical thickness since for its calculation two τ_{app} -values need to be determined (comp. Eq. 3.21) which are both prone to errors. The adding of apparent optical thickness values seems by trend to introduce a negative bias in the CSR since for over 90% of the considered test cases the parameterized CSR is smaller than the MYSTIC reference value.

For the second test scenario several external aerosol mixtures were considered. Again the broad band apparent optical thickness and the CSR were calculated – once explicitly with MYSTIC and once by adding the parametrized apparent optical thickness values for

¹¹External mixture means that particles of different type are present, whereas internal mixture indicates that individual particles are composed of several components (e.g. particles with a coating).

the individual aerosol species. Overall 230 scenes with a total aerosol optical thickness at 550 nm of either 0.05, 0.10, 0.15, 0.3, 0.4, 0.5, 0.7, 0.9, 1.1, 1.5, 2.0, 3.0 or 5.0 were generated by randomly mixing eight aerosol components from OPAC, namely *insoluble* (*inso*), *water-soluble* (*waso*), *soot*, *mineral nucleation mode* (*minm*), *mineral accumulation mode* (*miam*), *mineral coarse mode* (*micm*), *sea salt accumulation mode* (*ssam*) and *sea salt coarse mode* (*sscm*). That is, after randomly picking one total aerosol optical thickness level τ , each aerosol component i was assigned a random number $t_i \in [0, 1]$, from which the partial aerosol optical thickness values τ_i were computed as

$$\tau_i = \tau \frac{t_i}{\sum_{\text{aer. components}} t_i} \quad . \quad (3.27)$$

Figure 3.16 shows that the relative error in the apparent optical thickness is mostly below 2%. Only for aerosol optical thickness values larger than 1 the error can reach values in the order of 10%. Like in the first test case the errors in CSR can be larger than in apparent optical thickness. At times they reach values in the order of 15%. Below a total aerosol optical thickness of ≈ 0.5 the “adding method” underestimates the CSR values from MYSTIC in tendency while for larger values mostly an overestimation can be observed.

Considering the results of the two test cases I assume that the error in CSR due to application of the “adding method” is on average below 5%. For individual setups the tests showed errors in the range of up to 15%. These errors seem to be acceptable if one considers the greatly enhanced flexibility obtained by the adding method. Note that if linearity can be assumed, i.e. $\Delta k_a \tau_s \ll 1$ (comp. Eq. 3.23), also the CSR is additive and CSR contributions of the individual layers can be separated.

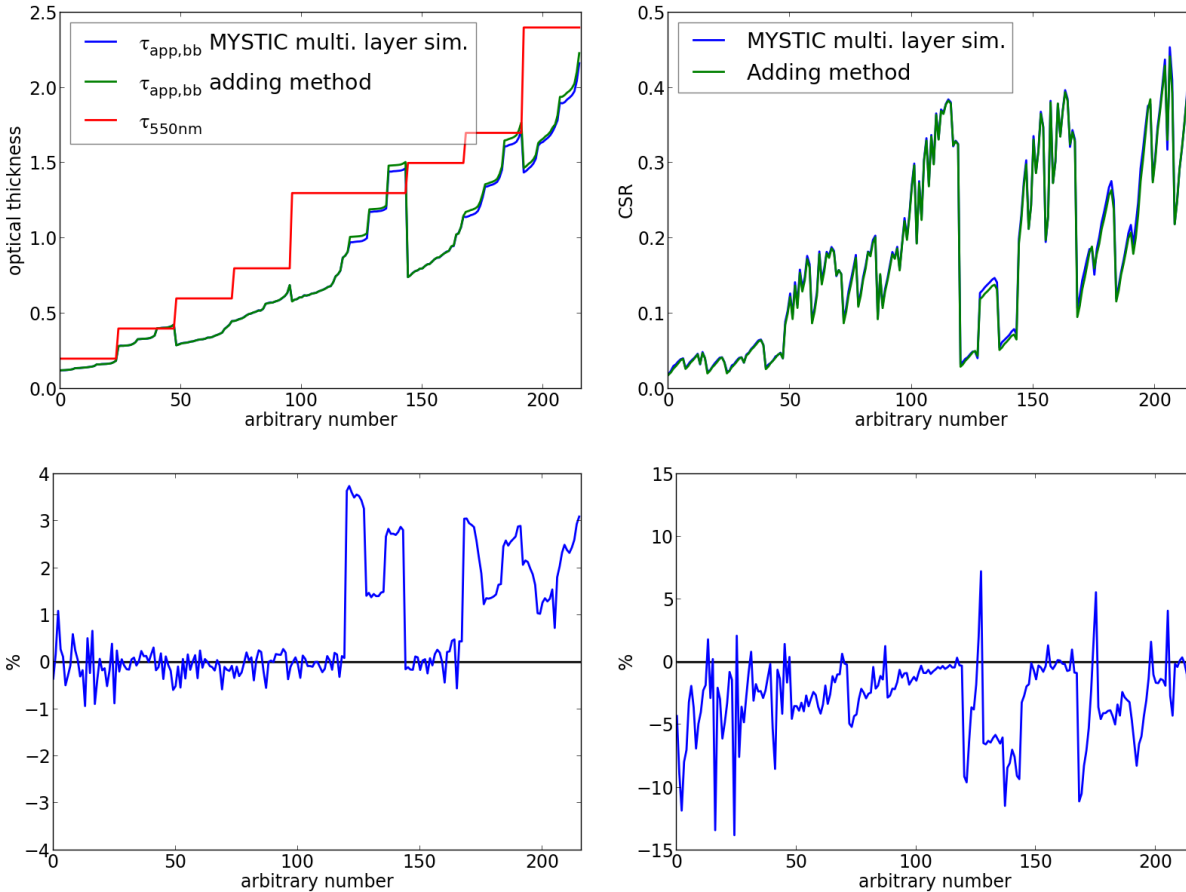


Figure 3.15: Values of apparent optical thickness (left) and CSR (right) for 216 setups of a two layer scene with a cirrus over an aerosol layer. The cirrus is composed of HEY “solid-columns” of varying r_{eff} and an ice optical thickness at 550 nm of 0.1, 0.5 or 1.2. The aerosol layer is composed either of the small, medium or large dust component of the ECMWF IFS aerosol (Sect. 3.3.2) with an aerosol optical thickness of 0.1, 0.3 or 1.2. The diagrams are primarily sorted by increasing combined optical thickness (aerosol + cirrus) at 550 nm (τ_{550nm}) and secondly by apparent optical thickness. Upper left: Broad band apparent optical thickness explicitly simulated with MYSTIC (blue), apparent optical thickness (bb) obtained by adding apparent optical thickness values of the individual layers computed using the k -LUTs (Sect. 3.5, green), combined optical thickness τ_{550nm} (red). Lower left: Relative deviation of the parametrized apparent optical thickness to the MYSTIC reference. Upper right: Resulting CSR values. Lower right: Relative deviation of the parametrized CSR to the MYSTIC reference.

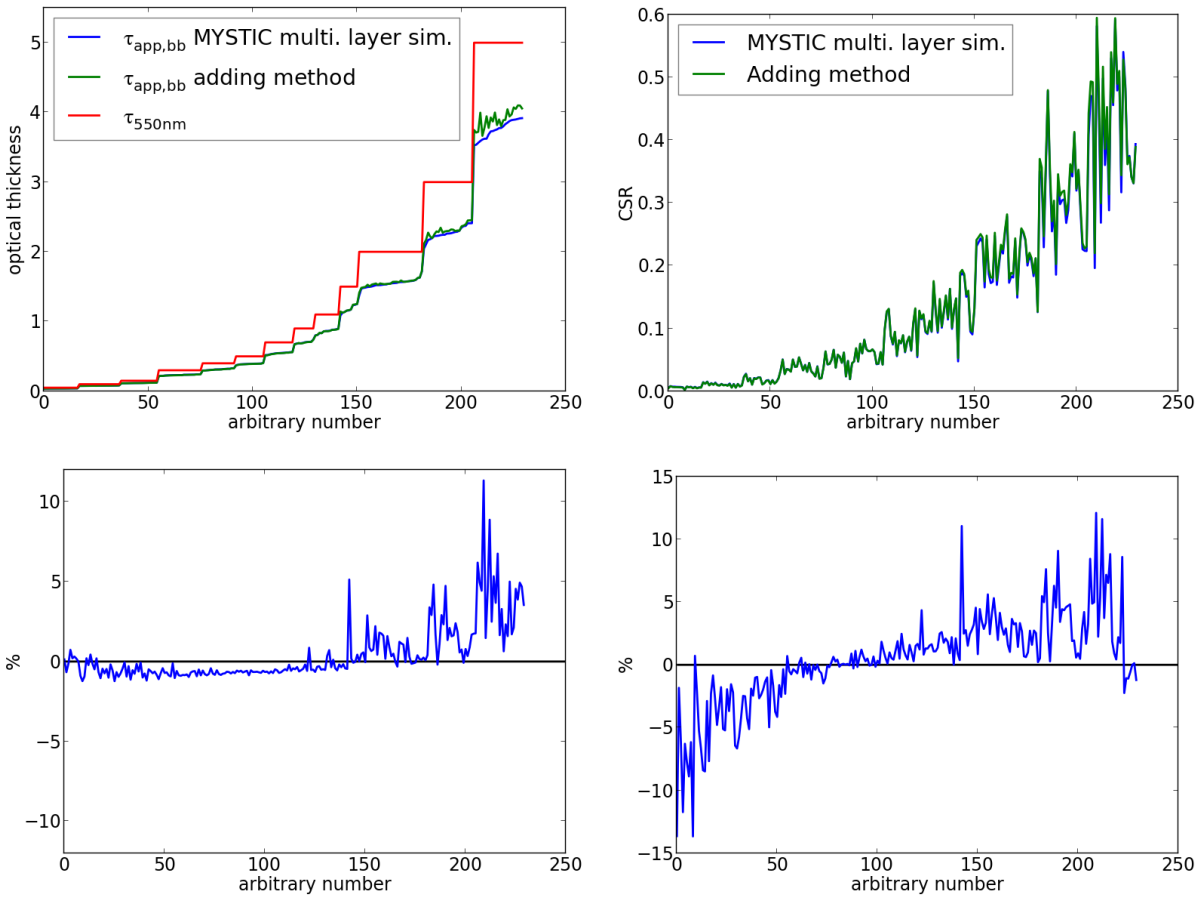


Figure 3.16: Values of apparent optical thickness (left) and CSR (right) for 230 setups with a random external mixture of eight OPAC aerosol components (inso, waso, soot, minm, miam, micm, ssam, sscm). The diagrams are primarily sorted by increasing combined optical thickness which was set to either 0.05, 0.10, 0.15, 0.3, 0.4, 0.5, 0.7, 0.9, 1.1, 1.5, 2.0, 3.0 or 5.0 and secondly by apparent optical thickness. See Fig. 3.15 for description of panels.

3.5.3 Sensitivity of the CSR Parameterization on Sun Zenith Angle

The developed CSR parameterization accounts only indirectly for the sun zenith angle θ_{sun} . It is considered in the conversion from optical thickness to *slant path* optical thickness $\tau_s = \frac{\tau}{\cos(\theta_{\text{sun}})}$. However, the MYSTIC simulations to determine k were always performed with $\theta_{\text{sun}} = 0^\circ$. In the following the impact of this simplification is evaluated with additional simulations. To this end, CSR values calculated from simulations at $\theta_{\text{sun}} = 0^\circ$ were compared to CSR values at $\theta_{\text{sun}} \neq 0^\circ$ but for equal slant path optical thickness values. Limiting angles α_{cir} of 0.5° , 1.0° , 2.0° , 3.0° and 5.0° were considered. The simulations for cirrus clouds were performed with HEY solid-column particles at $r_{\text{eff}} = 5 \mu\text{m}$, $20 \mu\text{m}$, $40 \mu\text{m}$ and $90 \mu\text{m}$ and τ_s varying between 0.2 and 4.0. Simulations for aerosol were performed for the aerosol components *miam* and *ssam* from OPAC as well as the different dust and sea salt components from the IFS with τ_s varying between 0.1 and 3.0.

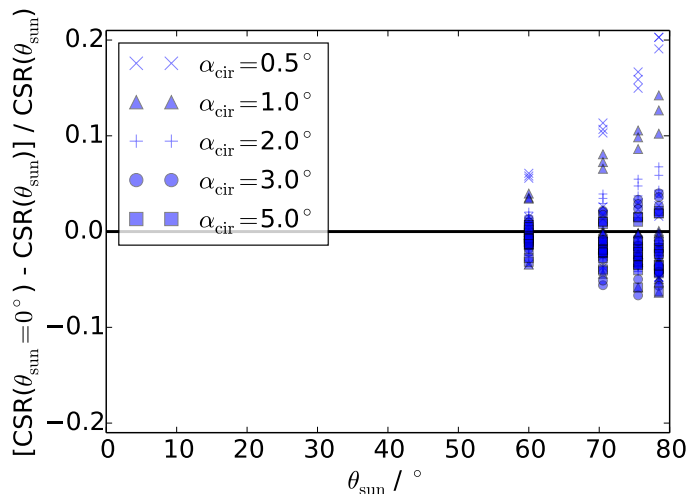


Figure 3.17: Relative deviation of CSR calculated at $\theta_{\text{sun}} = 0^\circ$ and $\theta_{\text{sun}} \neq 0^\circ$ but for the same slant path optical thickness for HEY solid-columns. For detailed description see text.

The relative deviation of the CSR calculated from simulations at $\theta_{\text{sun}} = 0^\circ$ to the reference simulations with $\theta_{\text{sun}} \neq 0^\circ$ are shown in Fig. 3.17 for cirrus clouds and in Fig. 3.18 for aerosol. Considering the cirrus clouds, the deviations stay mostly confined to $\pm 5\%$. The largest calculated deviation amounts to -21% so that it can be concluded that deviations in

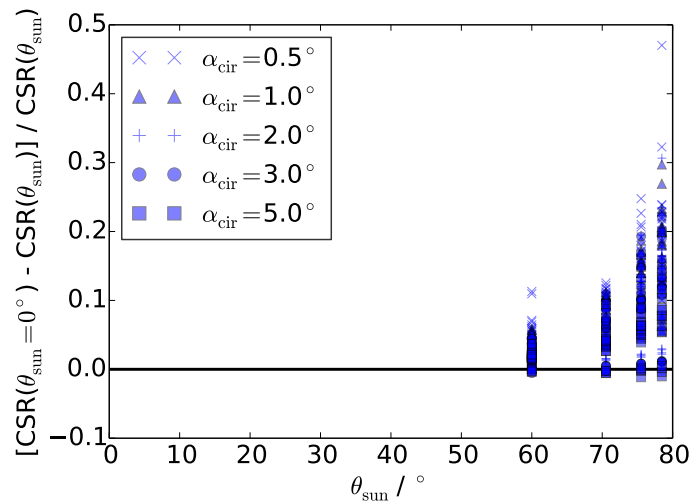


Figure 3.18: Relative deviation of CSR calculated at $\theta_{\text{sun}} = 0^\circ$ and $\theta_{\text{sun}} \neq 0^\circ$ but for the same slant path optical thickness for several aerosol components. For detailed description see text.

the order of 20% must be expected for individual cases. While for cirrus clouds the deviations are distributed around the ± 0 , an overestimation of the CSR at high sun zenith angle was diagnosed for most aerosol setups. To avoid introducing a bias in the results, k -values for aerosol were additionally tabulated at $\theta_{\text{sun}} = 60^\circ$, 70° and 80° . In the computation of CSR this requires an additional linear interpolation step in θ_{sun} .

3.5.4 Sensitivity of the CSR Parameterization on the Scattering Layer's Geometry

If not stated otherwise, cirrus clouds were always placed in a layer between 10 km and 11 km above the ground in the MYSTIC simulations. Aerosol was always evenly distributed in a layer of one kilometer depth directly above the ground. This was founded on the assumption that circumsolar radiation is caused mainly due to single scattering and that Rayleigh scattering contributes only negligibly to the signal. For example, Lohmann et al. (2006) also reported that the cloud geometrical thickness has negligible influence on global horizontal and direct irradiance at the surface. Here this is verified in regard to circumsolar radiation for some scenes by exemplary calculations of the CSR ($\alpha_{\text{cir}} = 3^\circ$). Considering clouds, the cloud height as well as the cloud thickness were varied in the control simulations.

For aerosol, only impact of a change of the thickness of the aerosol layer was assessed, because most of the aerosol will normally be concentrated in the atmospheric boundary layer and not in elevated layers.

Ice clouds composed of HEY solid columns were simulated in a layer 0 km and 1 km above ground. The simulations were then compared to the original simulations. This was done for 92 combinations of slant path optical thickness varying between 0.2 and 4.0, effective radius varying between 5 μm and 90 μm and sun zenith angle varying between 0° and 78°. The deviations from the originally calculated CSR – i.e. for the cirrus in 10 km height – were always below 2% or 0.003 which is below the calculated Monte Carlo uncertainty for most simulations performed for this sensitivity study. Furthermore cirrus clouds of only 300 m thickness between 10.0 km and 10.3 km were simulated using the same parameter combinations. The deviations in CSR from the original simulations with clouds of 1000 m thickness were again below 2% or 0.003.

miam, *ssam* and *sscm*¹² aerosol from OPAC was simulated in a 300 m thick layer above ground. Following, the CSR ($\alpha_{\text{cir}} = 3^\circ$) was compared to the original simulation with a 1 km thick aerosol layer. In the simulations slant path optical thickness values between 0.1 and 3.0 were considered. The sun zenith angle was varied between 0° and 78°. In total simulations for 90 parameter combinations were compared. In all cases the simulations for the thin aerosol layers deviate by less than 1% from the simulations for the thick aerosol layer. These exemplary verification simulations confirm that the circumsolar radiation is not unduly sensitive to the geometry of the scattering layer.

3.5.5 Further Aspects of the Apparent Optical Thickness Approach

Shiobara and Asano (1994) showed that k (Eq. 3.14) can be approximated by evaluating the single scattering phase function P :

$$k \approx 1 - \omega_0 \frac{\int_0^{\alpha_{\text{cir}}} P(\theta) \sin(\theta) d\theta}{\int_0^\pi P(\theta) \sin(\theta) d\theta} \quad (3.28)$$

with ω_0 being the single scattering albedo. I verified this with the cirrus optical properties considered in this study at one wavelength (550 nm) by performing MYSTIC simulations.

¹²*miam*: mineral dust accumulation mode. *ssam*: sea salt accumulation. *sscm*: sea salt coarse mode

The approximation leads to deviations of less than 5% in $k(550 \text{ nm})$ as long as $\tau_s < 3$ and $\alpha_{\text{cir}} > 0.5^\circ$. For smaller angles the extent of the sun which is not captured by the approximation causes larger deviations from the values obtained from MYSTIC simulations. Therefore the more exact results from MYSTIC were used to compute k in this study.

If we consider a non-absorbing medium ($\omega_0 = 1$), Eq. 3.28 can also be written as

$$k \approx \frac{\int_{\alpha_{\text{cir}}}^{\pi} P(\theta) \sin(\theta) d\theta}{\int_0^{\pi} P(\theta) \sin(\theta) d\theta} . \quad (3.29)$$

This means that k is approximated by the relative amount of radiation that is scattered out of the forward direction (i.e. the circumsolar region) by single scattering.

Interestingly the concept of the apparent optical thickness (Sect. 3.5.1) which was originally born out of shortcomings in *measuring direct* radiation shows parallels to a concept developed due to shortcomings in *simulating diffuse* radiation – the well known δ -scaling approach (e.g. Joseph et al., 1976). The basic concept of δ -scaling is that the forward peak of the phase function is truncated which is accounted for by a reduction of the optical thickness. I.e. forward scattered radiation is treated as direct radiation.

3.6 Sensitivity of Circumsolar Radiation to Ice Particle Shape

Of the three parameters determining k (Eq. 3.15) for a cirrus cloud – field of view, effective radius and ice particle shape – the field of view is the only one which is easy to determine. The effective radius can be retrieved from MSG with APICS but is subject to uncertainties, particularly for optically very thin clouds. The ice particle shape cannot be retrieved with passive remote sensing methods like APICS at all. The uncertainties due to this are evaluated in Sect. 4.1, looking at the complete circumsolar retrieval chain – including the cloud property retrieval. In this section the uncertainties which arise in the modelling of circumsolar radiation are evaluated separately. In Fig. 3.19 possible CSR-values are depicted as a function of the field of view for a variety of cirrus clouds, each composed of a random mixture of particles. The left panel shows values for clouds with $\tau_s = 0.4$, the right one for $\tau_s = 2.0$. From the scatter of the data points one can deduce which uncertainties arise in the determination of CSR if either the information about one parameter – particle

shape – or about both parameters – particle shape and effective radius – are absent. The possible CSR values for the whole range of particle shapes and effective radii contained in the k -LUT (see Sect. 3.1) are displayed: If the optical thickness is the only information available, the whole band composed of the different symbols must be considered. In this case the determined values have a large uncertainty. If the effective radius is known, the range of possible values narrows to the band filled by the corresponding symbol type. The remaining uncertainty originates from differences in the optical properties of the ice particle shapes. This is the uncertainty that is inherent to the method even for an otherwise perfect retrieval of the cloud properties τ_s and r_{eff} .

For the slant path optical thickness range of $0 < \tau_s \leq 3$ uncertainties are also depicted directly in Figs. 3.20 and 3.21. The first shows the difference ΔI_{cir} between the maximal and minimal possible values of the circumsolar irradiance in W m^{-2} depending on the field of view and the optical thickness τ_s for all ice optical properties considered in the k -LUT. The latter shows the relative uncertainties in CSR δ_{CSR} for the same parameters, computed as

$$\delta_{\text{CSR}} = \frac{\text{CSR}_{\text{max}} - \text{CSR}_{\text{min}}}{0.5 \cdot (\text{CSR}_{\text{max}} + \text{CSR}_{\text{min}})} \quad . \quad (3.30)$$

In both graphs solid lines stand for a fixed r_{eff} of $25 \mu\text{m}$ and dashed lines for an undefined effective radius. Again it becomes apparent that knowledge about the effective radius reduces the uncertainties considerably.

3.7 Sensitivity of CSR to Aerosol Particle Shape and Relative Humidity

As mentioned in Sect. 3.3.2, libRadtran comes with optical properties for spherical and non-spherical dust particles. The non-spherical particles are modelled as prolate spheroids which exhibit a surface equal to their spherical counterparts. This enables us to evaluate the impact of the aerosol particle shape on the CSR. In Fig. 3.22 CSR values for spherical and aspherical particles are compared considering the three different OPAC dust components. The results are shown only for $\tau_s = 0.5$, but they vary only marginally with changes in τ_s . The differences between spherical and aspherical particles are mostly below 5%, except for the mineral dust nucleation mode type for which the differences can reach up to 14% for

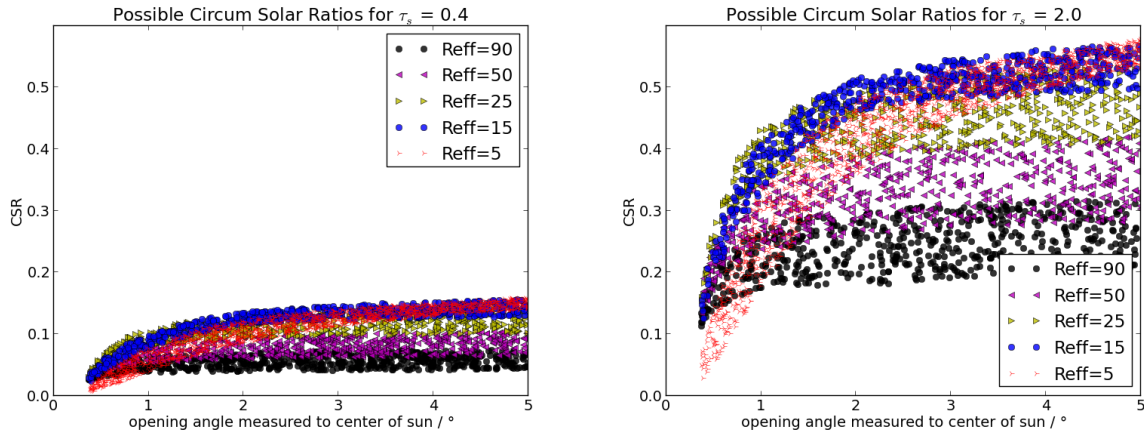


Figure 3.19: Possible CSR-values as a function of the opening angle α_{cir} for a variety of cirrus clouds, each composed of a random mixture of the five particle shapes and the two particle mixtures (described in Sect. 3.1). Left: $\tau_s = 0.4$. Right: $\tau_s = 2.0$. Different symbols denote different effective radii (labeled Reff, units μm).

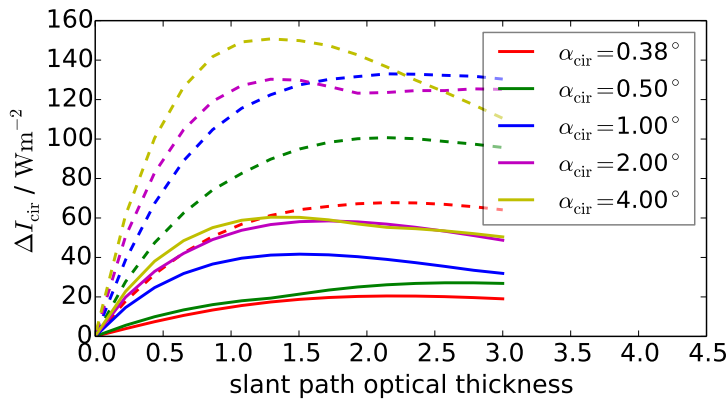


Figure 3.20: Uncertainty in circumsolar radiation for certain field of views (legend gives opening half angle in degrees). Solid lines: For $r_{\text{eff}} = 25 \mu\text{m}$ and undefined ice particle shape. Dashed lines: For undefined r_{eff} and ice particle shape.

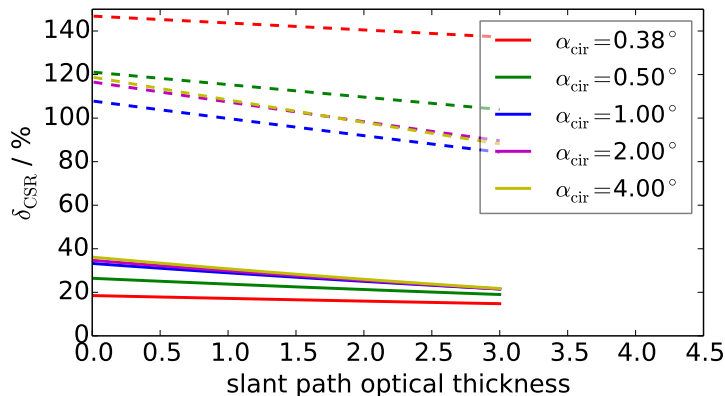


Figure 3.21: Relative uncertainty δ_{CSR} for certain field of views (legend gives opening half angle in degrees). Solid lines: For $r_{\text{eff}} = 25 \mu\text{m}$ and undefined ice particle shape. Dashed lines: For undefined r_{eff} and ice particle shape.

small fields of view ($\alpha_{\text{cir}} < 1^\circ$). This indicates that as long as spheroid particles of equal surface are considered (as in Wiegner et al., 2011), the variation in CSR is small. However for more complex shaped particles further sensitivity studies should be considered.

Besides the aerosol type, the modelled aerosol particle size in the IFS depends on the relative humidity. This was outlined in Sect. 3.3.2 where the hygroscopic growth of some aerosol components was discussed. Figure 3.23 shows how the hygroscopic growth translates into CSR changes. $\text{CSR}(\alpha_{\text{cir}}=2.5^\circ)$ for the different hygroscopic ECMWF aerosol components was calculated at varying relative humidity. Thereby always the same aerosol dry mass area loading was used corresponding to $\tau_{s,550\text{nm}} = 0.5$. It shows that for some aerosol types changes of approximately a factor of 2 compared to the CSR values at 50% RH must be expected due to changes in the relative humidity.

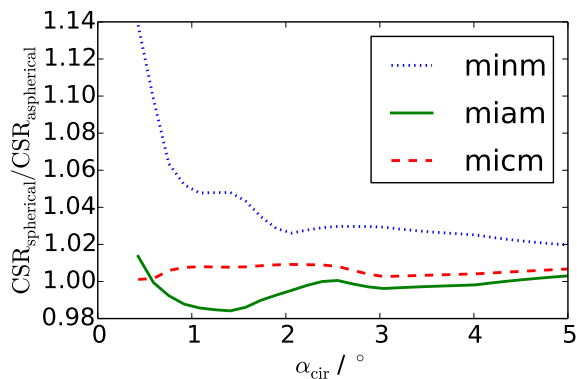


Figure 3.22: Parameterized CSR for varying field of view obtained for spherical dust particles divided by CSR for aspherical dust particles. Three curves for the different OPAC dust aerosol components: Dotted blue: Mineral dust nucleation mode (*minm*), Solid green: Mineral dust accumulation mode (*miam*), dashed red: Mineral dust coarse mode (*micm*).

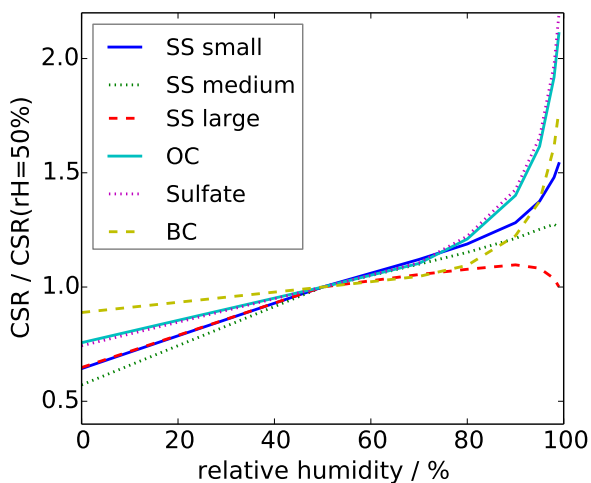


Figure 3.23: Parameterized CSR at constant aerosol area dry mass loading for varying relative humidity (RH) divided by CSR at 50% RH. Different lines for the different hygroscopic ECMWF aerosol components. SS: sea salt, OC: organic carbon, BC: black carbon.

Chapter 4

Results

The results of the study are presented in this chapter. It starts with an intercomparison of cirrus related CSR for different ice particle shapes (Sect. 4.1). Next, results for aerosol and cirrus related CSR are validated against ground measurements performed at the PSA (Sect. 4.2). Finally, in Sect. 4.3 some characteristics of cirrus related circumsolar radiation are derived. For aerosol this step was omitted, as the validation proofed the results not to be reliable enough (see also discussion in Sect. 5.1).

4.1 Intercomparison of Retrieval Results for Different Ice Particle Shapes

In Sects. 3.1 and 3.6 it was outlined that uncertainties exist in the cloud property retrieval as well as in the conversion of these properties to CSR values due to the unknown ice particle shape (mixture). It is not obvious how these uncertainties interact, in particular, whether they cancel at least partially. Therefore the overall variability was investigated by applying the complete retrieval chain yielding circumsolar radiation from SEVIRI measurements several times using different setups.

To this end CSR values for a limiting angle $\alpha_{\text{cir}} = 2.5^\circ$ have been retrieved from one year (May 2011 – Apr. 2012) within the SEVIRI test sector (Fig. 2.4). This was performed for the five ice particle shapes and the two shape mixtures described in Sect. 3.1. I.e. seven distinct APICS runs were performed with different cloud optical properties. In the following conversion from the retrieved cloud properties to CSR values, optical properties

for the same particle shape were used as in the correspondent APICS run, so that seven different CSR datasets were obtained in total.

A histogram of the occurrence of CSR values relative to all time steps with $\theta_{\text{sun}} < 80^\circ$ was computed for every ice particle shape, considering the whole domain. These histograms are shown in the upper panel of Fig. 4.1 which gives a first illustration of the uncertainty induced by not knowing the particle shape. The “Baum” optical properties are based on a realistic mixture of particle shapes, so that an operational retrieval would rely on them rather than on individual particle shapes. Therefore the corresponding lines are highlighted. The lower panel of Fig. 4.1 shows basically the same histogram, but this time only values contribute that go along with total irradiance values $I_{\text{tot},\alpha=2.5^\circ} > 200 \text{ W/m}^2$. I considered this to be the lower operation limit of a hypothetical CST plant. Here the occurrence is shown relative to all time steps that fulfil $I_{\text{tot},\alpha=2.5^\circ} > 200 \text{ W/m}^2$, i.e. inclusive corresponding clear sky time steps. For the calculation of $I_{\text{tot},\alpha=2.5^\circ}$ the clear sky direct irradiance I_0 is required (Eq. 3.19). It was obtained from libRadtran calculations which were performed with a θ_{sun} -resolution of 1° and interpolated in between. Thereby the elevation was set to 0 m above sea level. In the presence of water clouds, $I_{\text{tot},\alpha=2.5^\circ}$ was assumed to be below the 200 W/m^2 threshold because water clouds are at most times optically too thick to allow higher values. These cases were identified with a general cloud mask from EUMETSAT (EUM OPS DOC 09 5164; EUM MET REP 07 0132). Pixels marked cloudy in this mask but not in the COCS cirrus cloud mask were assumed to contain water clouds. While on average 22% of the SEVIRI measurements in the test data set produce a cirrus cloud detection, only 8%-10% additionally satisfy the 200 W/m^2 criterion (depending on the assumed ice particle shape).

To gain insight into how much the retrieval results scatter, Fig. 4.2 shows, as example, the distribution of CSR from the retrieval with “Baum v2.0”, which was applied to a subset of SEVIRI measurements – namely to the subset for which the retrieval with “Baum v3.5” yielded CSR values between 0.17 and 0.18. Ideally, if the ice particle shape had no influence, all “Baum v2.0” results would also fall into the same interval. However in reality the distribution is clearly wider.

Figure 4.3 gives a more complete comparison of the scatter between the different optical properties: For this purpose, the SEVIRI measurements were binned into CSR intervals (retrieved using “Baum v3.5”) of width 0.01. Each subset is then processed again assuming other cloud optical properties (specified in the y-axis label of each panel). The resulting new CSR distribution is then color-coded along the y-axis. Figure 4.2 shows the “Baum

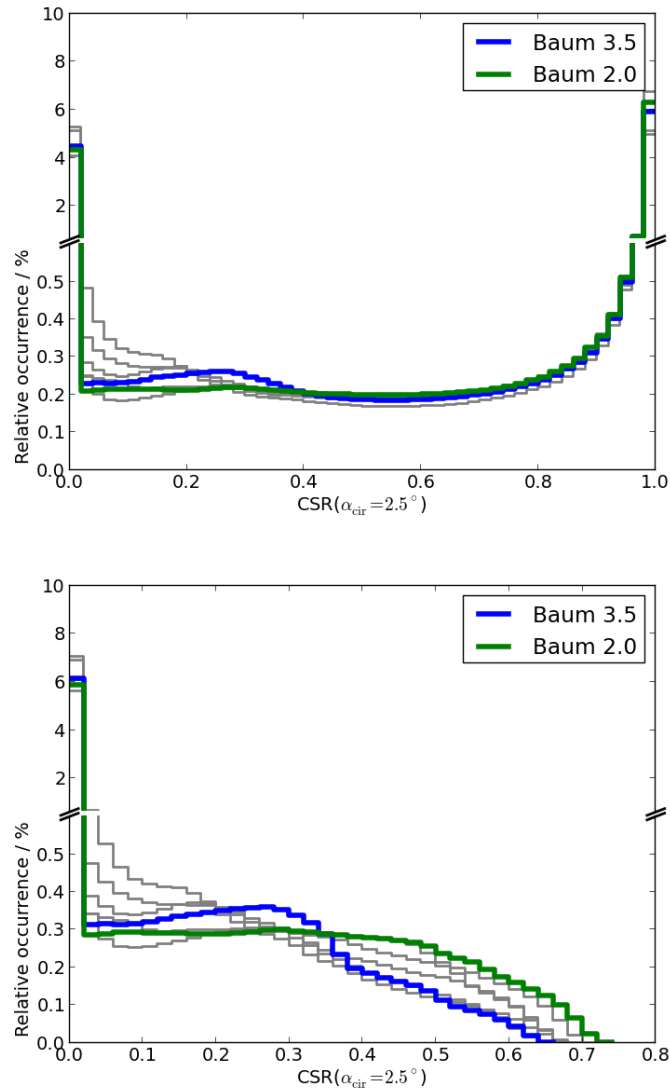


Figure 4.1: Histograms of the relative occurrence of CSR values in case of cirrus clouds for one year within the test sector for different assumed ice particle shapes. Results for the “Baum” ice particle mixtures are shown colored. Results for the different individual ice particle shapes from HEY are shown in grey. Upper panel: Histograms of the relative occurrence with respect to the total number of SEVIRI measurements with $\theta_{\text{sun}} < 80^\circ$. Lower panel: Histograms of the relative occurrence of CSR values under the condition $I_{\text{tot},\alpha=2.5} > 200\text{W}/\text{m}^2$ (lower operation limit of the assumed hypothetical CST plant) with respect to the total number of SEVIRI measurements with $I_{\text{tot},\alpha=2.5} > 200\text{W}/\text{m}^2$.

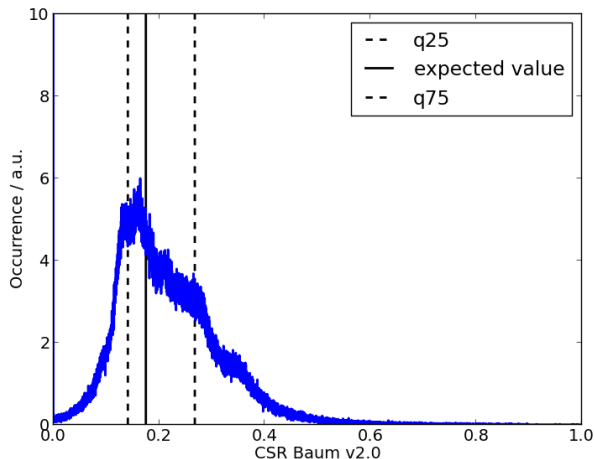


Figure 4.2: Normalized distribution of retrieval results using “Baum v2.0” for SEVIRI measurements for which the retrieval with “Baum v3.5” yielded values between 0.17 and 0.18. Dashed lines mark the 25th and 75th percentiles (q_{25} & q_{75}).

v2”-CSR-distribution within one of these subsets and is simply a vertical cross section through the upper left panel. From Fig. 4.3 one can see that droxtals yield quite different CSR results than “Baum v3.5”: The results within the individual CSR subsets scatter widely and most times droxtals yield smaller CSR values than “Baum v3.5” (distribution is curved to lower values). Hollow columns and rough aggregates have rather narrow distributions but also show some curvature – implying a bias compared to “Baum v3.5”. Rosettes produce a relatively narrow distribution close to the 1:1 line. The distributions for “Baum v2.0” and solid columns are quite similar, being rather broad with no clear bias visible.

4.2 Validation

In the following parameterized CSR values (CSR_{param}) are compared to ground measurements of the CSR (CSR_{SAMS}) performed at the Plataforma Solar de Almería with SAMS (Sect. 2.7). First the CSR parameterized from ECMWF IFS modelled aerosol data is evaluated in Sect. 4.2.1, before the satellite based CSR parameterization for clouds is reviewed in Sect. 4.2.2. The SAMS measurements show varying frequency but were generally performed at least once per minute, except for a few days which had to be discarded due to

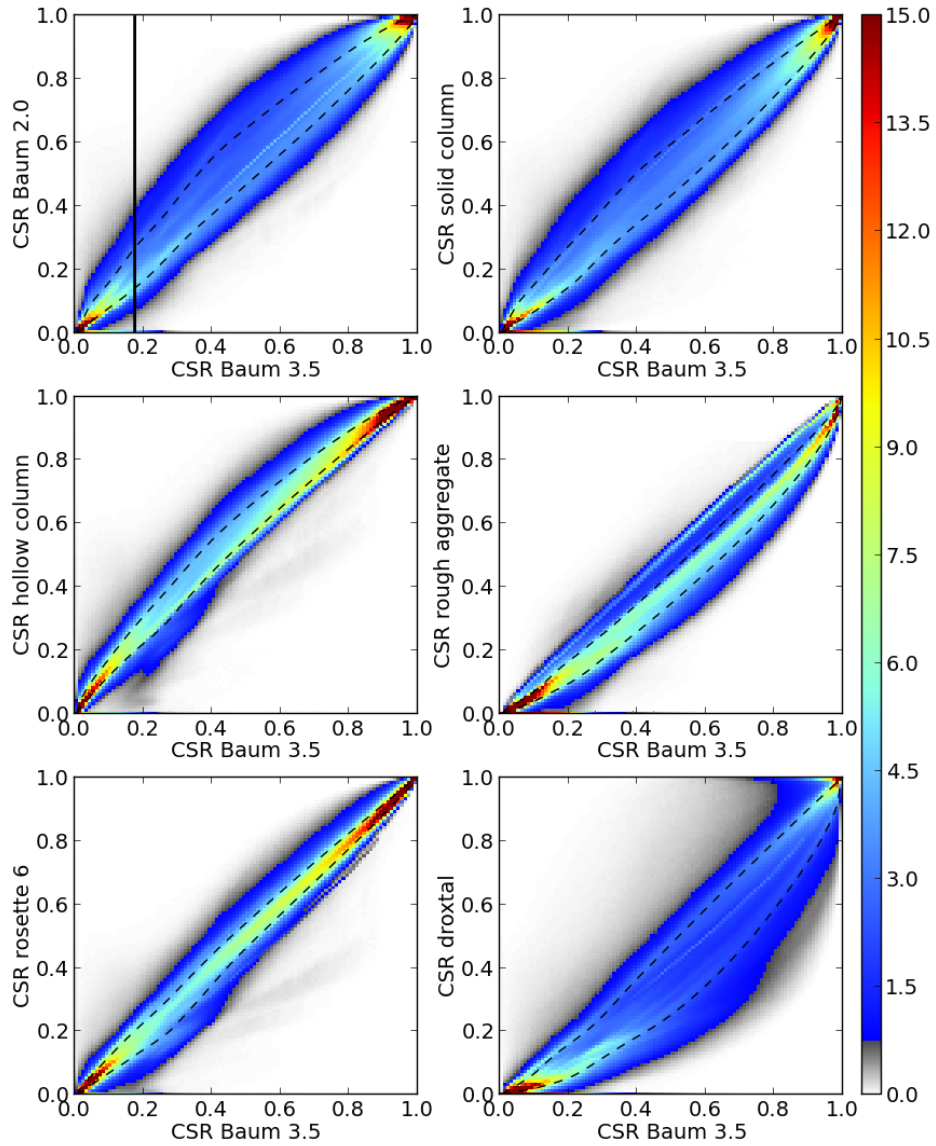


Figure 4.3: Normalized CSR retrieval distributions for 100 bins of CSR from “Baum v3.5” (x-axis, bin width 0.01). Dashed lines mark q_{25} and q_{75} , i.e. they enclose 50% of the measurements. Black vertical line in upper left panel marks the cross section that is displayed in Fig. 4.2.

technical failures of the instrument. Unless stated otherwise, the CSR refers to an opening half-angle of 2.5° in this section and one year of data was evaluated (May 2011 – Apr. 2012).

Following measures were used for an objective validation: The relative bias, the mean absolute deviation (MAD), the root-mean-square deviation (RMSD), the Pearson correlation r (Wilks, 2005, Eq. 3.23) and the Spearman rank correlation r_{rank} (Wilks, 2005, Eq. 3.28). The RMSD and the Pearson correlation are provided since they are widely used validation measures, however it should be noted that they have to be interpreted with care: The deviations between the SAMS measured and the satellite retrieved values are not necessarily normally distributed such that an interpretation of the RMSD in terms of a standard deviation may be misleading. Furthermore the RMSD strongly penalizes outliers which, for example, can easily be caused by collocation errors of satellite data. Also can a truly linear relationship between the CSR from SAMS and from the developed parameterization not be expected which may deteriorate Pearson correlation values. This is because errors in Δk or τ_s will not propagate linearly (comp. Eq. (3.22)) – at least not for cirrus clouds with $\Delta k_\alpha \tau_s$ being *not* much smaller than 1. For N evaluated CSR tuples the corresponding formulas are:

$$\text{Bias} = \frac{\sum_{i=1}^N \text{CSR}_{\text{param},i} - \sum_{i=1}^N \text{CSR}_{\text{SAMS},i}}{\sum_{i=1}^N \text{CSR}_{\text{SAMS},i}} \quad (4.1)$$

$$\text{MAD} = \sum_{i=1}^N \frac{|\text{CSR}_{\text{param},i} - \text{CSR}_{\text{SAMS},i}|}{N} \quad (4.2)$$

$$\text{RMSD} = \sqrt{\sum_{i=1}^N \frac{(\text{CSR}_{\text{param},i} - \text{CSR}_{\text{SAMS},i})^2}{N}} \quad (4.3)$$

$$r = \frac{\frac{1}{N-1} \sum_{i=1}^N [\text{CSR}'_{\text{param},i} \text{CSR}'_{\text{SAMS},i}]}{\left[\frac{1}{N-1} \sum_{i=1}^N (\text{CSR}'_{\text{param},i})^2 \right]^{1/2} \left[\frac{1}{N-1} \sum_{i=1}^N (\text{CSR}'_{\text{SAMS},i})^2 \right]^{1/2}} \quad , \quad (4.4)$$

where primes denote anomalies from the mean values. The Spearman rank correlation r_{rank} is simply the Pearson correlation applied not on the data but on the ranks of the data. It is not a measure of linear relationship but of monotone relationship. The Pearson correlation is neither robust nor resistant while the Spearman rank correlation is – contrasting the Pearson correlation it requires no assumption about the kind of monotone relationship and

is not unduly influenced by few outliers (Wilks, 2005, Chap. 3).

4.2.1 Validation of Aerosol Related Circumsolar Radiation

In this section, CSR parameterized from aerosol data from the IFS near-real-time forecast is compared to SAMS measurements. No information about the relative humidity is included in the NRT data. Therefore the parameterized values refer to a relative humidity of 50%, unless stated otherwise.

The cloud free SAMS measurements, falling in the timespan of ± 7.5 min around the quarter hour, were averaged by calculating their arithmetic mean. This reduces potential random measurement errors, and allows for a comparison to the parameterized CSR values, which were also computed by the quarter hour (comp. Sect. 3.3.3). The cloud free state was initially assessed via the cloud flag in the SAMS dataset. IFS output was taken from the “nearest neighbour” column of the model to the PSA. Evaluating one year (May 2011 – Apr. 2012), 7972 data tuples were generated.

If the parameterization is applied straight on, the resulting CSR values are on average clearly too low. The bias is -73%. In the histogram shown in Fig. 4.4 the parameterized CSR values stay mostly confined to the first two bins (below 0.01) while the measured CSR is broader distributed. Not only are the parameterized CSR values too low, they also correlate only weakly with the measured values. For the initially processed 7972 data tuples the Spearman rank correlation is only 0.25. It turns out, that the measured CSR often fluctuates considerably on the scale of minutes, even if no cloud is detected by SAMS. Examination of sky images from an automated camera positioned besides the SAM instrument revealed one possible reason for this. The CSR fluctuations are often caused by non-condensing convection, which appears as highly variable haze plumes, but sometimes also by clouds that are not detected by SAMS. These fluctuations occur on scales that are not resolved by the model. Furthermore both phenomena can cause increased CSR values which cannot be captured by the parameterization.

To evaluate how the parameterized CSR performs in a stable, purely aerosol dominated situation the data set is filtered: If there are measured CSR values within the 15 min averaging period which deviate by more than 50% from the mean for this period, this period is discarded from evaluation. Furthermore, if the mean CSR for a period deviates too much from the preceding or following one, it is discarded as well: Only periods are

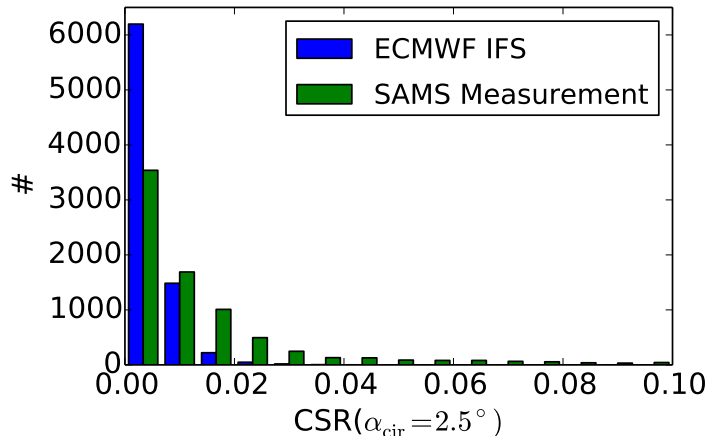


Figure 4.4: Blue: Histogram of $\text{CSR}(\alpha_{\text{cir}} = 2.5^\circ)$ for the PSA due to aerosol, parameterized from IFS output. Green: Histogram of $\text{CSR}(\alpha_{\text{cir}} = 2.5^\circ)$ measured by SAMS at the PSA at times without a cloud flag in the SAMS dataset, averaged over 15 min. 7972 data points in total. 253 data points of SAMS $\text{CSR} > 0.10$ not shown.

considered for which the relative change in $\text{CSR} \cdot \cos(\theta_{\text{sun}})$ is smaller than 5%. Here, the CSR is multiplied by $\cos(\theta_{\text{sun}})$ to equalize deviations caused solely by a changing sun zenith angle to first order. To ensure stable clear sky conditions, it is further required that at least four averaging periods in a row meet these conditions. Data tuples belonging to smaller contiguous groups are discarded as well. This stringent filtering leaves 1081 data points. Still, the parameterized values are on average too low (Bias -67%). Also the Spearman correlation is quite low (30%).

One reason for the poor agreement between the datasets lies probably in the underestimation of the concentration of the largest aerosol particles by the IFS. The largest aerosol particles are most relevant for the forward scattering peak but not necessarily for the optical thickness. Indeed it is known that the evaluated model version suffers from too much small dust particles at the expense of the larger ones (pers. comm. J.-J. Morcrette). Nevertheless, a comparison of the Ångström exponent α shows that the model can dis-

criminate between situations with large or small aerosol particles dominating scattering. The Ångström exponent is a qualitative indicator of particle size. It is defined as

$$\dot{\alpha} = - \frac{\log \frac{\tau_{\lambda_1}}{\tau_{\lambda_2}}}{\log \frac{\lambda_1}{\lambda_2}}, \quad (4.5)$$

with τ_{λ_1} and τ_{λ_2} being the aerosol optical thickness at the different wavelengths λ_1 and λ_2 . Ångström exponents $\lesssim 1$ indicate that the size distribution is dominated by large particles with radii $\gtrsim 0.5 \mu\text{m}$, or vice versa (Schuster et al., 2006). The Ångström exponent was calculated from IFS aerosol area mass loadings utilizing the aerosol optical properties created for this study. In Fig. 4.5 it is compared to the Ångström exponent computed from aerosol optical thickness values determined by the AERONET-processing scheme¹ (Holben et al., 1998), which is applied to the Cimel sun photometer data from the PSA. The IFS is able to coarsely reproduce the temporal evolution of the Ångström exponent measured at the PSA, although it exhibits on average lower values. At first this may seem contradictory to the CSR bias, as a smaller Ångström exponent in principle means larger particles. However, it should be mentioned that while the Ångström exponent tells if coarse mode aerosol is present or not, it cannot be used to determine whether the concentration of the largest particles is indeed correct. This is because the scattering efficiency – and therefore the Ångström exponent – exhibits only a weak dependence on particle size for particles considerably larger than the wavelength of the light.

One has to realize that the parameterization of CSR from IFS modeled aerosol data cannot be applied straight on. Two reasons have been identified for this: On one hand the CSR often fluctuates substantially on scales that are not resolved by the model, even in clear sky conditions. On the other hand, the parameterized values are considerably too low, even for stable clear sky conditions. Also the disregard of the hygroscopic growth of some aerosol components cannot explain the strong bias: The difference in mean CSR parameterized assuming a constant relative humidity of 50% and 99% amounts to about 25%.

For these reasons, the IFS dataset was not evaluated globally because the results would probably be not reliable. However, in Sect. 5.1 the possibility of a statistical post-processing of the IFS output to obtain reasonable CSR data is discussed.

¹Level 1.5 data, i.e. automatically cloud screened, but final a posteriori calibration not applied.

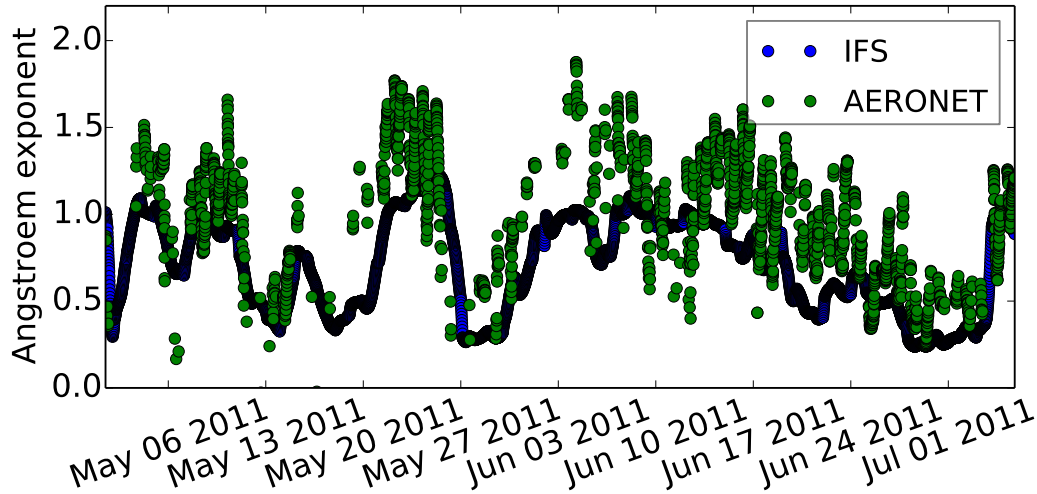


Figure 4.5: Green dots: Ångström exponent (440 nm/870 nm) calculated from aerosol optical thickness values measured by the AERONET Cimel sun photometer at the PSA (Level 1.5 data). Blue dots: Ångström exponent (440 nm/870 nm) calculated from IFS aerosol concentration for the corresponding model column utilizing the optical properties described in Sect. 3.3.2.

4.2.2 Validation of Cirrus Related Circumsolar Radiation

In the following CSR retrieved from SEVIRI measurements for cirrus covered sky are compared to ground measurements of the CSR performed with SAMS at the PSA.

The comparison of satellite data with ground measurements is not trivial due to the different spatial footprints and viewing geometries of the instruments. To get a best possible match methods discussed by Greuell and Roebeling (2009) were applied: A correction of the parallax displacement, which results from the two instruments (SAMS & SEVIRI) looking at an elevated cloud layer under different geometries, was used². A schematic drawing of the measurement geometry of SAMS and SEVIRI in Fig. 4.6 illustrates this parallax correction of the SEVIRI measurements. In case of circumsolar radiation measurements a parallax correction must consider not only the satellite viewing geometry but also the sun geometry since SAMS looks into the sun. For these corrections the cirrus was assumed to lie between altitudes of 9 and 11 km. First, the algorithm determines the geographic location of the atmospheric volumes between 9 and 11 km corresponding to the SEVIRI

²Courtesy of Luca Bugliaro, DLR

pixels which are geo-referenced at 0 km altitude. This step depends on the viewing geometry of SEVIRI. In the following, those SEVIRI pixels are selected whose corresponding elevated atmospheric volumes are crossed by the line of sight between SAMS and the sun. If more than one SEVIRI pixel is identified as relevant, the retrieved optical thickness and effective radius values of the pixels are averaged. However, the effective radius is averaged only over cirrus covered pixels. To reduce short term variability which can deteriorate the validation results if the SEVIRI and SAMS measurements are not perfectly collocated, the already parallax corrected cloud property retrieval results from three consecutive SEVIRI measurements at times $t_0 - 15$ min, t_0 and $t_0 + 15$ min were temporally averaged, before the CSR was computed from this average. Collocation errors can be caused by wrong assumptions about the cloud height and thickness but also by deviations in the registration of SEVIRI pixels to latitude/longitude values (comp. Sect. 2.3.1).

The SAMS measures CSR only at one place while the method developed in this study delivers an average value for several square kilometers. To alleviate this scale discrepancy the ground measurements were brought to the same time grid as the SEVIRI measurements by averaging them within a symmetrical time span Δt around t_0 . The averaging of the CSR from SAMS was performed applying a Gaussian weighting function w to the measurements

$$w = \exp \left[\frac{-2(t - t_0)^2}{\Delta t^2} \right] \quad (4.6)$$

with t being the time of the SAMS measurement and t_0 being the time of the central SEVIRI measurement. Underlying this is the assumption that a *temporal* average of the advected cloud properties is representative of the *spatial* average of cloud properties retrieved at distinct times from SEVIRI. I found the averaging time of 35 min to deliver better agreement between satellite and ground measurements than without the averaging, and did not see considerable improvement for longer averaging times. Therefore I used this value for Δt . Only SAMS measurements meeting the condition

$$|t - t_0| < \Delta t = 35 \text{ min} \quad (4.7)$$

were considered. The Gaussian therefore has not to be evaluated to \pm infinity, but is cut off at these limits.

Before comparing CSR values for a 2.5° field of view the measurements were filtered: Only time steps were considered with a positive cirrus cloud detection from MSG. I.e. at least one of the SEVIRI pixels considered in the parallax correction process at $t_0 - 15$ min, t_0

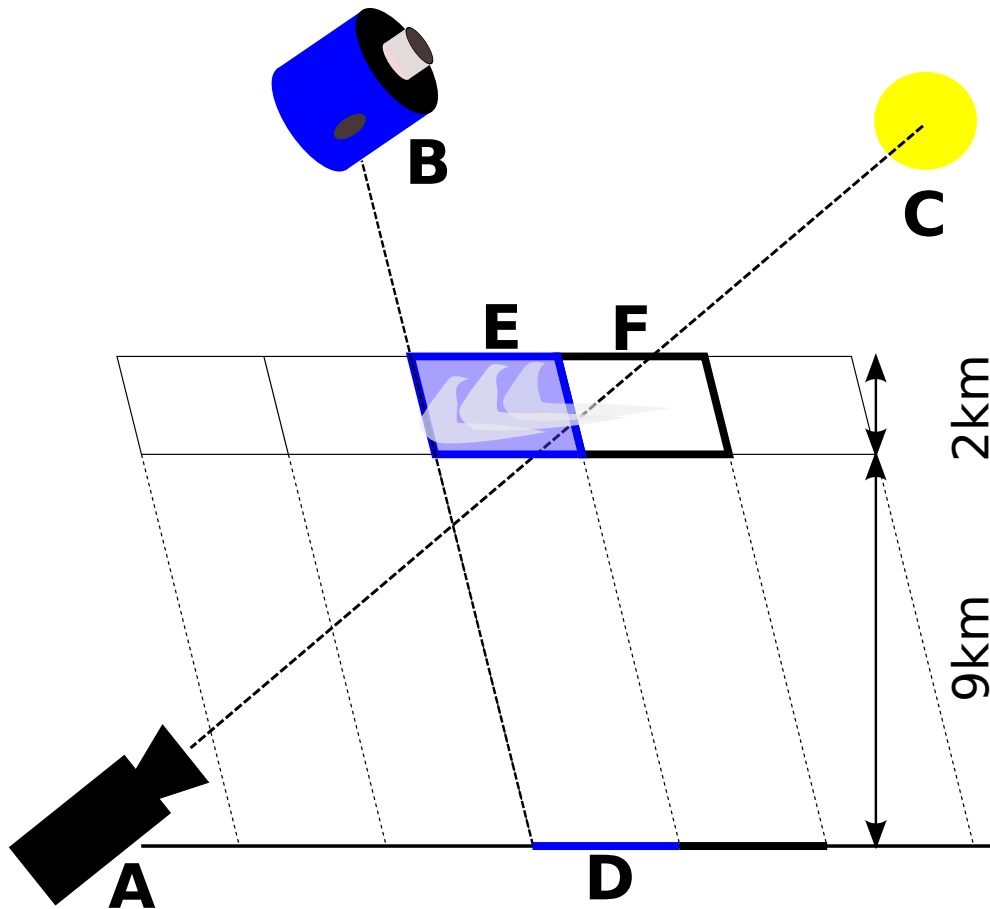


Figure 4.6: Schematic drawing of the different measurement geometries of SAMS and SEVIRI (not to scale) as illustration of the parallax correction of SEVIRI measurements. A: SAMS. B: MSG satellite. C: Sun. D: Original SEVIRI grid referenced on the ground. E and F: Atmospheric volumes between 9 km and 11 km probed by SEVIRI and SAMS. If a cirrus is detected from MSG within E but not within F, as illustrated in the drawing, the retrieved optical thickness is averaged over E & F. The effective radius is solely averaged over cloudy pixels, for the illustrated case this means that the value of E is preserved.

and $t_0 + 15 \text{ min}$ was required to be cloudy. Furthermore I required the total irradiance $I_{\text{tot},\alpha=2.5^\circ}$ calculated from the averaged SEVIRI measurements to be above 200 W/m^2 to ensure relevance for CST plants.

Excerpts of the filtered time series for three days are shown as example in Fig. 4.7. From the figure it becomes apparent that the temporal evolution of the CSR measured by SAMS is in general captured by the satellite time series, but there are timing and amplitude errors so that the CSR values at a given time often disagree.

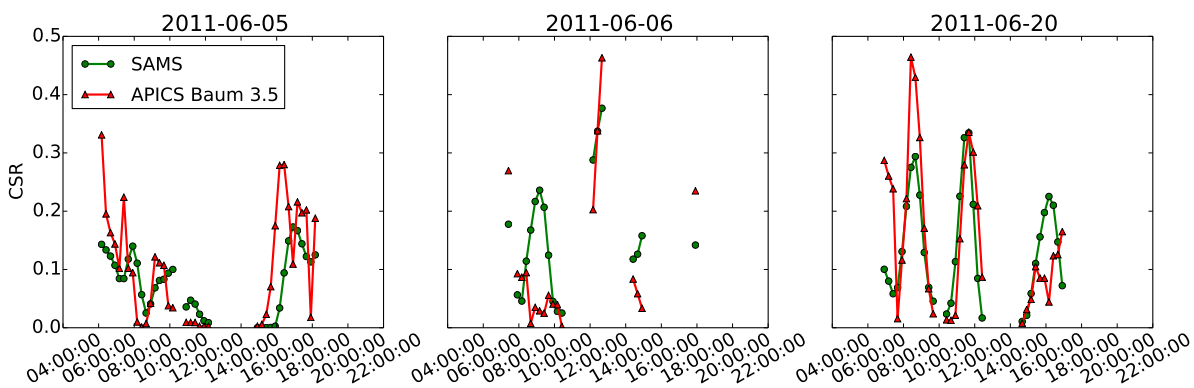


Figure 4.7: Exemplary excerpt of the CSR time series used for the validation. Time is given as UTC.

In Tab. 4.1 the different validation measures are listed which were introduced at the beginning of this chapter. The rank correlation between 0.48 and 0.54 (depending on employed optical properties) and the MAD of 0.11 show that there are often considerable differences between the time series if instantaneous values at a given time are compared. However, the statistical values of CSR are more important than the instantaneous ones for long-term CST system performance prediction (e.g. Rabl and Bendt, 1982). Therefore, Fig. 4.8 compares the histograms of CSR from SAM and retrieved from SEVIRI using “Baum v3.5”. Although there are some differences, the histograms compare well considering the two completely different methods operating on different scales. It is also encouraging that the bias value for both employed “Baum” optical property sets is close to zero (4% and -11% respectively, see Tab. 4.1). With Figs. 4.7 & 4.8 in mind, I therefore conclude that the presented method is suitable to generate typical distributions or time series of the cirrus related CSR.

To locate reasons for the disagreement between the two time series considering instantana-

neous values, sky images from an automated camera positioned besides the SAM instrument were examined. After a manual inspection of the data series and the sky images it was suspected that presence of water clouds (in most cases cumuli) might compromise the results. The cumulus clouds – also if only covering a SEVIRI pixel partly – will increase the reflectivity in the SEVIRI 0.6 μm channel. This will result in APICS retrieving an increased optical thickness for the cirrus. This hypothesis was tested with a shortened version of the evaluation time series (01 May 2011 – 30 Jun. 2011). For this period the data were additionally filtered by hand, leaving only slots without cumuli visible in the sky camera images. Table. 4.2 contains the validation measures for the shortened time series. The numbers within parentheses in Tab. 4.2 were obtained without the manual cumulus clouds screening as reference. The validation measures are improved by the manual filtering: The rank correlation and correlation are increased and the MAD is decreased compared to the unfiltered dataset. Figures 4.9 and 4.10 show two examples from the series of sky images which was manually evaluated for the cumulus cloud screening. On 06 Jun. 2011 (Fig. 4.9) clouds at different atmospheric levels with high spatial variability were present during most of the day. Consequently this day was removed from the time series in the manual cumulus cloud screening. On this day pronounced disagreements between the two time series are observable (comp. Fig. 4.7). In the image in Fig. 4.10 the sky appears rather homogeneous. The clouds are clearly identified as cirrus clouds by the presence of a halo. The image was acquired at 08 UTC on 20 Jun 2011. This date is also depicted in Fig. 4.7. At this time the parameterized CSR matches the measured one. This limited evaluation indicates that an automated cloud detection excluding pixels contaminated with water clouds would be beneficial for future applications of the circumsolar radiation retrieval.

Table 4.1: Results of the comparison of CSR measured from ground and retrieved from SEVIRI for different setups: Rank correlation $r_{\text{rank,CSR}}$, Pearson correlation r_{CSR} , mean absolute deviation MAD, root mean square deviation RMSD, bias and the number of compared data tuples N .

| Optical Properties | $r_{\text{rank,CSR}}$ | r_{CSR} | MAD | RMSD | Bias | N |
|--------------------|-----------------------|------------------|------|------|------|------|
| Baum v2.0 | 0.54 | 0.50 | 0.11 | 0.16 | 4% | 2021 |
| Baum v3.5 | 0.48 | 0.44 | 0.11 | 0.15 | -11% | 1890 |

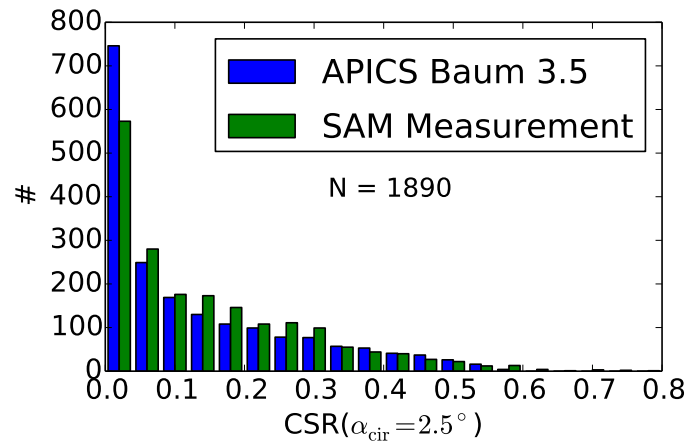


Figure 4.8: Histograms of CSR measured by SAMS (green) and retrieved from SEVIRI (blue) as used for the validation in Sect. 4.2.2.



Figure 4.9: Image of the sky acquired by an automated camera at the PSA on 06 Jun 2011 at 12 UTC (Courtesy of Stefan Wilbert, DLR).



Figure 4.10: Image of the sky acquired by an automated camera at the PSA on 20 Jun 2011 at 08 UTC (Courtesy of Stefan Wilbert, DLR).

Table 4.2: Same as Tab. 4.1 but for the shortened time series (01 May 2011 – 30 Jun. 2011) which was manually cumulus screened. Values in parenthesis are for unscreened time series.

| Optical Properties | $r_{\text{rank,CSR}}$ | r_{CSR} | MAD | RMSD | Bias | N |
|--------------------|-----------------------|------------------|-------------|-------------|-----------|-----------|
| Baum v2.0 | 0.79 (0.68) | 0.75 (0.62) | 0.08 (0.10) | 0.12 (0.14) | 18% (14%) | 220 (407) |
| Baum v3.5 | 0.76 (0.65) | 0.67 (0.58) | 0.07 (0.09) | 0.10 (0.13) | -7% (-7%) | 213 (386) |

4.3 Characteristics of Cirrus-Related Circumsolar Radiation

4.3.1 Spatial Distribution

The average circumsolar irradiance and CSR during CST plant operation is strongly dependent on the lower DNI limit the plant can work at. To provide an example of the spatial distribution of the circumsolar radiation, I consider again a hypothetical power plant with a lower operation limit of $I_{\text{tot},\alpha=2.5^\circ} > 200 \text{ W/m}^2$ like in Sect. 4.1. Figure 4.11 shows two maps of the circumsolar irradiance $I_{\text{cir},\alpha=2.5^\circ}$ averaged over all time steps with $I_{\text{tot},\alpha=2.5^\circ} > 200 \text{ W/m}^2$ – one for the “Baum v3.5” optical properties and one for “Baum v2.0”. The values for “Baum v2.0” are on average about 50% higher than for “Baum v3.5”, but the regional distribution patterns are similar. Therefore intra-site comparisons are possible with considerably less dependence on the assumed ice particle shape. The shown maps highlight a distinct small scale variability, i.e. on the scale of few SEVIRI pixels. This variability cannot be resolved by ground measurements at few selected places. In the presented example the “Baum” parameterizations mark the extremes of the temporally and spatially averaged values and the HEY parameterizations lie in between (not shown here). There are few red pixels visible in the figure standing out from their environment. These are caused by unusually frequent cloud detections by COCS at these locations (see also Sect. 5.2.2).

Figure 4.12 emphasises that the lower DNI operation limit of a CST system has indeed strong influence on the average circumsolar radiation during operation. Both panels in the figure show the average cirrus related CSR for $\alpha_{\text{cir}} = 2.5^\circ$ and “Baum v3.5” during operation of a hypothetical power plant. However, they differ in the assumed operation limits: While in the left panel CSR is averaged over all time steps with $I_{\text{tot},\alpha=2.5^\circ} > 200 \text{ W/m}^2$, the CSR shown in the right panel is an average over all time steps with $I_{\text{tot},\alpha=2.5^\circ} > 100 \text{ W/m}^2$. The spatial patterns are similar, but the magnitude of the values for the 100 W/m^2 -threshold are considerably higher. The mean values averaged over the whole domain are 0.0164 and 0.0272, respectively. I.e. the change of the operation limit from 200 W/m^2 to 100 W/m^2 causes an average increase of 66% in the CSR. A change of the opening angle α_{cir} has less effect in this case: If we consider the same time steps as in the left panel ($I_{\text{tot},\alpha=2.5^\circ} > 200 \text{ W/m}^2$) but calculate the CSR for $\alpha_{\text{cir}} = 0.7^\circ$ and $\alpha_{\text{cir}} = 5.0^\circ$ the values

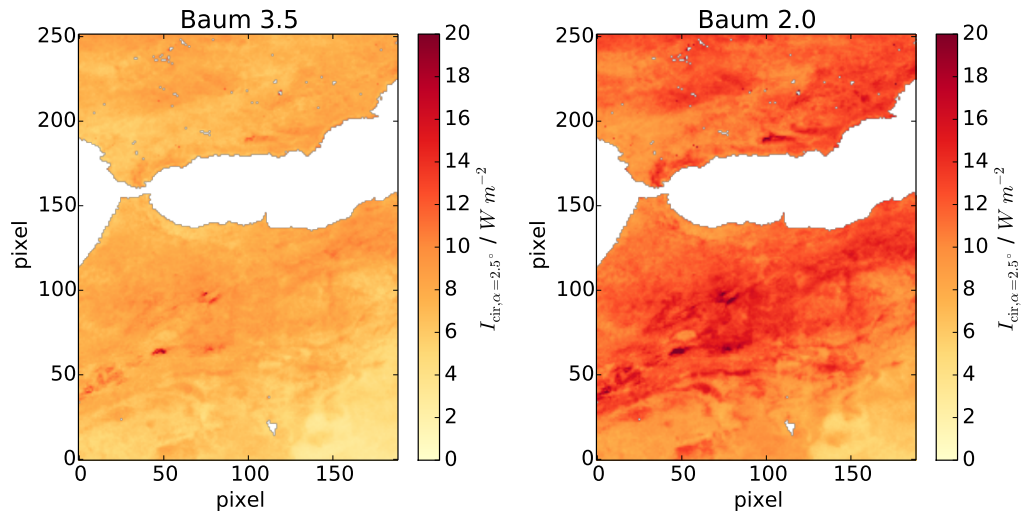


Figure 4.11: Circumsolar irradiance for a limiting angle of 2.5° , averaged over all time steps in the test dataset with $I_{\text{tot},\alpha=2.5^\circ} > 200 \text{ W/m}^2$ obtained using the “Baum v3.5” (left) and “Baum v2” (right) optical property datasets.

change moderately to 0.0113 and 0.0183, respectively. This corresponds to a change of -33% and +12% in regard to the value for $\alpha_{\text{cir}} = 2.5^\circ$ (compare also Fig. 3.19).

In this study evaluation of SEVIRI data was limited to a one year period for the sake of reduced computing time and storage space. Processing of longer time spans was not performed because the results would be most likely not directly applicable in a specific solar resource assessment process, which depends on the CST facility design. The presented results serve primarily as a proof of concept and may deviate from the long term mean. Still they allow to estimate the magnitude of the considered effects and give insight on the importance of the regional distribution. To obtain a rough estimate for the inter-annual variability of circumsolar irradiance due to cirrus clouds one can evaluate the variability of the cirrus cloud occurrence itself. To this end, I calculated the mean cirrus cloud cover within the test sector from the COCS cloud mask for six time spans of a full year’s length available (years 2006 to 2010 and the time span from May 2011 to Apr. 2012). The mean annual anomaly of the cirrus cloud cover derived from this data lies between 8% and 28%, depending on location, with a spatial average of 13%. The cirrus cloud cover for the time span May 2011 to Apr. 2012, for which circumsolar radiation was calculated, is on average 11% lower than the mean value for the six considered time periods. One can also contemplate the DNI variability: Lohmann et al. (2006) derived DNI from data of the

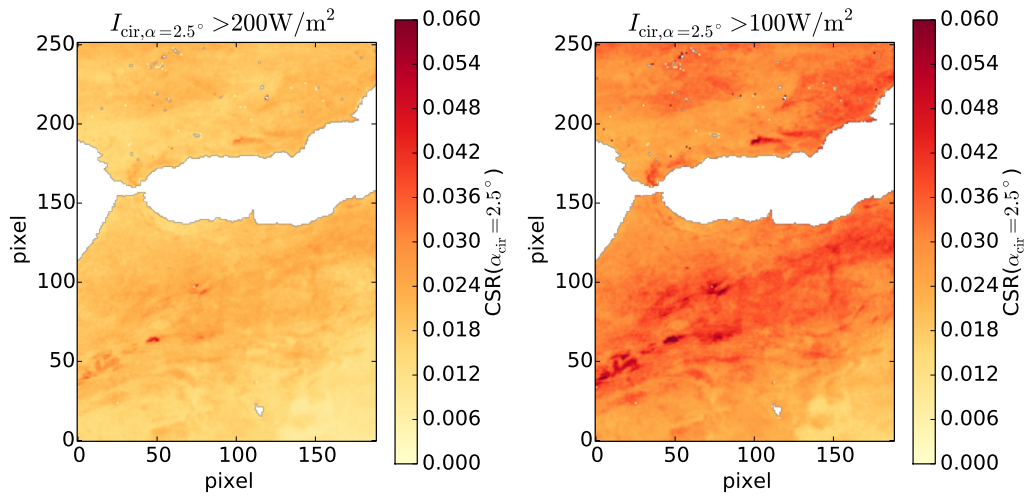


Figure 4.12: CSR for a limiting angle of 2.5° , averaged over all time steps in the test dataset with $I_{\text{tot}, \alpha=2.5^\circ} > 200 \text{ W/m}^2$ (left) and $I_{\text{tot}, \alpha=2.5^\circ} > 100 \text{ W/m}^2$, respectively, obtained using the “Baum v3.5” optical properties.

International Satellite Cloud Climatology Project (ISCCP). They reported annual standard deviations of DNI for selected places between between 5% and 13%. From measurements at the PSA Pozo-Vázquez et al. (2011) calculated an annual standard deviation of 6% for DNI and 9% for the cloud fraction. With these numbers in mind, a uncertainty in the range of 15% in the presented circumsolar radiation values in regard to the long-term mean through natural variability seems to be a reasonable first-order estimate.

4.3.2 Irradiance Overestimation by Pyrheliometers

In this section it is characterised how much the irradiation usable by a CST system deviates from the from pyrheliometer readings due to the cirrus related circumsolar radiation. At first, a coarse proxy for the operating hours of a hypothetical power plant was calculated, to estimate how much the solar resource is overestimated if irradiance is measured with a pyrheliometer exhibiting a larger aperture than a CST plant. The mean number of time steps at which $I_{\text{tot}, \alpha_{\text{cir}}} > 200 \text{ W/m}^2$ – i.e. at which the power plant could be operating – was computed for the test sector (Fig. 2.4) for $\alpha_{\text{cir}} = 2.5^\circ$ to represent a pyrheliometer and $\alpha_{\text{cir}} = 0.7^\circ$ to represent a power plant. Depending on the assumed ice particle shape this count is between 0.8% and 1.1% higher for the pyrheliometer compared to the power

plant.

Furthermore the mean overestimation of usable irradiation itself by a typical pyrheliometer due to cirrus clouds was calculated. To this end the irradiance integrated over calculated operating time E was compared. Consider the integrals

$$E_{0.7^\circ} = \int_{t_{0.7^\circ}} I_{\text{tot},\alpha_{\text{cir}}=0.7^\circ} dt \quad , \quad (4.8)$$

$$E_{2.5^\circ} = \int_{t_{2.5^\circ}} I_{\text{tot},\alpha_{\text{cir}}=2.5^\circ} dt \quad , \quad (4.9)$$

where $t_{0.7^\circ}$ and $t_{2.5^\circ}$ are all time steps with $I_{\text{tot},\alpha_{\text{cir}}=0.7^\circ} > 200 \text{ W/m}^2$ and $I_{\text{tot},\alpha_{\text{cir}}=2.5^\circ} > 200 \text{ W/m}^2$, respectively. The relative overestimation of usable irradiance is then calculated as

$$\Delta E = \frac{E_{2.5^\circ} - E_{0.7^\circ}}{E_{0.7^\circ}} \quad (4.10)$$

The mean values of ΔE averaged over all evaluated pixels within the test sector lie between 0.4% and 0.7%, depending on assumed cirrus optical properties. Figure 4.13 shows histograms of the (spatial) distribution of ΔE within the test sector (Fig. 2.4) for the optical property datasets “Baum v2” and “Baum v3.5”. From these one can assess that on one hand there can be considerable differences depending on location. E.g. considering the histogram for “Baum v2”, one can see that there are pixels for which the overestimation is calculated as low as 0.2%, but there are also others for which one must expect more than 1%. On the other hand, the values seem approximately normally distributed so that for most pixels the values cluster around a central value. To evaluate the sensitivity of the resource overestimation, ΔE was also calculated for two additional hypothetical CST systems. The first exhibits the same lower operation limit of 200 W/m^2 but a smaller acceptance angle $\alpha_{\text{cir}} = 0.5^\circ$. The second has the same acceptance angle of $\alpha_{\text{cir}} = 0.7^\circ$ but a changed lower operation limit of 100 W/m^2 . The average resource overestimation calculated with “Baum v2” is increased by 34% and 3%, respectively, due to these configuration changes in regard to the original value with $\alpha_{\text{cir}} = 0.7^\circ$ and a lower operation limit of 200 W/m^2 . In the presented example, the overestimation is clearly more sensitive to the CST system’s aperture size than to the lower operation limit. In the previous Sect. 4.3.1, however, average CSR values were calculated which proved to be sensitive to the lower operation limit. This highlights that a determination of which parameter is more important

cannot be made with universal validity.

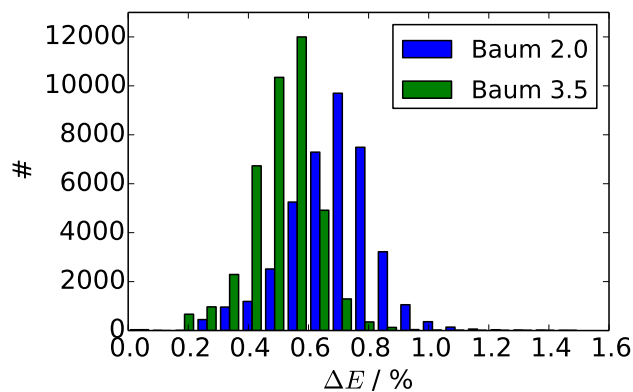


Figure 4.13: Histograms of the relative overestimation of usable irradiation ΔE due to cirrus clouds by a pyrliometer with $\alpha_{\text{cir}} = 2.5^\circ$ with regard to a hypothetical CST system with $\alpha_{\text{cir}} = 0.7^\circ$ and a lower operation limit of $I_{\text{tot},\alpha_{\text{cir}}=0.7^\circ} > 200 \text{ W/m}^2$. Blue: Values obtained utilizing the “Baum v2” cirrus optical properties. Green: Values obtained utilizing the “Baum v3.5” cirrus optical properties.

Altogether, ΔE values mostly below 1% are small compared to other uncertainties in the resource assessment process. For example, the long term mean value of the DNI could be deduced only with an uncertainty of approximately 3% from a 10-year-long series of perfect measurements, if one assumes an annual standard deviation of the DNI in the order of 10% (postulating a normal distribution of the annual DNI values). Standard deviations in this order are in line with reported values from Lohmann et al. (2006). In reality one will usually have to cope with shorter time series and/or additional measurement errors so that, depending on undertaken effort, deviations in the assessed DNI from the long-term average in the order of 5% can occur (pers. comm. Richard Meyer, 2013). However, it should be noted that the irradiance overestimation discussed in this section is no random uncertainty but a systematic error which should be accounted for. Without delving into economics, one should be aware of that the profit margin of a solar power plant can be strongly influenced by variations in power generation. This is because the expenses for construction, operation and maintenance are virtually independent from the produced power. Furthermore, the price per unit energy is often pre-determined by long-term power purchase agreements or feed-in tariffs (Meyer, 2013). The profit is usually small compared to the turnover and can basically be regarded as the turnover minus the expenses. Therefore any influence on

produced power has a leveraged effect on the profit. Following an estimate of Meyer et al. (2008) even a 0.5% bias in the usable irradiance may lead to profit differences between 100 000 € and 300 000 € p.a. considering a typical Spanish solar thermal power plant with 50 MW_e*. In general, the consideration of the resource overestimation becomes the more important the lower the overall uncertainty can be fixed.

4.3.3 Relation of Irradiance and CSR

If typical time series of CSR shall be generated for the simulation of CST plants, its frequency of occurrence must be linked to irradiance values. As there is no distinct dependence between irradiance and CSR, the statistics of both measures should be considered together. Figure 4.14 shows 2-dimensional histograms of irradiance and CSR obtained from the SEVIRI test data set (only measurements considered with a positive cirrus detection from COCS) and compares them to a histogram obtained from SAMS measurements (only measurements considered with a positive cloud detection by SAMS). The histograms need not necessarily be identical as the histograms for SEVIRI were computed for the whole test domain while the SAMS measurements were performed only at the PSA. Furthermore the cloud detection of SAMS is based basically on a threshold for the temporal variability of the measured optical thickness and therefore it is unlikely that all detections are due to cirrus clouds alone. The SAMS histogram exhibits a bifurcation for decreasing irradiance. The lower part cannot be accounted to cirrus clouds with optical properties as used in this study and is presumably caused by the aerosol contribution within falsely classified clear sky measurements. The histogram obtained for “Baum v3.5” matches the SAMS histogram better than the one for “Baum v2”. The latter shows a tendency to larger CSR values compared to “Baum v3.5”.

In Fig 4.15 similar histograms are depicted for three different fields of view. They highlight once more the dependence of circumsolar radiation of the field of view. Furthermore, the DNI-CSR-combinations for cirrus clouds simulated by Thomalla et al. (1983) are given in these plots to allow for a comparison. While in general they are within the range of values retrieved from the SEVIRI data, there is a notable difference for the field of view with $\alpha_{\text{cir}} = 0.5^\circ$. The high CSR values at around 800 W/m² irradiance cannot be reproduced with the cirrus optical properties considered in this study (Sect. 3.1).

*Capacity of 50 MW electric power generation

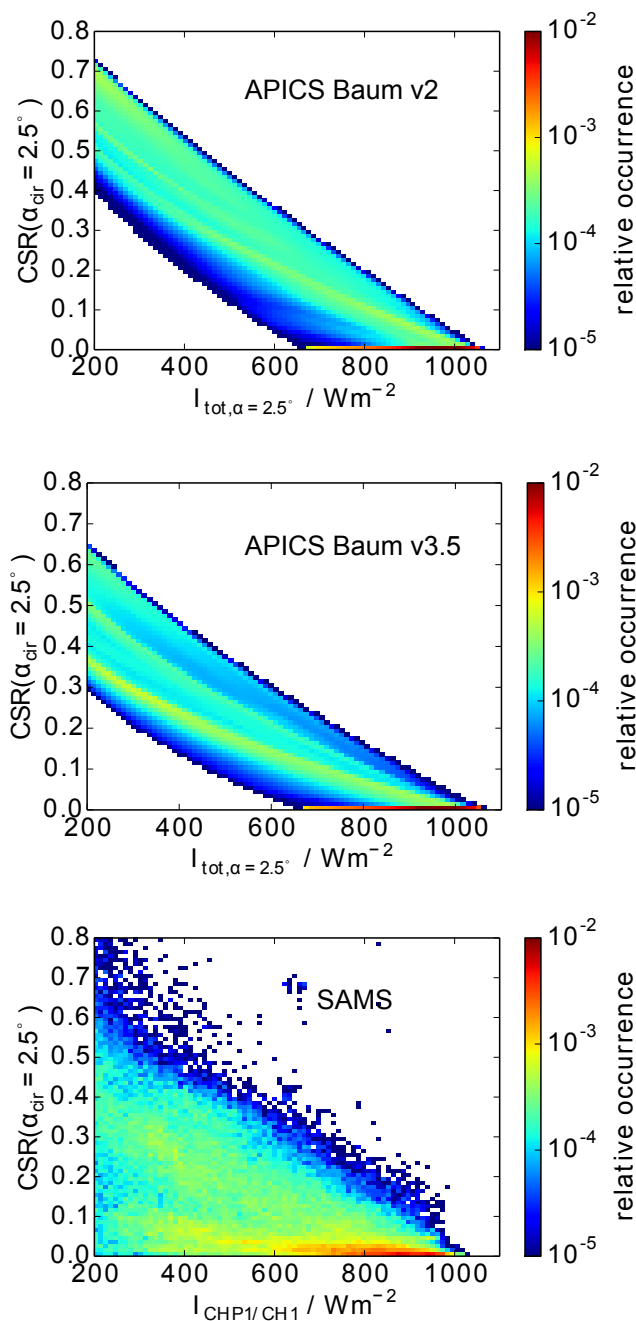


Figure 4.14: 2-dimensional histogram of the occurrence of $I_{\text{tot}, \alpha_{\text{cir}} = 2.5^\circ}$ and $CSR(\alpha_{\text{cir}} = 2.5^\circ)$ in case of cirrus clouds relative to the amount of all cirrus cloud measurements. Upper panel: Retrieved using “Baum v2” optical properties. Middle panel: Retrieved using “Baum v3.5” optical properties. Lower panel: Histogram from one year SAMS measurements (CloudPresenceVec=1). DNI measured with Kipp & Zonen CHP1/CH1.

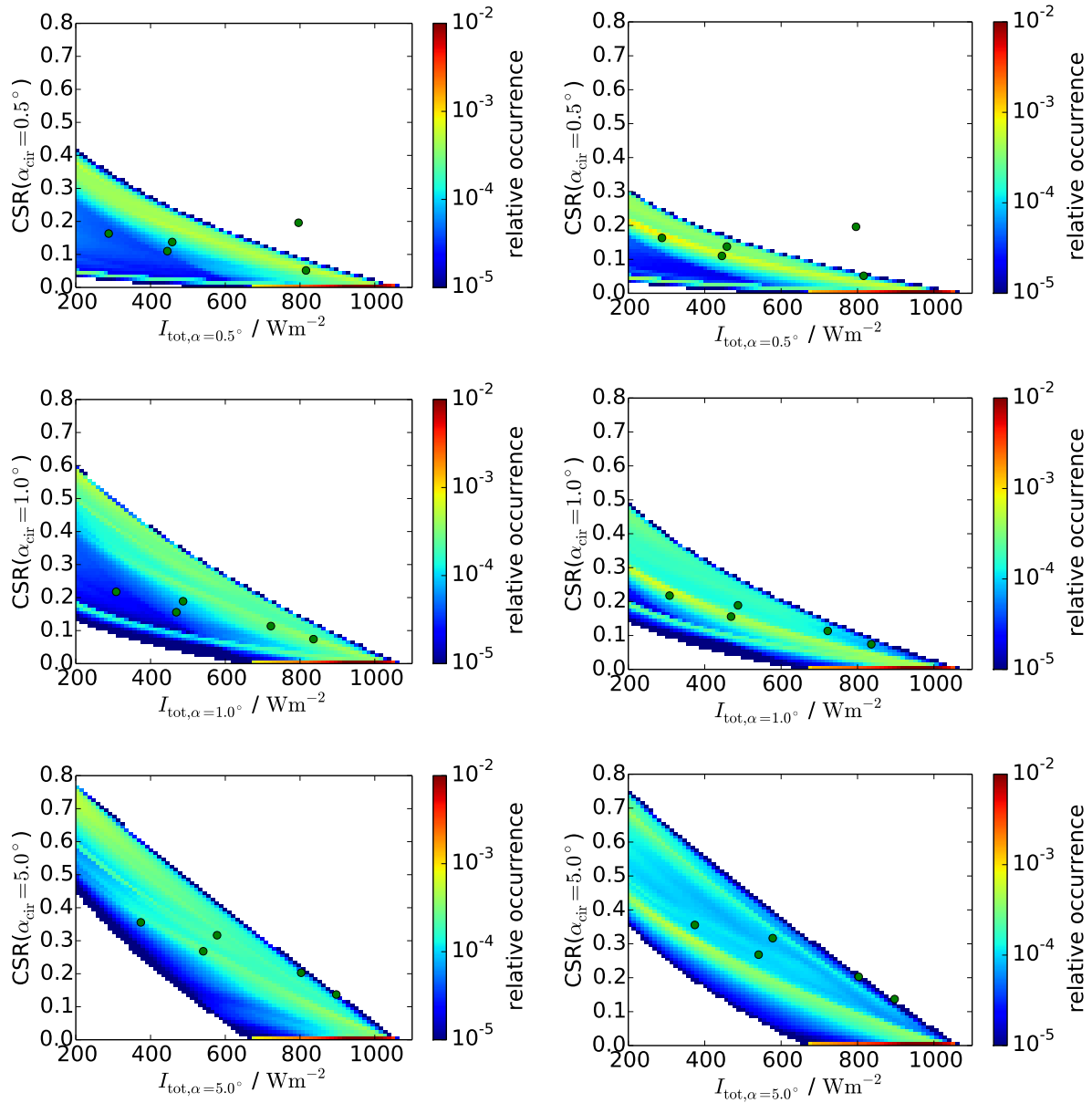


Figure 4.15: 2-dimensional histogram of the occurrence of $I_{\text{tot}, \alpha_{\text{cir}}}$ and $\text{CSR}(\alpha_{\text{cir}})$ in case of cirrus clouds relative to the amount of all cirrus cloud measurements. Green dots: Values from Thomalla et al. (1983, Tab. 2b) (simulations without aerosol). Left panels: “Baum v2”, Right panels: “Baum v3.5”, Upper panels: $\alpha_{\text{cir}} = 0.5^\circ$, Middle panels: $\alpha_{\text{cir}} = 1.0^\circ$, Lower panels: $\alpha_{\text{cir}} = 5.0^\circ$.

Chapter 5

Discussion

In this chapter the possibility of a statistical post-processing of IFS aerosol data is discussed (Sect. 5.1) as well as uncertainties in the cirrus cloud property retrieval (Sect. 5.2). In the last section the cirrus related CSR results obtained from MSG measurements are compared to a CSR parameterization from Neumann et al. (1998), which is based on DNI and GHI measurements.

5.1 Statistical Post-Processing of IFS Aerosol Output

In Sect. 4.2.1 it was pointed out that the aerosol related circumsolar radiation is strongly underestimated if IFS data are used head on, even for stable clear sky conditions. In this section it is investigated if a statistical post-processing can be used to obtain reasonable CSR values, though. This seemed promising, since it was already demonstrated that the model fulfills two important prerequisites for a successful retrieval of the circumsolar radiation: The model can predict the optical thickness (Bouarar et al., 2012) reasonably well and furthermore can distinguish between periods at which large particles are present or not (comp. Sect. 4.2.1). However, statistical post-processing comes at the cost of challenged universal validity because it depends on reference measurements. It was exercised with the measurements from the PSA and is not transferable one-to-one to other locations. A simple coefficient fit was exercised nevertheless to explore if the model could in principle serve in the retrieval of circumsolar radiation, specific tuning provided.

Originally the CSR is calculated with the adding method (see Sect. 3.5.2) as:

$$\text{CSR} = 1.0 - \exp \left[\sum_{i=1}^{N_{\text{aerosol components}}} -(\tau_{\text{app,sun},i} - \tau_{\text{app},\alpha,i}) \right] , \quad (5.1)$$

where $\tau_{\text{app,sun},i}$ and $\tau_{\text{app},\alpha,i}$ are the apparent optical thickness values for the i th aerosol component for a field of view enclosing the sun and for a field of view with the angular radius α for which the CSR shall be calculated, respectively (compare also Eqs. 3.15 & 3.21).

Under the assumption of linearity one can also treat the contributions of the individual aerosol components to the CSR separately (comp. Eq. 3.23):

$$\begin{aligned} \text{CSR} &= \sum_{i=1}^{N_{\text{aerosol components}}} \{1.0 - \exp [-(\tau_{\text{app,sun},i} - \tau_{\text{app},\alpha,i})]\} \\ &= \sum_{i=1}^{N_{\text{aerosol components}}} \text{CSR}_i . \end{aligned} \quad (5.2)$$

The linearity assumption holds true for the considered IFS data for the location of the PSA. The mean relative deviation between CSR calculated with Eq. (5.1) or with Eq. (5.2) is only 0.2%. Therefore the latter equation was used to enable the separation of the individual CSR-contributions.

In the post-processing step the CSR contributions of the individual aerosol types were weighted by time independent coefficients, so that the post-processed CSR is given as

$$\sum_{i=1}^{N_{\text{aerosol components}}} c_i \cdot \text{CSR}_i . \quad (5.3)$$

The coefficients were determined by minimizing the mean absolute deviation in CSR in regard to the SAMS measurements using a truncated Newton algorithm¹. It is an iterative minimizing procedure and does not necessarily always find the global minimum as it would be possible with an analytical linear least squares regression. For the purpose of this exemplary evaluation this drawback is however not crucial. In fact, the utilized numerical method is more flexible and contrasting the least squares method allows to use the mean absolute deviation as cost function.

¹Implemented in the Python software module `scipy.optimize.fmin_tnc` (SciPy 0.13)

Several setups of the fitting process were examined. The filtered validation dataset – containing the 1081 data tuples mentioned above in Sect. 4.2.1 – was always divided into a training set and an evaluation set by varying criteria. To ensure to have best possible data quality for the training, only measurements taken at $\theta_{\text{sun}} < 60^\circ$ were used in this example for the training.

If the coefficients for all aerosol components are fitted without constraints, the results are ambiguous: Depending on how the training and validation set is chosen, or how the first guess for the coefficients is made, the coefficients vary strongly, and sometimes extremely large or small values are the result. Interpreting this, one should be aware of that the contribution of most IFS aerosol components to the total CSR is negligible because they are comprised of particles with radii much smaller than $1\ \mu\text{m}$ and thus show no distinct forward scattering peak. The algorithm therefore fits the measured CSR with several time series of limited physical meaning, which may lead to the ambiguous results. The aerosol component indices and the corresponding mean contribution to the CSR at PSA are listed in Tab. 5.1. Furthermore some of the aerosol components are correlated which can cause ambiguity in the fit results as well. While virtually all coefficients depend strongly on the fitting setup, most of the tested setups have in common that they produce a coefficient c_3 (for the large dust component) between 40 and 60. In the end one can force all coefficients but c_3 to be 1 without increasing the fit residual considerably.

In the following, the result of one specific fit setup is presented as example. Data from the first nine days of each month were used for the training (191 data tuples) and data from the remaining days for the evaluation (823 data tuples). All coefficients but c_3 were constrained to be 1. The fitted coefficient c_3 in this case is 50.9, independent of the first guess. With this coefficient the validation measures computed for the 823 data tuples in the evaluation set improve considerably (comp. Tab. 5.2): The rank correlation is increased from 0.33 to 0.70, the MAD is reduced from 0.010 to 0.005 and the bias is reduced from -72% to -22%. The table also holds validation measures obtained by evaluating all 7972 data tuples originally considered (comp. Sect. 4.2.1) – including times with high temporal variability in the measured CSR. If the coefficient $c_3 = 50.9$ is applied on this data series, the validation measures improve as well. However the results are still rather poor with a bias of -49%, MAD of 0.013 and a rank correlation of 0.49. After the post-processing the CSR signal is mainly determined by the dust large and the sea salt medium component. Together they account for 81% of the CSR considering the evaluation dataset of 823 data tuples. Originally the CSR is dominated by the sea salt medium aerosol component alone.

If we again assume linearity, we can propagate the fit coefficients back and calculate the AOT contributions of the individual aerosol components after the fitting. To this end, one applies the same coefficients on the AOT as on the CSR. In the presented example the linearity assumption introduces an error of few percent only. As mentioned before, the largest particles are not necessarily accountable for large shares of the optical thickness. This is reflected in the total aerosol optical thickness after applying the fit. The mean AOT at 500 nm* for the period from 01 May. 2011 till 30 Apr. 2012 from the IFS data before fitting is 0.11 and 0.15 after fitting. Considering the bias in regard to the AERONET value (0.14) the fit also improves the AOT bias from -19% to +6%.

It was shown that a post-processing of the aerosol related CSR values can considerably improve the results. However the exercised fit cannot increase the temporal resolution of the model and thus not solve the problem with the sometimes high temporal variability of the CSR. Furthermore the underrepresentation of large dust particles in the IFS, as well as their importance, may vary with location. Therefore, the obtained results are not applicable one-to-one to other locations. It was demonstrated, however, that weather model output can in principle serve in the derivation of aerosol related circumsolar radiation, although, in regard to the IFS, improvements concerning the aerosol size distribution are necessary before the model output can be used unmodified. Future circumsolar radiation measurements at different places on the globe could help to validate and improve weather models in regard to large aerosol particles and/or to develop a more sophisticated time and location dependent post-processing.

5.2 Uncertainties in the Cirrus Cloud Property Retrieval

Considering the calculation of cirrus related circumsolar radiation the cloud property retrieval poses a considerable uncertainty. In the following Sect. 5.2.1 especially the effect of the utilized cirrus cloud mask on the calculated circumsolar radiation is discussed. In Sect. 5.2.2 the reasons for spurious cloud property retrieval results at some pixels are investigated.

*Utilising 500 nm here as the closest wavelength to 550 nm supported by the AERONET sun photometer at the PSA.

Table 5.1: Mean contribution to the CSR and AOT(500 nm) values of the individual aerosol components for Almería derived from IFS data for the 823 data tuples of the filtered evaluation dataset before fitting.

| i | Aerosol Component | CSR orig. | AOT orig. |
|----|----------------------------|-----------|-----------|
| 1 | Dust small | 8.2e-4 | 7.6e-2 |
| 2 | Dust medium | 2.2e-4 | 8.1e-3 |
| 3 | Dust large | 1.4e-4 | 1.4e-3 |
| 4 | Black carbon hydrophilic | 1.1e-6 | 3.5e-4 |
| 5 | Black carbon hydrophobic | 2.3e-5 | 7.3e-3 |
| 6 | Organic carbon hydrophilic | 4.1e-6 | 6.7e-4 |
| 7 | Organic carbon hydrophobic | 9.8e-5 | 1.6e-2 |
| 8 | Sea salt small | 1.2e-4 | 1.0e-2 |
| 9 | Sea salt medium | 1.9e-3 | 5.7e-3 |
| 10 | Sea salt large | 6.0e-4 | 7.3e-4 |
| 11 | Sulfate | 2.7e-4 | 3.7e-2 |
| | Total | 4.2e-3 | 0.164 |

Table 5.2: Validation measures computed for CSR as originally derived from IFS output and for the fitted CSR time series with coefficient $c_3 = 50.9$.

| | | $r_{\text{rank,CSR}}$ | r_{CSR} | MAD | Bias | N |
|-----------------------------|-------------------|-----------------------|------------------|-------|------|------|
| IFS original | stable conditions | 0.33 | 0.41 | 0.010 | -72% | 823 |
| IFS fitted ($c_3 = 50.9$) | stable conditions | 0.70 | 0.75 | 0.005 | -22% | 823 |
| IFS original | all data | 0.25 | 0.17 | 0.015 | -73% | 7972 |
| IFS fitted ($c_3 = 50.9$) | all data | 0.49 | 0.28 | 0.013 | -49% | 7972 |

5.2.1 Undetected Cirrus Clouds

As mentioned the APICS cloud property retrieval is only applied to pixels contained in a cirrus cloud mask. In this section it is discussed how sensitive the circumsolar radiation results are to the implemented change in the APICS cirrus cloud mask from MeCiDa to COCS.

The detection efficiency of COCS is only better than MeCiDa's for thin cirrus clouds (Kox, 2012). Therefore, the total ice cloud cover (ICC), considering all evaluated SEVIRI measurements in the test sector (May 2011 – Apr. 2012, $\theta_{\text{sun}} < 80^\circ$), increases only moderately from 17.4% to 22.2%, i.e. by 28%, when changing from MeCiDa to COCS (see Tab. 5.3). However, if looking at measurements with a total irradiance $I_{\text{tot},\alpha_{\text{cir}}=2.5^\circ}$ larger than 200 W/m^2 alone, the ICC determined by COCS is about 70%-80% larger than

Table 5.3: Determined ice cloud cover (ICC) for different setups of APICS. The first column gives the total ice cloud cover. The second column holds the relative amount of pixels classified as cirrus with $I_{\text{tot}} > 200 \text{ W/m}^2$ ($= N_{\text{cirrus},200 \text{ W/m}^2}$) on the evaluated slots ($= N_{\text{tot}}$) and the last column provides the relative amount of pixels classified as cirrus with $I_{\text{tot}} > 200 \text{ W/m}^2$ on all slots with $I_{\text{tot}} > 200 \text{ W/m}^2$ ($= N_{200 \text{ W/m}^2}$). Irradiance values were calculated for $\alpha_{\text{cir}} = 2.5^\circ$.

| APICS Setup | ICC | $N_{\text{cirrus},200 \text{ W/m}^2}/N_{\text{tot}}$ | $N_{\text{cirrus},200 \text{ W/m}^2}/N_{200 \text{ W/m}^2}$ |
|-------------------|-------|--|---|
| MeCiDa, Baum v2.0 | 17.4% | 6.5% | 8.8% |
| COCS, Baum v2.0 | 22.2% | 10.6% | 14.0% |
| MeCiDa, Baum v3.5 | 17.4% | 5.8% | 7.9% |
| COCS, Baum v3.5 | 22.2% | 9.9% | 13.2% |

Table 5.4: Mean circumsolar irradiance and mean CSR in case of cirrus clouds for different setups of APICS. All values were calculated for $\alpha_{\text{cir}} = 2.5^\circ$.

| APICS Setup | $I_{\text{cir}}(I_{\text{tot}} > 200 \text{ W/m}^2)$ | CSR for cirrus with ($I_{\text{tot}} > 200 \text{ W/m}^2$) |
|-------------------|--|--|
| MeCiDa, Baum v2.0 | 5.4 W/m ² | 0.24 |
| COCS, Baum v2.0 | 7.8 W/m ² | 0.20 |
| MeCiDa, Baum v3.5 | 3.7 W/m ² | 0.19 |
| COCS, Baum v3.5 | 5.3 W/m ² | 0.15 |

the one from MeCiDa. The exact number depends on the considered ice particle shape parameterization because it influences the calculation of I_{tot} . In terms of mean circumsolar irradiance this results in an increase of 40%-50% (considering an α_{cir} of 2.5° , see Tab. 5.4). When MeCiDa is used, fewer thin clouds are detected, but the amount of thick clouds remains basically unchanged. Therefore, the mean CSR in case of cirrus clouds decreases in the order of 15% to 20% when changing from MeCiDa to COCS. Figure 5.1 shows histograms of the CSR occurrence for the four setups of APICS as listed in Tab. 5.4 – that is for the possible combinations of the COCS and MeCiDa cloud mask and the “Baum v2” and “Baum v3.5” optical properties. The curves converge at large CSR values if different cloud masks but the same cirrus optical properties are used. This confirms that the cirrus detection schemes only differ for optically thin cirrus clouds. The discussed examples highlight the importance of detecting and retrieving thin cirrus clouds at the best.

Even COCS does not detect all cirrus clouds, although it shows increased performance

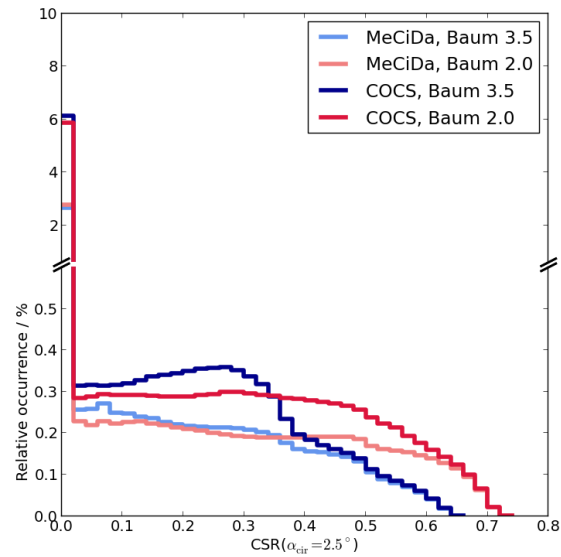


Figure 5.1: Histograms of the relative occurrence of CSR values due to cirrus clouds under the condition $I_{\text{tot},\alpha=2.5} > 200\text{W}/\text{m}^2$ with respect to the total number of SEVIRI measurements with $I_{\text{tot},\alpha=2.5} > 200\text{W}/\text{m}^2$ for one year within the test sector considering the two ice particle shape parameterizations "Baum v2.0" and "Baum v3.5" as well as the two different cirrus cloud detection algorithms MeCiDa and COCS.

compared to MeCiDa. In the following it is estimated how large the impact of the missed cirrus clouds is in terms of circumsolar radiation. Bugliaro et al. (2012, Fig. 25.5 b) gave the detection efficiency values η_{det} for COCS and MeCiDa as step functions. For simplicity they are approximated here as

$$\eta_{\text{det,MeCiDa}}(\tau) = \begin{cases} 0.125 + 1.458 \cdot \tau, & \text{for } \tau < 0.6 \\ 1, & \text{else} \end{cases} \quad (5.4)$$

$$\eta_{\text{det,COCS}}(\tau) = \begin{cases} 0.375 + 2.083 \cdot \tau, & \text{for } \tau < 0.3 \\ 1, & \text{else} \end{cases} \quad (5.5)$$

Figure 5.2 displays the approximated detection efficiencies. For each detected cloud, whose optical thickness is retrieved by APICS, a correction factor for the occurrence can be defined:

$$f_{\text{cor}}(\tau) = \frac{1}{\eta_{\text{det}}(\tau)} \quad . \quad (5.6)$$

For example, if for a cloudy SEVIRI pixel $f_{\text{cor}} = 2$ is identified, it is likely that there is another pixel containing a cirrus with the same optical thickness τ that stays undetected. Therefore, if computing an occurrence histogram, one can determine the average correction factor for each histogram bin which allows to transform the real histogram by multiplication by f_{cor} into a new histogram corrected for the missed cloud detections. This is shown in Fig. 5.3 where CSR histograms are displayed similar to Fig. 5.1 but also a version corrected for the missed cloud detections (note that only SEVIRI measurements for the month May 2011 are the basis for Fig. 5.3). Furthermore a histogram is shown that was obtained by treating all SEVIRI pixels as cirrus cloudy and processing them through the cloud property retrieval. This will of course produce a lot of wrong values as water clouds, or even clear sky measurements deviating from the APICS a priori assumptions will thereby produce an ice optical thickness. However, this curve is shown as it poses the upper limit for the histogram.

Interestingly the histogram correction mainly affects CSR values smaller than 0.2 for MeCiDa and smaller than 0.1 for COCS. It can therefore not correct the discrepancy between COCS and MeCiDa at higher CSR values. This, however, can be alleviated if the maximum detection efficiency of MeCiDa is assumed to be 0.8 (histogram not shown). This suggests that either MeCiDa reaches its full detection efficiency only at optical thickness values considerably larger than 0.6 (comp. Eq. 5.5) or that COCS produces a considerable amount of false alarms. However as mentioned earlier, Kox (2012) found a false alarm

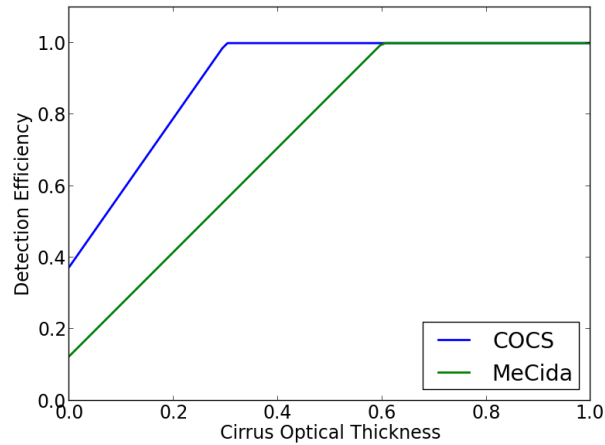


Figure 5.2: Cirrus detection efficiency for COCS and MeCiDa (approximating the step function from Bugliaro et al., 2012, Fig. 25.5 (b)).

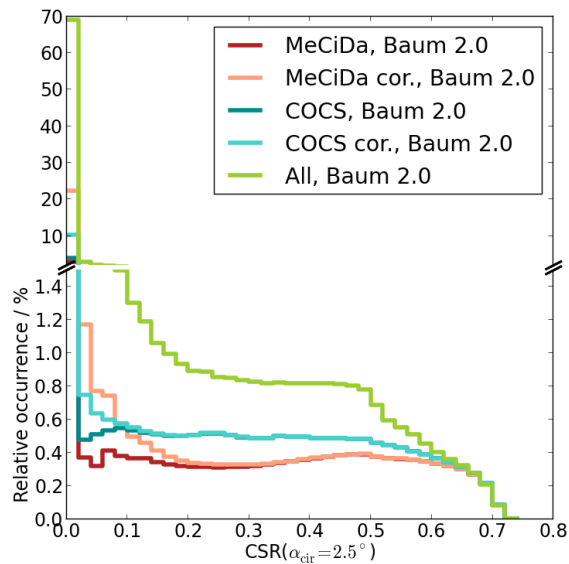


Figure 5.3: Histograms of the relative occurrence of CSR values due to cirrus clouds under the condition $I_{\text{tot},\alpha=2.5} > 200\text{W/m}^2$ with respect to the total number of SEVIRI measurements with $I_{\text{tot},\alpha=2.5} > 200\text{W/m}^2$ for May 2011 within the test sector considering the ice particle shape parameterization "Baum v2.0" as well as the cirrus cloud detection algorithms MeCiDa and COCS. The light colored lines show the results corrected for decreasing cloud detection efficiency at lower optical thickness. The yellow curve was obtained by assuming all SEVIRI pixels as cirrus cloud covered.

rate of only approximately 5% for COCS using CALIOP spaceborne LIDAR observations as reference, which makes the former point more likely. Also the data basis for $\tau > 0.6$ from the LIDAR measurements evaluated by Bugliaro et al. (2012) is rather small so that a concluding answer considering the detection efficiency at $\tau > 0.6$ cannot be given. In general it should be noted that Bugliaro et al. (2012) could rely only on about 450 data points to calculate the detection efficiency distributions so that a considerable uncertainty must be expected. It must also be noted that the histogram correction does not consider the ice and water cloud cover in a specific scene. For example, if the ice cloud cover in a hypothetical scene was 100%, f_{cor} could still be larger than one which is unphysical. Still, for a coarse estimate this method seems appropriate because the shown histograms are calculated utilizing many different scenes.

Figure 5.4 shows the detection efficiency correction applied to histograms of circumsolar irradiance ($\alpha_{\text{cir}} = 2.5^\circ$). The correction for MeCiDa affects I_{cir} values smaller than approximately 100 W/m^2 and the correction for COCS values smaller than approximately 75 W/m^2 . Again at higher values the discrepancy between COCS and MeCiDa stays unchanged.

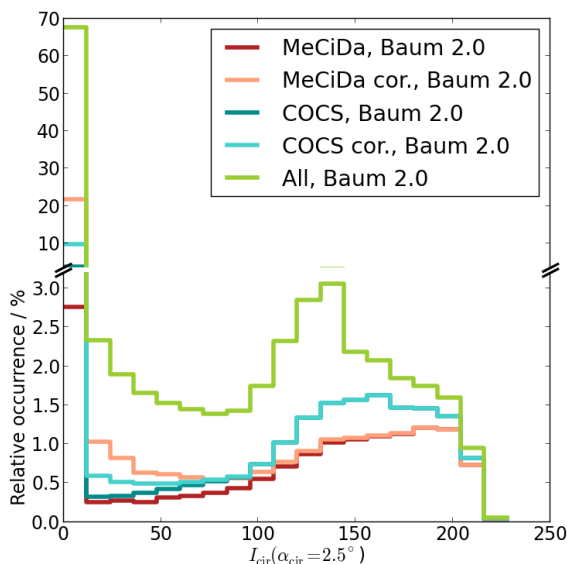


Figure 5.4: Same as Fig. 5.3 but here the occurrence of circumsolar irradiance values is displayed instead of occurrence of CSR values.

Concluding, it can be said that the variation of the curves in Figs. 5.3 & 5.4 (except for the

light green curves) depict the uncertainties remaining from the imperfect cloud detection algorithms.

5.2.2 Spurious SEVIRI Pixels

There are some pixels in the SEVIRI image for which the average retrieved CSR values are exceptionally high or low compared to the neighbouring pixels (comp. figures in Sect. 4.3). This is because they show an exceptionally high or low amount of cloud detections. Two reasons for this have been diagnosed. First, there are some pixels for which the COCS algorithm spuriously diagnoses almost always clouds. Second, there are some pixels for which often no albedo could be unraveled from the EUMETSAT Clear Sky Map (comp. Sect. 3.2.2). This is because the Clear Sky Map often contains negative reflectivity values for these pixels. In such case the APICS retrieval fails. In the processing of the satellite measurements, the SEVIRI images were filtered through a land-water mask from the LANDSAF¹. Ocean pixels as well as continental pixels containing a considerable amount of water are therefore masked. The reason for the negative values in the Clear Sky Map is not entirely clear, but most pixels for which negative values occur are near spots that contain water surfaces according to the LANDSAF land-water-mask. Possibly the land-water mask does not always capture the full extent of the water surfaces. However the number of spurious pixels is low and does not put the derived results into question.

5.3 Comparison of the Satellite CSR Retrieval to a Regression Model

Neumann et al. (1998) parameterized the CSR as a function of the DNI/GHI ratio, because they found that CSR cannot reasonably be parameterized from DNI alone. Combined DNI and GHI measurements are taken at many sites so that their parameterization could in principle help to alleviate the lack of CSR measurements. They published empirical fits to their measurements of circumsolar radiation performed at the PSA and in Cologne. For the PSA they parameterized the CSR in percent as

$$\text{CSR} = 70 - 65.948 \cdot \frac{\text{DNI}}{\text{GHI}} \cdot \frac{(90^\circ - \theta_{\text{sun}})^{0.669}}{15.822} \quad , \quad (5.7)$$

¹Land Surface Analysis Satellite Applications Facility.

where the right most term normalizes the DNI/GHI ratio to empirically determined clear sky conditions.

The SAMS dataset also contains DNI and GHI measured at the nearby meteorological station as additional data. Therefore one can compare the fit (Eq. 5.7) to satellite retrieved as well as to directly measured CSR. To allow for this comparison, CSR values for the PSA calculated with Eq. (5.7) were re-gridded to the 15 min-interval of SEVIRI in the same way like the SAMS measurements, as described in Sect. 4.2.2. The validation measures listed in Tab. 5.5 indicate that the DNI/GHI-fitting method has advantages compared to the satellite retrieval developed in this study if instantaneous CSR values shall be derived: They show higher correlation and a lower mean absolute deviation when compared to the SAMS values than the satellite derived values. This can be attributed to the fact that DNI and GHI were measured at the same place as the CSR, and therefore all collocation errors are removed, which need to be considered for SEVIRI measurements, though. The statistical distribution of CSR, however, is better captured by the satellite retrieval. This becomes obvious from the bias (Tab. 5.5): While the mean value from the DNI/GHI parameterization is 50% off, the satellite derived values only show an underestimation of 11%. Furthermore the histogram for the satellite retrieval resembles the one for the SAMS measurements considerably better than the one for the DNI/GHI-fit which can be followed in Fig. 5.5. Therefore, I conclude that the, compared to the DNI/GHI-parameterization, elaborate process of deriving the circumsolar radiation is rewarded with advantages in the characterisation of the circumsolar radiation.

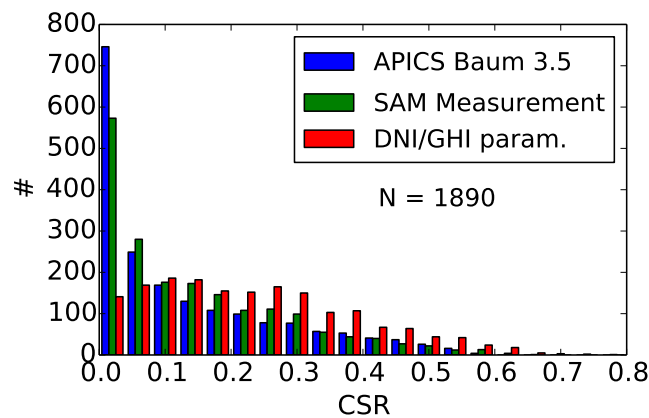


Figure 5.5: Histograms of CSR measured by SAMS and retrieved from SEVIRI (just as in Fig. 4.8), as well as parameterized according to Eq. 5.7 (red).

Table 5.5: Comparison of CSR retrieved from SEVIRI and obtained from the DNI/GHI-fit (Eq. 5.7) to values measured by SAMS: Rank correlation $r_{\text{rank,CSR}}$, Pearson correlation r_{CSR} , mean absolute deviation MAD, bias and the number of compared data tuples N .

| Optical Properties | $r_{\text{rank,CSR}}$ | r_{CSR} | MAD | Bias | N |
|--------------------|-----------------------|------------------|------|------|------|
| APICS, Baum v3.5 | 0.48 | 0.44 | 0.11 | -11% | 1890 |
| DNI/GHI-fit | 0.86 | 0.86 | 0.09 | 50% | 1890 |

It should be mentioned that Neumann et al. (1998) measured the DNI with an Eppley Normal Incidence Pyrheliometer (NIP) which has a slightly larger field of view than the Kipp & Zonen CH1/CHP1 that was used to measure the DNI values included in the SAMS dataset. Also the CSR refers to a slightly different α_{cir} . Therefore, a fit formula derived from the SAMS dataset would probably possess slightly different coefficients. This could explain the bias (Tab 5.5) to some extent, but not the deviations in the histogram: Histograms for SAMS and SEVIRI have also been calculated for slightly larger field of views. They are not shown here because they look similar to the one in Fig. 5.5.

Chapter 6

Conclusions

In this study a novel method to determine circumsolar radiation from data on cirrus clouds and aerosol was developed. The specific data sets used in the study are cirrus cloud properties retrieved from MSG measurements and modelled aerosol data from ECMWF's IFS. Several components were linked together and improved where necessary to develop the method. The Monte Carlo radiative transfer model MYSTIC was extended by introducing a sun disk instead of a point source such that it can simulate the circumsolar region with high accuracy. Furthermore, optical property data sets for the aerosol components as simulated in the IFS were generated to enable radiative transfer simulations specifically in regard to the IFS model output. With these tools at hand, it was possible to establish a database of coefficients which allow the fast computation of circumsolar radiation by simple analytical expressions from cloud or aerosol properties instead of performing time consuming radiative transfer simulations.

While the IFS aerosol data could be processed through the circumsolar radiation parameterization as they were, the required cloud properties first had to be retrieved from the MSG measurements. To obtain the required parameters cloud particle effective radius and cloud optical thickness the APICS retrieval framework was employed. The success rate of APICS was optimized by improving an important a priori assumption for the cloud property retrieval – the reflectivity of the ground. A ground albedo dataset which is consistent with the other a priori assumptions made in the cloud property retrieval algorithm was created. It replaces the formerly used MODIS datasets. The APICS retrieval requires a cirrus cloud mask to select which satellite pixels are processed. The within this study introduced use of a cirrus cloud mask based on the COCS algorithm allows to consider

more optically thin clouds in the retrieval than originally possible with the MeCiDa cloud mask. This increases the retrieved circumsolar irradiance on average by some 40% to 50%. APICS was also extended with new lookup tables for individual ice particle shapes and the “Baum v3.5” ice particle mixture to allow for an uncertainty analysis concerning the particle shape.

6.1 Synopsis of Findings

Considering cirrus related circumsolar radiation, the uncertainties in the complete retrieval chain due to necessary assumptions of the ice particle shape have been assessed to be large. On average, the circumsolar irradiance derived relying on the “Baum v2” ice particle parameterization is some 50% larger than the one obtained using “Baum v3.5”. However, the spatial distributions show similar patterns. The evaluated satellite data revealed that the circumsolar radiation exhibits a considerable variability on the scale of a few SEVIRI pixels which cannot be captured by ground measurements at few selected places. Despite the mentioned differences between the two state-of-the-art ice particle parameterizations, a validation of retrieved CSR values with ground measurements performed at the PSA, Spain, showed good agreement for both ice particle mixtures. For this location the results obtained using the “Baum” parameterizations differ only by some 15% to 25% regarding the mean of the CSR, depending on choice of the considered time span. A specification of the best particle mixture parameterization is ambiguous since none optimizes all validation measures. Considering the complete evaluated time series, the CSR derived using “Baum v2” exhibits a slightly smaller bias (4%) compared to the one obtained using “Baum v3.5” (-11%). The mean absolute deviation is 0.11 for both variants. The performance of the satellite retrieval of cirrus related CSR was also compared to a CSR parameterization from Neumann et al. (1998) which uses ordinary DNI and GHI measurements as they are collected at many sites: The satellite retrieved values show considerably less bias and a histogram that much better resembles the SAMS measurements. The parameterization from Neumann et al. (1998) correlates better with the SAMS measurements, though. This comes to no surprise as the utilized DNI/GHI measurements were taken directly next to the SAMS location so that no collocation errors can occur. Besides the determination of spatially resolved circumsolar radiation characteristics, the developed method also allows to calculate the overestimation of exploitable irradiation by a pyrheliometer due to cirrus clouds. To provide an example, this was exercised for a hypothetical power plant exhibiting

a lower operation limit of 200 W/m^2 and an opening half-angle of 0.7° . An average overestimation of the solar resource in the order of 0.5% due to cirrus clouds alone was found, with the exact values depending on location. In the context of the overall uncertainties in the resource assessment which can be in the order of 5% this may seem small. Yet, these small values in the order of 0.5% translate into a profit overestimation of several hundred thousand Euro per year for a typical 50 MW_e solar thermal plant. At locations with stable insolation conditions it is achievable to determine the long term solar resource with uncertainties as low as 3%, at the same time there are some spots for which overestimations of over 1% were retrieved in this thesis. Therefore in some cases a 1% bias could face a 3% random error. Consideration of the circumsolar radiation could therefore improve the resource assessment considerably in such cases.

Concerning the aerosol related CSR, a strong underestimation by the method was diagnosed. Most likely this is mainly caused by an underrepresentation of large dust particles ($r \gtrsim 1 \mu\text{m}$) in the IFS. Furthermore, circumsolar radiation fluctuations on the time scale of minutes were found – even during clear sky conditions. These cannot be reproduced with the current model resolution of the IFS. However, an a posteriori adjustment of the contribution of large dust particles to the CSR improves all validation measures considerably. On one hand this challenges the applicability of the model results at other locations than the PSA for the time being because the necessary adjustment may vary with location. On the other hand it shows that the model has some skill in predicting the course of the aerosol concentrations, including large particles, as the adjustment comprises only a static bias correction for the large dust component.

6.2 Outlook

Despite obvious uncertainties, a retrieval of cirrus related circumsolar radiation from meteorological satellite observations can complement ground measurements since it offers several unique advantages: Compared to ground measurements it is cheap. Satellite data are also readily available for many regions of the world for longer time spans than any of the so far available time series of ground measurements. Furthermore, the method allows to easily compare the circumsolar radiation characteristics of arbitrary sites as long as they are within the field of view of the same satellite. The diagnosed small scale spatial variability highlights that ground-based measurements of circumsolar radiation at a few sites alone

are not sufficient for a global characterisation. The further development of satellite based cloud property retrievals can improve the circumsolar radiation products since the errors in the retrieved cloud properties are a main source of uncertainty in circumsolar radiation. In particular, information about the ice particle shape composition would help to reduce the uncertainty. A manual screening of a subset of the validation data series considerably improved the mean absolute deviation and correlation (MAD 0.07 instead of 0.09, r_{rank} 0.76 instead of 0.65, “Baum v3.5”) which indicates that the presence of sub-scale water clouds below or besides the cirrus compromises the satellite retrieved results. A detection and appropriate treatment of “mixed cloud” pixels is therefore another open point for further development.

The presented parameterization with its efficient lookup table approach can in principle be extended and applied to other data sources as well. Regional aerosol models, for example, with higher temporal and spatial resolution could help to overcome the current limitations of the IFS. To this end an optical properties according to the new data source would be required so that expanded k -tables can be calculated.

Bibliography

- G. B. Airy. *Transactions of the Cambridge Philosophical Society*, volume 5, chapter On the Diffraction of an Object-glass with Circular Aperture, pages 283–291. 1835.
- B. A. Baum, P. Yang, Andrew J. Heymsfield, Carl G. Schmitt, Yu Xie, Aaron Bansemer, Yong-Xiang Hu, and Zhibo Zhang. Improvements in Shortwave Bulk Scattering and Absorption Models for the Remote Sensing of Ice Clouds. *Journal of Applied Meteorology and Climatology*, 50:1037–1056, 2011. doi: 10.1175/2010JAMC2608.1.
- B.A. Baum, A.J. Heymsfield, P. Yang, and S.T. Bedka. Bulk Scattering Models for the Remote Sensing of Ice Clouds. Part 1: Microphysical Data and Models. *Journal Of Applied Meteorology*, 44:1885–1895, 2005a.
- B.A. Baum, P. Yang, A.J. Heymsfield, S. Platnick, M. D. King, Y. X. Hu, and S.T. Bedka. Bulk Scattering Models for the Remote Sensing of Ice Clouds. Part 2: Narrowband Models. *Journal Of Applied Meteorology*, 44:1896–1911, 2005b.
- A. Benedictow, A.M. Blechschmidt, I. Bouarar, E. Cuevas, H. Clark, J. Griesfeller, V. Huijnen, N. Huneus, L. Jones, J. Kapsomenakis, S. Kinne, K. Lefever, M. Razinger, A. Richter, M. Schulz, W. Thomas, V. Thouret, M. Vrekoussis, A. Wagner, and C. Zerefos. *Validation Report of the MACC Reanalysis of Global Atmospheric Composition: Period 2003-2010*. KNMI, De Bilt, the Netherlands, 2012.
- P. Blanc. International Solar Energy Society Webinar: Improving DNI Information for CSP Development, 2013. URL http://www.ises-online.de/fileadmin/user_upload/PDF/ISES-Webinar-DNI-May2013-MINES_ParisTech-Ed1.5.pdf. 29 May 2013, last accessed 24 Jun 2013.
- Max Born and Emil Wolf. *Principles of Optics : Electromagnetic Theory of Propagation, Interference and Diffraction of Light*. Cambridge Univ. Press, Cambridge, 7. (expanded) edition, 1999. ISBN 978-0-521-64222-4.
- I. Bouarar, H. Clark, H. Flentje, V. Huijnen, L. Jones, J. Griesfeller, N. Huneus, J. Kapsomenakis, S. Kinne, E. Katragkou, K. Lefever, M. Razinger, A. Richter, A.M. Blechschmidt, M. Schulz, A. Benedictow, W. Thomas, V. Thouret, M. Vrekoussis, A. Wagner, and C. Zerefos. *Validation Report of the MACC Near Real Time Global*

Atmospheric Composition Service, System Evolution and Performance Statistics, Status to March 2012. KNMI, De Bilt, the Netherlands, 2012.

L. Bugliaro, T. Zinner, C. Keil, B. Mayer, R. Hollmann, M. Reuter, and W. Thomas. Validation of Cloud Property Retrievals with Simulated Satellite Radiances: A Case Study for SEVIRI. *Atmos. Chem. Phys.*, 11(12):5603–5624, 2011. doi: 10.5194/acp-11-5603-2011.

Luca Bugliaro, Hermann Mannstein, and Stephan Kox. Ice Cloud Properties from Space. In Ulrich Schumann, editor, *Atmospheric Physics: Background - Methods - Trends*, pages 417–432. Springer-Verlag, Berlin, 2012.

Luca Bugliaro, Andreas Ostler, Martin Wirth, Claudia Emde, and Ulrich Schumann. Validation of Cirrus Detection and Cirrus Optical Thickness Derived from MSG/SEVIRI with an Airborne High Spectral Resolution Lidar. In preparation for *Atmos. Meas. Tech.*, 2013.

D. Buie and A.G. Monger. The Effect of Circumsolar Radiation on a Solar Concentrating System. *Solar Energy*, 76:181–185, 2004.

D. Buie, A.G. Monger, and C.J. Dey. Sunshape Distributions for Terrestrial Solar Simulations. *Solar Energy*, 74:113–122, 2003. doi: 10.1016/S0038-092X(03)00125-7.

R. Buras and B. Mayer. Efficient Unbiased Variance Reduction Techniques for Monte Carlo Simulations of Radiative Transfer in Cloudy Atmospheres: The Solution. *Journal of Quantitative Spectroscopy and Radiative Transfer*, 112:434–447, 2011. doi: 10.1016/j.jqsrt.2010.10.005.

R. Buras, T. Dowling, and C. Emde. New Secondary-Scattering Correction in DISORT with Increased Efficiency for Forward Scattering. *J. Quant. Spectrosc. Radiat. Transfer*, 112:2028–2034, 2011.

Julio Chaves. *Introduction to Nonimaging Optics*. CRC Press, Boca Raton, 2008.

CIMO Guide. Guide to Meteorological Instruments and Methods of Observation, 7th edition. Technical report, World Meteorological Organization, 2008.

J. G. DeVore, A. T. Stair, A. LePage, D. Rall, J. Atkinson, D. Villanucci, S. A. Rappaport, P. C. Joss, and R. A. McClatchey. Retrieving Properties of Thin Clouds from Solar Aureole Measurements. *J. Atmos. Oceanic Technol.*, 26:2531–2548, 2009. doi: 10.1175/2009JTECHA1289.1.

J. G. DeVore, J. A. Kristl, and S. A. Rappaport. Retrieving Cirrus Microphysical Properties from Stellar Aureoles. *Journal of Geophysical Research: Atmospheres*, 118:5679–5697, 2013. doi: 10.1002/jgrd.50440.

- C. Emde and B. Mayer. Simulation of Solar Radiation During a Total Solar Eclipse: A Challenge for Radiative Transfer. *Atmos. Chem. Phys.*, 7:2259–2270, 2007. doi: 10.5194/acp-7-2259-2007.
- C. Emde, R. Buras, and B. Mayer. ALIS: An Efficient Method to Compute High Spectral Resolution Polarized Solar Radiances Using the Monte Carlo Approach. *J. Quant. Spectrosc. Radiat. Transfer*, 112:1622–1631, 2011. doi: 0.1016/j.jqsrt.2011.03.018.
- EUM MET REP 07 0132. *Cloud Detection for MSG - Algorithm Theoretical Basis Document*. EUMETSAT, Darmstadt, Germany, v2 edition, Nov 2007. EUM/MET/REP/07/0132.
- EUM OPS DOC 09 5164. *Cloud Mask Factsheet*. EUMETSAT, Darmstadt, Germany, v1 edition, Oct 2010. EUM/OPS/DOC/09/5164.
- EUM OPS DOC 09 5165. *SEVIRI - Clear Sky Reflectance Map Factsheet*. EUMETSAT, Darmstadt, Germany, v2b edition, Jul 2011. EUM/OPS/DOC/09/5165.
- EUM MET TEN 12 0332. *Conversion from Radiances to Reflectances for SEVIRI Warm Channels*. EUMETSAT, Darmstadt, Germany, v4 edition, Oct 2012. EUM/MET/TEN/12/0332.
- F. Ewald, L. Bugliaro, H. Mannstein, and B. Mayer. An Improved Cirrus Detection Algorithm MeCiDA2 for SEVIRI and its Validation with MODIS. *Atmos. Meas. Tech.*, 6:309–322, 2013. doi: 10.5194/amt-6-309-2013.
- Clemens Fricke, Andre Ehrlich, Manfred Wendisch, and Birger Bohn. *Wiss. Mitteil. Inst. f. Meteorol. Univ. Leipzig*, volume 50, chapter Influence of Surface Albedo Inhomogeneities on Remote Sensing of Optical Thin Cirrus Cloud Mikrophysics, pages 1–10. Inst. f. Meteorol. Univ. Leipzig, 2012.
- Josef Konrad Gasteiger. *Retrieval of Microphysical Properties of Desert Dust and Volcanic Ash Aerosols from Ground-based Remote Sensing*. PhD thesis, Ludwig–Maximilians–Universität München, 2011.
- H. Grassl. Calculated Circumsolar Radiation as a Function of Aerosol Type, Field of View, Wavelength, and Optical Depth. *Applied Optics*, 10:2542–2543, 1971.
- Donald Grether, David Evans, Arlon Hunt, and Michael Wahlig. Measurement and Analysis of Circumsolar Radiation. In *U.S. Department of Energy Insulation Resource Assessment Program Review*, Davis, CA, August 19-21, 1980.
- W. Greuell and R.A. Roebeling. Towards a Standard Procedure for Validation of Satellite-Derived Cloud Liquid Water Path. *Journal of Applied Meteorology and Climatology*, 48: 1575–1590, 2009. doi: 10.1175/2009JAMC2112.1.

- G. M. Hale and M. R. Querry. Optical Constants of Water in the 200-nm to 200- μ m Wavelength Region. *Appl. Opt.*, 12:555–563, 1973. doi: 10.1364/AO.12.000555.
- S.-H. Ham and B. J. Sohn. Assessment of the Calibration Performance of Satellite Visible Channels Using Cloud Targets: Application to Meteosat-8/9 and MTSAT-1R. *Atmos. Chem. Phys.*, 10:11131–11149, 2010. doi: 10.5194/acp-10-11131-2010.
- J.E. Hansen and L.D. Travis. Light Scattering in Planetary Atmospheres. *Space Sci. Rev.*, 16:527–610, 1974. doi: 10.1007/BF00168069.
- M. Hess, P. Köpke, and I. Schult. Optical Properties of Aerosols and Clouds: The Software Package OPAC. *Bulletin of the American Meteorological Society*, 79:831–844, 1998.
- E.J. Highwood. Suggested Refractive Indices and Aerosol Size Parameters for Use in Radiative Effect Calculations and Satellite Retrievals ADIENT / APPRAISE CP2 Technical Report, DRAFT V2. Technical report, Department of Meteorology, University of Reading, August 2009.
- B. N. Holben, T. F. Eck, I. Slutsker, D. Tanre, J. P. Buis, A. Setzer, E. Vermote, J. A. Reagan, Y. J. Kaufman, T. Nakajima, F. Lavenu, I. Jankowiak, and A. Smirnov. AERONET – A Federated Instrument Network and Data Archive for Aerosol Characterization. *Remote Sens. Environ.*, 66:1–16, 1998.
- T. Holzer-Popp, M. Schroedter-Homscheidt, H. Breitkreuz, D. Martynenko, and L. Klüser. Improvements of Synergetic Aerosol Retrieval for ENVISAT. *Atmospheric Chemistry and Physics*, 8(24):7651–7672, 2008. doi: 10.5194/acp-8-7651-2008.
- J. H. Joseph, W. J. Wiscombe, and J. A. Weinman. The Delta-Eddington Approximation for Radiative Flux Transfer. *J. Atmos. Sci.*, 33(12):2452–2459, December 1976. ISSN 0022-4928. doi: 10.1175/1520-0469(1976)033<2452:TDEAFR>2.0.CO;2.
- Ragini Kalapatapu, Matteo Chiesa, Peter Armstrong, and Stefan Wilbert. Measurement of DNI Angular Distribution with a Sunshape Profiling Irradiometer. In *SolarPACES*, Marrakesh, 09 2012.
- K. Kandler, L. Schütz, C. Deutscher, M. Ebert, H. Hofmann, S. Jäckel, R. Jaenicke, P. Knippertz, K. Lieke, A. Massling, A. Petzold, A. Schladitz, B. Weinzierl, A. Wiedensohler, S. Zorn, and S. Weinbruch. Size Distribution, Mass Concentration, Chemical and Mineralogical Composition and Derived Optical Parameters of the Boundary Layer Aerosol at Tinfou, Morocco, During SAMUM 2006. *Tellus B*, 61(1), 2011. doi: 10.1111/j.1600-0889.2008.00385.x.
- S. Kato, T. P. Ackerman, J. H. Mather, and E. Clothiaux. The k-Distribution Method and Correlated-k Approximation for a Shortwave Radiative Transfer Model. *J. Quant. Spectrosc. Radiat. Transfer*, 62:109–121, 1999.

- David L. King. Photovoltaic Module and Array Performance Characterization Methods for All System Operating Conditions. *AIP Conf. Proc.*, 394:347–368, 1996. doi: 10.1063/1.52852.
- S. Kinne, T.P. Akermann, M. Shiobara, A. Uchiyama, A.J. Heymsfield, L. Miloshevich, J. Wendell, E.W. Eloranta, C. Purgold, and R.W. Bergstrom. Cirrus Cloud Radiative and Microphysical Properties from Ground Observations and In Situ Measurements During Fire 1991 and their Application to Exhibit Problems in Cirrus Solar Radiative Transfer Modeling. *Journal of the Atmospheric Sciences*, 54:2320–2344, 1997.
- S. Kox, A. Ostler, M. Vazquez-Navarro, L. Bugliaro, and H. Mannstein. Optical Properties of Thin Cirrus Derived from the Infrared Channels of SEVIRI. In *EUMETSAT Meteorological Satellite Conference, Oslo, Norway*, Darmstadt, 2011. EUMETSAT.
- Stephan Kox. *Remote Sensing of the Diurnal Cycle of Optically Thin Cirrus Clouds*. PhD thesis, Ludwig–Maximilians–Universität München, 2012. URL <http://nbn-resolving.de/urn:nbn:de:bvb:19-151170>.
- W. Krebs, H. Mannstein, L. Bugliaro, and B. Mayer. Technical Note: A New Day- and Night-Time Meteosat Second Generation Cirrus Detection Algorithm MeCiDA. *Atmos. Chem. Phys.*, 7:6145–6159, 2007.
- Peter Köpke, Joachim Reuder, and Jan Schween. Spectral Variation of the Solar Radiation During an Eclipse. *Meteorologische Zeitschrift*, 10:179–186, 2001. doi: 10.1127/0941-2948/2001/0010-0179.
- Kuo-Nan Liou. *An Introduction to Atmospheric Radiation*. International Geophysics Series. 26. Academic Press, New York, 1980. ISBN 0-12-451450-2.
- N.G. Loeb and R. Davies. Angular Dependence of Observed Reflectances: A Comparison with Plane Parallel Theory. *Journal of Geophysical Research*, 102(D6):6865–6881, 1997.
- N.G. Loeb, T. Varnai, and R. Davies. Effect of Cloud Inhomogeneities on the Solar Zenith Angle Dependence of Nadir Reflectance. *Journal of Geophysical Research*, 102(D8): 9387–9395, 1997.
- S. Lohmann, C. Schillings, B. Mayer, and R. Meyer. Long-Term Variability of Solar Direct and Global Radiation Derived from ISCCP Data and Comparison with Reanalysis Data. *Solar Energy*, 80(11):1390–1401, November 2006. ISSN 0038-092X.
- Kaj Madsen, Hans Bruun Nielsen, and Ole Tingleff. *Methods for Non-Linear Least Squares Problems*. Informatics and Mathematical Modelling, Technical University of Denmark, DTU, Richard Petersens Plads, Building 321, DK-2800 Kgs. Lyngby, 2004. URL http://www2.imm.dtu.dk/pubdb/views/edoc_download.php/3215/pdf/imm3215.pdf. Last accessed 25 Jul. 2013.

- A. Mangold, H. De Backer, B. De Paepe, S. Dewitte, I. Chiapello, Y. Derimian, M. Kacenenbogen, J.-F. Léon, N. Huneus, M. Schulz, D. Ceburnis, C. O'Dowd, H. Flentje, S. Kinne, A. Benedetti, J.-J. Morcrette, and O. Boucher. Aerosol Analysis and Forecast in the European Centre for Medium-Range Weather Forecasts Integrated Forecast System: 3. Evaluation by Means of Case Studies. *Journal of Geophysical Research*, 116 (D3):D03302, February 2011. ISSN 0148-0227. doi: 10.1029/2010JD014864.
- B. Mayer and A. Kylling. Technical Note: The libRadtran Software Package for Radiative Transfer Calculations: Description and Examples of Use. *Atmos. Chem. Phys.*, 5:1855–1877, 2005. doi: 10.5194/acp-5-1855-2005.
- Bernhard Mayer. Radiative Transfer in the Cloudy Atmosphere. *Eur. Phys. J. Conferences*, 1:75–99, 2009. doi: 10.1140/epjconf/e2009-00912-1.
- G.M. McFarquhar and A.J. Heymsfield. The Definition and Significance of an Effective Radius for Ice Clouds. *Journal of the Atmospheric Sciences*, 55:2039–2052, 1998.
- J. F. Meirink, R. A. Roebeling, and P. Stammes. Inter-Calibration of Polar Imager Solar Channels Using SEVIRI. *Atmos. Meas. Tech. Discuss.*, 6(2):3215–3247, 2013. doi: 10.5194/amtd-6-3215-2013.
- Richard Meyer. International Solar Energy Society Webinar: DNI Information for CSP Development Part3: Improving Knowledge during Project Development, 2013. URL http://www.ises-online.de/fileadmin/user_upload/PDF/ISES-Webinar-DNI-P3_rMeyer-Suntrace_20130529.pdf. 29 May 2013, last accessed 14 Aug 2013.
- Richard Meyer, Jesús Torres Butron, Gunnar Marquardt, Marko Schwandt, Norbert Geuder, Carsten Hoyer-Klick, Elke Lorenz, Annette Hammer, and Hans Georg Beyer. Combining Solar Irradiance Measurements and Various Satellite-Derived Products to a Site-Specific Best Estimate. In *SolarPACES Symposium 2008*, 2008.
- G. Mie. Beiträge zur Optik trüber Medien, speziell kolloidaler Metallösungen. *Annalen der Physik, Vierte Folge*, 25(3):377–445, 1908.
- Qilong Min and Minzheng Duan. Simultaneously Retrieving Cloud Optical Depth and Effective Radius for Optically Thin Clouds. *Journal of Geophysical Research: Atmospheres*, 110(D21):n/a–n/a, 2005. doi: 10.1029/2005JD006136.
- J.-J. Morcrette, O. Boucher, L. Jones, D. Salmond, A. Beljaars P. Bechtold, A. Benedetti, A. Bonet, J. W. Kaiser, M. Razinger, M. Schulz, S. Serrar, A. J. Simmons, M. Sofiev, M. Suttie, A. M. Tompkins, and A. Untch. Aerosol Analysis and Forecast in the European Centre for Medium-Range Weather Forecasts Integrated Forecast System: Forward Modeling. *Journal of Geophysical Research*, 114:D06206, 2009.

- Teruyuki Nakajima and Michael D. King. Determination of the Optical Thickness and Effective Particle Radius of Clouds from Reflected Solar Radiation Measurements. Part I: Theory. *Journal of the Atmospheric Sciences*, 47:1878–1893, 1990.
- Teruyuki Nakajima, Masayuki Tanaka, and Toyotato Yamauchi. Retrieval of the Optical Properties of Aerosols from Aureole and Extinction Data. *Appl. Opt.*, 22(19):2951–2959, 1983. doi: 10.1364/AO.22.002951.
- A. Neumann and A. Witzke. The Influence of Sunshape on the DLR Solar Furnace Beam. *Solar Energy*, 66(6):447 – 457, 1999. ISSN 0038-092X. doi: 10.1016/S0038-092X(99)00048-1.
- A. Neumann, B. von der Au, and P. Heller. Measurements of Circumsolar Radiation at the Plataforma Solar (Spain) and in Cologne (Germany). In *Proc. of Int. Solar Energy Conf. Solar Engineering*. ASME, 1998.
- Andreas Neumann, Andreas Witzke, Scott A. Jones, and Gregor Schmitt. Representative Terrestrial Solar Brightness Profiles. *Journal of Solar Energy Engineering Transactions of the ASME*, 124:198–204, 2002. doi: 10.1115/1.1464880.
- J.E. Noring, D.F. Grether, and A.J. Hunt. Circumsolar Radiation Data: The Lawrence Berkely Laboratory Reduced Data Base. Technical Report NREL/TP-262-44292, National Renewable Energy Laboratory, 1991. URL <http://rredc.nrel.gov/solar/pubs/circumsolar/index.html>. Last accessed 26 Jul. 2013.
- Andreas Ostler. Validierung von optischen Wolkeneigenschaften aus MSG-Daten. Masterarbeit, Ludwig-Maximilians-Universität München, 2011.
- Grant William Petty. *A First Course in Atmospheric Radiation*. Sundog Publishing, Madison, 2. edition, 2006. ISBN 0-9729033-1-3.
- D. Pozo-Vázquez, S. Wilbert, C.A. Gueymard, L. Alados-Arboledas, F.J. Santos-Alamillos, and M.J. Granados-Muñoz. Interannual Variability of Long Time Series of DNI and GHI at PSA, Spain. In *SolarPaces 2011*, 2011.
- A. Rabl and P. Bendt. Effect of Circumsolar Radiation on Performance of Focusing Collectors. *J. Sol. Energy Eng.*, 104:237, 1982.
- Lord Rayleigh (J. W. Strutt). *Phil. Mag.*, 41:107, 274 and 447, 1871.
- Bernhard Reinhardt, Robert Buras, Luca Bugliaro, and Bernhard Mayer. Determination of the Sunshape from Meteosat Second Generation. Technical report, 2012. SFERA Project Report, Deliverable R13.4.
- Bernhard Reinhardt, Robert Buras, Luca Bugliaro, Stefan Wilbert, and Bernhard Mayer. Determination of Circumsolar Radiation from Meteosat Second Generation. *Atmos. Meas. Tech. Discuss.*, 6:5835–5879, 2013. doi: 10.5194/amtd-6-5835-2013.

- P. Ricchiazzi, S. Yang, C. Gautier, and D. Sowle. SBDART: A Research and Teaching Software Tool for Plane-Parallel Radiative Transfer in the Earth's Atmosphere. *Bulletin of the American Meteorological Society*, 79:2101–2114, 1998.
- J. M. Ritter and K. J. Voss. A New Instrument for Measurement of the Solar Aureole Radiance Distribution from Unstable Platforms. *Journal of Atmospheric and Oceanic Technology*, 17:1040–1047, 2000.
- Helmut Scheffler and Hans Elsässer. *Physik der Sterne und der Sonne, 2. Auflage*. BI-Wiss.-Verl., Mannheim, 1990.
- J. Schmetz, P. Pili, S. Tjemkes, D. Just, J. Kerkmann, S. Rota, and A. Ratier. An Introduction to Meteosat Second Generation (MSG). *Bulletin of the American Meteorological Society*, 83:977–992, 2002.
- M. Schubnell. Influence of Circumsolar Radiation on Aperture, Operating Temperature and Efficiency of a Solar Cavity Receiver. *Solar Energy Materials and Solar Cells*, 27(3):233 – 242, 1992. ISSN 0927-0248. doi: 10.1016/0927-0248(92)90085-4.
- Gregory L. Schuster, Oleg Dubovik, and Brent N. Holben. Angstrom Exponent and Bimodal Aerosol Size Distributions. *Journal of Geophysical Research: Atmospheres*, 111(D7), 2006. ISSN 2156-2202. doi: 10.1029/2005JD006328.
- Michal Segal-Rosenheimer, Phillip B. Russell, John M. Livingston, S. Ramachandran, Jens Redemann, and Bryan A. Baum. Retrieval of Cirrus Properties by Sunphotometry: A New Perspective on an Old Issue. *Journal of Geophysical Research: Atmospheres*, 118: 1–18, 2013. ISSN 2169-8996. doi: 10.1002/jgrd.50185.
- E.P. Shettle and R.W. Fenn. Models for the Aerosols of the Lower Atmosphere and the Effects of Humidity Variations on their Optical Properties. Technical Report AFGL-TR-79-0214, Air Force Geophysics Laboratory, Hanscom AFB, Massachusetts, 1979.
- M. Shiobara and S. Asano. Estimation of Cirrus Optical Thickness from Sun Photometer Measurements. *Journal of Applied Meteorology*, 33(6):672–681, 1994. doi: 10.1175/1520-0450(1994)033<0672:EOCOTF>2.0.CO;2.
- K. Stamnes, S.C. Tsay, W. Wiscombe, and K. Jayaweera. A Numerically Stable Algorithm for Discrete-Ordinate-Method Radiative Transfer in Multiple Scattering and Emitting Layered Media. *Applied Optics*, 27(12):2502–2509, 1988.
- K. Stamnes, S.-C. Tsay, W. Wiscombe, and I. Laszlo. DISORT, a General-Purpose Fortran Program for Discrete-Ordinate-Method Radiative Transfer in Scattering and Emitting Layered Media: Documentation of Methodology. Technical report, Dept. of Physics and Engineering Physics, Stevens Institute of Technology, Hoboken, NJ 07030, 2000.

- Olaf Stein, Martin Schultz, Johannes Flemming, Antje Inness, Johannes Kaiser, Luke Jones, Angela Benedetti, and Jean-Jacques Morcrette. MACC Global Air Quality Services – Technical Documentation. Technical report, Forschungszentrum Jülich / ECMWF, Jülich / Reading, November 2011.
- A.H. Strahler, J.P. Muller, and MODIS Science Team Members. MODIS BRDF/Albedo product: Algorithm Theoretical Basis Document Version 5.0, 1999. URL http://modis.gsfc.nasa.gov/data/atbd/atbd_mod09.pdf. Last accessed 22 Mar. 2011.
- Edith Thomalla, Peter Köpke, Heinz Mueller, and Heinrich Quenzel. Circumsolar Radiation Calculated for Various Atmospheric Conditions. *Solar Energy*, 30:575–587, 1983. doi: 10.1016/0038-092X(83)90069-5.
- M. Waldmeier. *Ergebnisse und Probleme der Sonnenforschung - Probleme der kosmischen Physik*, volume 22. Akademische Verlagsgesellschaft Becker und Erler, Leipzig, 1941.
- Kathrin Wapler. *Der Einfluss des dreidimensionalen Strahlungstransportes auf Wolkenbildung und -entwicklung*. PhD thesis, Ludwig-Maximilians-Universität München, 2007. URL <http://nbn-resolving.de/urn:nbn:de:bvb:19-68948>.
- A. D. Watt. Circumsolar Radiation. Technical report, Sandia National Laboratories, Albuquerque, New Mexico, 1980.
- Viktor Wesselak and Thomas Schabbach. *Regenerative Energietechnik*. Springer-Verlag, Berlin, Heidelberg, 2009. doi: 10.1007/978-3-540-95882-6.
- M. Wiegner, J. Gasteiger, K. Kandler, B. Weinzierl, K. Rasp, M. Esselborn, V. Freudenthaler, B. Heese, C. Toledano, M. Tesche, and D. Althausen. Numerical Simulations of Optical Properties of Saharan Dust Aerosols with Emphasis on Lidar Applications. *Tellus B*, 61(1), 2011. doi: 10.1111/j.1600-0889.2008.00381.x.
- S. Wilbert, B. Reinhardt, J. DeVore, M. Röger, R. Pitz-Paal, and C. Gueymard. Measurement of Solar Radiance Profiles with the Sun and Aureole Measurement System (SAM). In *SolarPaces 2011*, 2011.
- S. Wilbert, B. Reinhardt, J. DeVore, M. Röger, R. Pitz-Paal, C. Gueymard, and R. Buras. Measurement of Solar Radiance Profiles With the Sun and Aureole Measurement System (SAM). *Journal of Solar Energy Engineering*, 135:041002, 2013. doi: 10.1115/1.4024244.
- Stefan Wilbert, Robert Pitz-Paal, and Joachim Jaus. Circumsolar Radiation and Beam Irradiance Measurements for Focusing Collectors. In *ES1002: Cost Wire Workshop*, Risö, 2012. URL <http://elib.dlr.de/78602/>.
- D.S. Wilks. *Statistical Methods in the Atmospheric Sciences*. Academic Press Inc., Amsterdam, 2 edition, 2005.

- P. Yang, K.N. Liou, K. Wyser, and D. Mitchell. Parameterization of the Scattering and Absorption Properties of Individual Ice Crystals. *Journal of Geophysical Research*, 105 (D4):4699–4718, 2000.
- P. Yang, H. Wei, H.-L. Huang, B.A. Baum, Y.X. Hu, G.W. Kattawar, M.I. Mishchenko, and Q. Fu. Scattering and Absorption Property Database for Nonspherical Ice Particles in the Near- Through Far-Infrared Spectral Region. *Applied Optics*, 44(26):5512–5523, 2005.
- Wilford Zdunkowski, Thomas Trautmann, and Andreas Bott. *Radiation in the Atmosphere: A Course in Theoretical Meteorology*. Cambridge University Press, Cambridge, 2007. ISBN 978-0-521-87107-5.

Glossary

| | |
|----------|---|
| AOT | Aerosol optical thickness |
| APICS | Algorithm for the Physical Investigation of Clouds |
| BC | Black carbon |
| COCS | Cloud Optical properties derived from CALIOP and SEVIRI algorithm |
| CSR | Circum solar ratio |
| CST | Concentrating solar technology |
| DNI | Direct normal irradiance |
| ECMWF | European Centre for Medium-Range Weather Forecasts |
| EUMETSAT | European Organisation for the Exploitation of Meteorological Satellites |
| FAR | False alarm rate |
| GHI | Global horizontal irradiance |
| ICC | Ice cloud cover |
| IFS | Integrated forecast system |
| INSO | Insoluble |
| LANDSAF | Land surface analysis satellite applications facility |
| LE | Local estimate |
| LIDAR | Light detection and ranging |

| | |
|------------------|--|
| LUT | Lookup Table |
| MeCiDa | Meteosat Second Generation Cirrus Detection Algorithm |
| MIAM | Mineral accumulation mode |
| MICM | Mineral coarse mode |
| MINM | Mineral nucleation mode |
| MODIS | Moderate-Resolution Imaging Spectroradiometer (aboard NASA's polar orbiting satellites Terra and Aqua) |
| MSG | Meteosat Second Generation meteorological satellite series |
| MYSTIC | Monte Carlo Code for the Physically Correct Tracing of Photons in Cloudy Atmospheres |
| NRT | Near real time |
| OC | Organic carbon |
| OPAC | Optical Properties of Aerosols and Clouds |
| PSA | Plataforma Solar de Almería |
| RH | Relative humidity |
| RT | Radiative transfer |
| RTE | Radiative transfer equation |
| SAM | Sun and Aureole Measurement System |
| SAMS | SAM based system |
| SEVIRI | Spinning Enhanced Visible Infra-Red Imager (aboard the MSG satellites) |
| SSAM | Sea salt accumulation mode |
| SSCM | Sea salt coarse mode |
| TOA | Top of atmosphere |
| WASO | Water-soluble |

Acknowledgements

First of all I would like to thank my advisors Robert Buras and Bernhard Mayer. They were always supportive when I had problems or concerns and shared their ideas with me – many who have found their way into this document. They also provided linguistic support in stylisation of the manuscript. Luca Bugliaro did the predominant programming work concerning the improvement of APICS. He also developed the software code to correct for the parallax in the SEVIRI measurements which I used in the validation section. Many ideas concerning the improvement of APICS came from his side. I would like to thank him for many fruitful discussions. Josef Gasteiger and Claudia Emde provided useful insights concerning optical properties of aerosols and clouds. Josef’s database of pre-calculated aerosol optical properties enabled the generation of bulk aerosol optical properties for libRadtran resembling the physical properties of the aerosol as in the ECMWF IFS. I would like to thank Peter Köpke for his advice on OPAC and aerosols in general. Special thanks also go to Stephan Kox who provided me the COCS data and performed several processing runs specifically for me. Stefan Wilbert provided ground measurements of the circumsolar radiation as well as other meteorological measurands at the Plataforma Solar de Almería. I would also like to thank him for our always inspiring exchange of ideas as well as for the hospitality that I received during my 2-months stay with DLR-Almería. Many thanks also to my other colleagues at DLR and MIM for the good times and the supportive atmosphere – especially to my office mate Fabian. Last but not least I would like to thank my family, especially my parents Martina and Wolfgang and my girl friend Christina, for always backing me up.

This study was mainly founded by the EU’s FP7 through the project “Solar Facilities for the European Research Area – SFERA”.